ALMA MATER STUDIORUM · UNIVERSITÀ DI BOLOGNA

Scuola di Scienze
Corso di Laurea Magistrale in Fisica

Morphological characterization of ZnS thin films for photovoltaic applications

Relatore:
Prof.ssa Daniela Cavalcoli

Correlatore:
Dott.ssa Martina Perani

Presentata da:
Alberto Bartolucci

Anno accademico 2014/2015
Sessione III

Contents

Abstract **1**

Introduction **3**

1 Introduction to photovoltaics **7**
1.1 Renewable sources: a global energy solution . . . 7
1.2 Present status and perspectives of photovoltaics . . . 13
1.3 The physics of a solar cell . . . 14
1.3.1 The solar spectrum . . . 14
1.3.2 *I-V* characteristic and main definitions of a solar cell . . . 16
1.3.3 Homojunction and heterojunctions . . . 20
1.3.4 The Shockley-Queisser limit . . . 21
1.3.5 Surface passivation . . . 24
1.4 Solar cells generations . . . 27

2 Zinc Sulfide State of the Art **31**
2.1 Main characteristics . . . 31
2.1.1 Crystal structure . . . 32
2.1.2 Optical properties . . . 32
2.1.3 Dielectric properties . . . 34
2.2 Applications in photovoltaics . . . 35

3 Materials and Methods **37**
3.1 Materials . . . 37
3.2 Methods . . . 40
3.2.1 Atomic Force Microscopy . . . 40
3.2.2 Experimental setup . . . 41
3.2.3 AFM modes of operation . . . 46
3.2.4 Image processing . . . 52
3.2.5 Image analysis . . . 56
3.2.6 Dips analysis . . . 61
3.2.7 Sheet resistance measurement . . . 64

3.2.8 EFM – KPFM characterization 66

4 Experimental Results 69

4.1 Morphological characterization 69
4.1.1 ZnS morphology 70
4.1.2 ZnO morphology 74
4.2 Presence and density of dips 75
4.2.1 Choice of z_{segm} 75
4.2.2 Dip analysis results 80
4.3 Structural and grain properties 82
4.3.1 50 W – ZnS_35 83
4.3.2 75 W – ZnS_36 86
4.3.3 125 W – ZnS_60 89
4.3.4 150 W – ZnS_53 92
4.3.5 Choice of segmentation parameters 95
4.3.6 Sputtering power dependence of the results 97
4.4 Comparison with ZnO 99
4.4.1 ZnO – Structural and grain analyses results 99
4.4.2 Results comparison and discussion 102
4.5 Electrostatic characterization results 103
4.5.1 EFM surface topography 103
4.5.2 Sheet resistance result 105
4.5.3 ZnS – Al contact potential difference 105
4.6 Discussion 107

Conclusions 109

Acknowledgements 113

Bibliography 115

Abstract

Le celle solari a film sottile rappresentano una delle alternative più promettenti per un abbattimento dei costi che incentivi significativamente la produzione di impianti fotovoltaici nel prossimo futuro. In questo contesto, la ricerca di nuovi materiali non tossici e più economici per la passivazione delle superfici, necessaria per aumentare l'efficienza delle celle, è di fondamentale importanza.

L'obiettivo di questa tesi è effettuare uno studio approfondito sulle caratteristiche morfologiche ed elettrostatiche di film sottili di ZnS, le cui interessanti proprietà trovano applicazione in svariati ambiti tecnologici, tra i quali dispositivi fotovoltaici ed optoelettronici. Si tratta di un materiale innovativo, le cui proprietà fisiche, nonostante le varie recenti applicazioni, sono state ancora poco studiate.

I film sottili di ZnS analizzati sono stati cresciuti tramite polverizzazione catodica a tensione continua (DC sputtering) a diversa potenza per studiare le connessioni tra condizioni di deposizione e caratteristiche strutturali, le quali determinano le proprietà di questi materiali nel contesto di applicazioni tecnologiche.

Lo studio delle proprietà morfologiche alla nanoscala è stato condotto mediante acquisizione di mappe con microscopia a forza atomica (AFM). Uno dei fattori associati alla qualità dei film è il profilo superficiale, per questa ragione è stata dapprima effettuata un'analisi dei buchi (dips) in funzione della potenza di sputtering, al fine di individuare il campione con la minore densità di dips in vista di applicazioni fotovoltaiche.

I parametri associati alla struttura superficiale, quali la rugosità superficiale, la lunghezza di correlazione laterale e l'esponente di Hurst, sono stati determinati tramite un'analisi statistica delle immagini. I parametri associati ai grani presenti sulla superficie, quali numero e dimensione, sono stati ricavati attraverso un processo di segmentazione delle immagini. Le stesse misure sono state svolte su due campioni di ZnO per comparare i risultati dei due composti.

L'analisi elettrostatica è stata condotta sul campione che ha mostrato la minor rugosità e densità di dips tra quelli analizzati, ed è stata effettuata tramite acquisizione di mappe di potenziale di contatto alla nanoscala con tecnica Electrostatic Force Microscopy (EFM). Un'ulteriore misura con tecnica Kelvin Probe Force Microscopy (KPFM) ha permesso di valutare la differenza di potenziale tra layers di Al depositati sulla superficie del campione e ZnS, corrispondente alla differenza tra la funzione

lavoro di Al e l'affinità elettronica di ZnS. Infine è stata misurata la resistenza elettrica di ZnS con metodo a quattro punte.

Dai risultati morfologici si è ottenuto che la potenza di sputtering influenza significativamente la struttura superficiale, ma senza una proporzionalità lineare. I campioni mostrano una rugosità che varia in modo non lineare tra 0.79 e 3.44 nm e una lunghezza di correlazione in un range da 10.8 a 34 nm. La densità dei grani è risultata variare tra 1100 e 1600 μm^{-2}, con un raggio medio equivalente dei singoli grani che varia tra 12 e 16 nm. I valori ottenuti per i campioni di ZnO mostrano una rugosità molto più elevata e una minor densità di grani.

Per la maggior parte dei campioni analizzati, la lunghezza di correlazione è risultata maggiore rispetto al raggio medio dei grani, da cui si è evinto un processo di clustering degli stessi. Tuttavia si è osservato che ciò non vale per il campione depositato a una potenza di 75 W, il quale inoltre esibisce la minor rugosità e la minor densità di dips. Da ciò si è concluso che potenze di sputtering troppo grandi o troppo piccole in fase di deposizione promuovono il fenomeno di clustering dei grani, di conseguenza aumentandone le dimensioni e incrementando la rugosità superficiale del film. La presenza di grani più grandi risulta correlata ad un maggior numero di dips. Al contrario, superfici composte da grani più piccoli e numerosi risultano avere una minore densità di dips, presentando dunque un profilo superficiale più regolare e con minor rugosità.

Dall'analisi elettrostatica è emersa una corrispondenza diretta tra la morfologia superficiale e il potenziale di contatto, da cui si è dedotto che la densità di carica locale tende ad accumularsi maggiormente in regioni concave. La differenza di potenziale di contatto misurata tra i layers di Al e ZnS è risultata un ordine di grandezza inferiore rispetto ai valori noti da letteratura. Ciò potrebbe essere dovuto alla presenza di stati superficiali indotti dalla formazione di ossidi, sperimentalmente già osservati da studi recenti, che portano a sottostimare la differenza di potenziale reale. Infine, si è ottenuta un limite inferiore per la resistenza elettrica di ZnS di 7 GΩ, andando a confermare le proprietà dielettriche del materiale.

Introduction

'The growing threat of climate change define the contours of this century more dramatically than any other'. This words, said by the US president Barack Obama at the United Nations Framework Conference on Climate Change (UNFCCC) in Paris, in November 2015, define well what many people believe to be among the biggest challenges for human kind in the 21st century. The first challenge is that nowadays the energy consumption strongly depends on fossil fuels like oil, coal and gas. Fossil fuels are not a sustainable energy resource, in the sense that they are not refilled by the nature. More important, by burning fossil fuels the production of greenhouse gases like carbon dioxide (CO_2) is promoted [1]. According to a major part of the scientific community, the additional CO_2 created by human activities is stored in oceans and atmosphere, leading to heavy climate changes that if not stopped could cause catastrophic scenarios in the next future. A second challenge is to supply the global energy demand that is rapidly growing with the increase of the world population, which some studies predict to reach 9 billion around 2040 in contrast to the 7 billion people living on the planet today. Especially, the living standard is rapidly increasing in developing countries like China and India, where more than a third of the world's population is living, according to the data from US Energy Information Administration (EIA) [2].

Finding other sources of energy is of primary importance for both an environmental-friendly consumption and to fill the gap due to the extra energy demand. From this point of view, the development of renewable resources is considered the best alternative to fossil fuels to supply energy in the next future. While all renewable resources will be important, only photovoltaics can provide this level of demand while releasing a low quantity of pollutants. In addition, photovoltaics has been one of the more active field of research in the last decades, with wide opportunities to improve the solar cells performances in order to obtain more energy while lowering material costs [3].

Different semiconductor materials with suitable optoelectronic properties have been found for photovoltaic applications. Silicon is the most commonly used active material for solar cells applications, with over the 85 % of the whole photovoltaic market dominated by crystalline silicon wafer technology. monocrystalline and polycrystalline silicon based solar cells have efficiencies approaching 20 - 25 %. However, despite new technologies that reduce the use of silicon exist, alternative materials and solutions are studied. This has led the photovoltaic industry to produce thin film solar cells consisting of cheaper materials and smaller thickness. The efficiencies reached by the

thin film solar cells result lower than silicon wafer cells, being of about 10 – 15 %. However, the ratio of efficiency to price makes these cells competitive in the photovoltaic market, with wider possibilities to improve the efficiency [3]. Thin film solar cells are made by deposition of more thin layers on a rigid substrate, with the presence of passivating material layers in the front and rear surfaces to reduce the surface recombination of minority carriers, which is among the major causes of efficiency loss [4].

Many studies have already proved the crucial importance of the surface passivation, especially for thin film solar cells. Actually, the presence of passivating layers in thin film solar cells technology is essential for a significant efficiency increase, making the implement of an effective passivation method a near-term challenge in the PV industry. Among various suitable materials for surface passivation, Al_2O_3 has been observed to increase significantly the efficiency of several types of cells. Recent investigations have led attention on zinc sulfide (ZnS) as a suitable material to be used as passivating layer for thin film solar cells [5,6]. The interesting properties of ZnS could be useful in various devices, covering a wide area of applications, among which can be included: antireflection coating for the solar cells, non-toxic buffer layer (compared to CdS layer in CIGS based thin film solar cells), wide energy gap material for electroluminescent and optoelectronic devices, photosynthetic coating and blue emitting laser diodes [7].

In this thesis, a morphological characterization of a series of ZnS thin layers at the nano-scale has been performed with Atomic Force Microscopy (AFM) technique to evaluate the main structural features. ZnS thin films deposited on a substrate by DC sputtering at different deposition conditions have been studied in the analysis, in order to measure how those conditions affects the morphological properties of the layers. The surface morphology has been investigated in order to perform a thorough characterization of the surface structure. In the framework of photovoltaic applications, a particular attention has been paid to structural properties related to the surface flatness, i.e. the roughness and density of dips. In addition, the electrical resistance has been measured by using a four-point probes method. Moreover, to get a characterization of the electrostatic profile at the surface, contact potential maps have been obtained by using Electrostatic Force Microscopy (EFM) and Kelvin Probe Force Microscopy (KPFM) techniques.

The contents of the thesis are the following: an overview on the field of photovoltaics, including the current status and future perspectives of technology, the working principles and the main definitions of a solar cell are described in Chapter 1. A description of the material studied, ZnS, with its structural, optical, electric properties, and the actual status of art for technological applications is reported in Chapter 2. The samples description and their properties are illustrated in the first section of Chapter 3. The second section of Chapter 3 is focused on the experimental setup used for all the measurements, the main features of AFM technique, the image processing method and the statistical analysis used to calculate the parameters.

The experimental results of all the measurements on different samples, with a comparison to another Zn compound (ZnO), the morphological AFM images performed and the parameters used during the analysis are reported and discussed. Finally, conclusions about the experimental results have been made.

Chapter 1
Introduction to Photovoltaics

In this chapter, an overview on the field of photovoltaics (PV), with its main motivations and applications, has been reported. In Section 1.1, the renewable energies, among which PV represents the most active field of research, are described. The actual status and prospects of PV technology are discussed in Section 1.2. The physics principles behind the solar cells, including the sunlight spectrum, the main circuital characteristics and definitions, the maximum theoretical limit for the efficiency and the surface passivation method, are illustrated in Section 1.3. Finally, a description of the three generations of solar cells with their basic schemes and efficiencies is reported in Section 1.4.

1.1 Renewable sources: a global energy solution

The constant demographic and technological growth that occurred in the last decades has yielded to an enormous increase of the worldwide request of energy. The present global energy consumption per inhabitant has been calculated to be around 6000 kWh per year [8]. From the last century, the main sources of energy have been found in exploitation of oil and gas, namely the fossil fuels. With the development of the nuclear energy a new source was found, but the issues associated to radioactive waste have been matter of discussion for a long time, and they are still today. However, for the easiness and the reduced risks associated with their use, human society has relied particularly on fossil fuels during the last decades. It was in 1956 the first presentation of the Hubbert peak theory [9], by which the rate of oil production has been described to follow a curve that reaches a maximum and then declines. Considering that the peak has been proved to have been around the 1970 [9], and the amount of oil under the ground in any region is finite, according to the International Energy Agency (IEA) for most

countries the oil production has already started to decline [10]. Moreover, according to the BP's Energy Outlook [11], the global energy consumption is expected to increase by 34 % between 2014 and 2035.

The massive usage of electrical power generated by fossil fuels has induced climate changes, due to the emission of greenhouse gases into the Earth's atmosphere. These gases are transparent to incoming solar radiation on Earth, but they absorb and re-emit infrared radiation within the atmospherem causing the global temperature to increase. Greenhouse gases naturally present in the atmosphere consist in water vapor (H_2O), carbon dioxide (CO_2), methane (CH_4), nitrous oxide (N_2O) and ozone (O_3), which except from ozone have largely incremented in recent years according to the European Environment Agency (EEA) [12]. Figure 1.1 shows the main climate change due to the incessant use of fossil fuels. One of the main constituents of the human-emitted greenhouse gases is composed by carbon dioxide (CO_2). This is is an important heat-trapping gas released through human activities such as agriculture and land use changes like deforestation, use of industrial gases and burning of fossil fuels in electricity generation, transport, industry and households [13]. Figure 1.1 *(a)* shows the atmospheric CO_2 levels from 2005 to 2016.

Global warming has led to a rise in the average surface temperature by 0.6 to 0.9 °C globally and by about 1 °C in Europe between 1906 and 2005, and the rate of temperature increase has nearly doubled in the last 50 years [14]. Without a global action to limit the emissions, the Intergovernmental Panel on Climate Change (IPCC) expects that global temperature may increase further by 1.8 to 4.0 °C by 2100 [15]. Figure 1.1 *(b)* shows the global temperature anomaly registered between 1880 and 2015. The 10 warmest years in the 134-year record all have occurred since 2000 [13].

The increase in the average temperature has been widely proved to be the main cause of ice melting, with consequent increase of the sea level. Data from NASA's Grace satellites have shown that the ice sheets in both Antarctica and Greenland are losing mass. The continent of Antarctica has been losing about 134 billion metric tons of ice per year since 2002, while the Greenland loss have been estimated in about 287 billion metric tons per year [13]. The Antarctica ice mass variation since 2002 are depicted in Figure 1.1 *(c)*. The melting of ice, jointly with the thermal expansion of the oceans (the increase in volume due to rising ocean water temperature), have inevitably led to the sea level rise. This is an important indicator of climate change, which also increases the probability of storms and endangers coastal ecosystems by flooding flat coastal regions [15]. Coastal areas often contain important urban centers and infrastructures. Thus coastal flooding related to sea level rise could affect a large part of the population [15]. Figure 1.1 *(d)* shows the variation in the sea level from 1993 as observed by satellites.

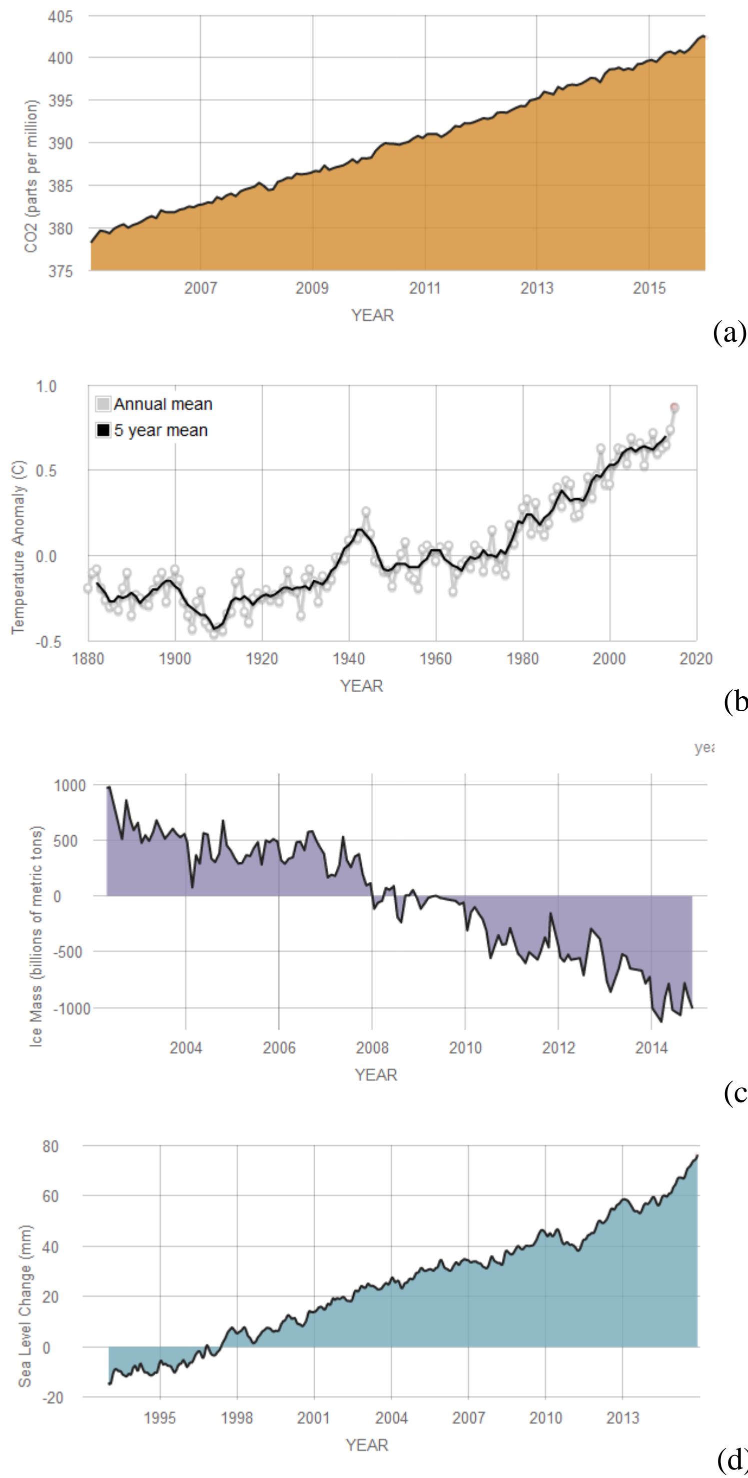

Figure 1.1: Main climate changes due to global warming: *(a)* Atmospheric CO_2 levels since 2005 *(montly measurements)*; *(b)* Global surface temperature change relative to 1951-1980 average temperatures (*NASA GISS); (c)* Antarctica ice mass variation since 2002 (*NASA's Grace satellites); (d)* Sea level change since 1993 (*data source: NASA GSFC)* [13].

The development of other sources of energy is necessary not only from an ecological point of view, but also by considering the gap between the fossil fuels production and the global energy demand that there will be in the next future. The best possible alternative to fossil fuels today is given by renewable energies, mainly hydroelectric, wind and solar energy, based on the continuing flows from sources of energy that can be approximated as inexhaustible. The world's largest oil company Shell expects that in the next future a restructuring of the energy industry will take place. In this scenario the global demand of fossil fuels will be still important, but it will reach a plateau by 2020 [16]. From this moment, renewable energy will become significant. Figure 1.2 shows the energy demand by regions *(a)* and the energy type of exploitation *(b)* between 2000 and 2050.

The main advantages of using renewable energy sources over the fossil fuels are a cleaner environment, new employment opportunities, and security of energy supply. Figure 1.3 shows the top countries with installed renewable energy infrastructures in recent years. Emissions of greenhouse gases and other pollutants can be reduced by the use of renewable energy. A collective use of renewable sources of energy would also lead to job creation in the technology manufacturing industries and also in the agricultural sector, which can supply biomass fuel. According to IEA, in 2012 the world relied on renewable sources for around 13.2 % of its total primary energy supply [17]. In 2013 renewables accounted for almost 22 % of global electricity generation, and the IEA Energy Report 2015 foresees that at least 26 % will be reached in 2020 [17]. Most likely the renewable energy will be one of the worldwide largest sources of energy by 2020, along with gas and nuclear [17]. Today, the renewable energy market strongly depends on environment, research and development and market support policies [18]. In Europe the renewable energy industry is a world leading sector, particularly in wind and PV [18].

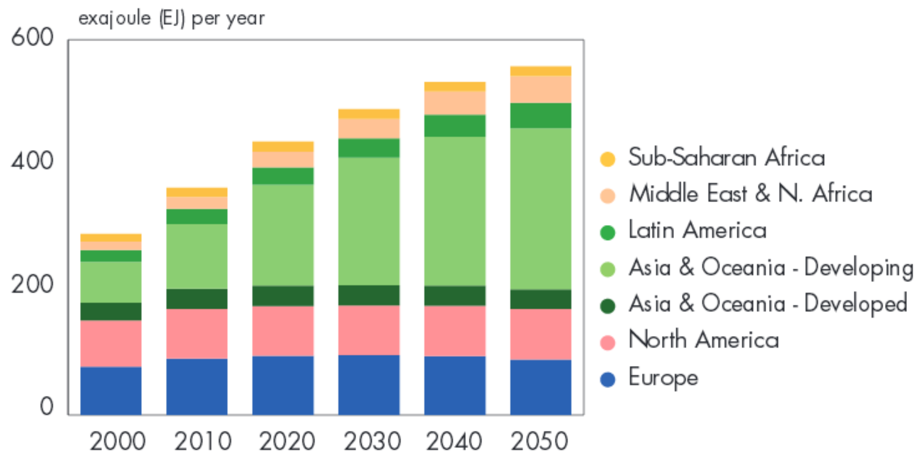

(a)

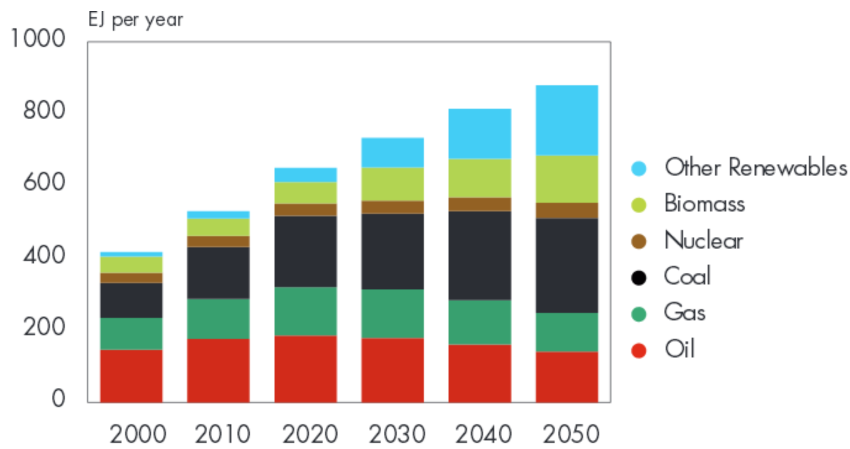

(b)

Figure 1.2: Energy supply scenarios for the next future: *(a)* Energy consumption by regions; *(b)* Primary energy by source [16].

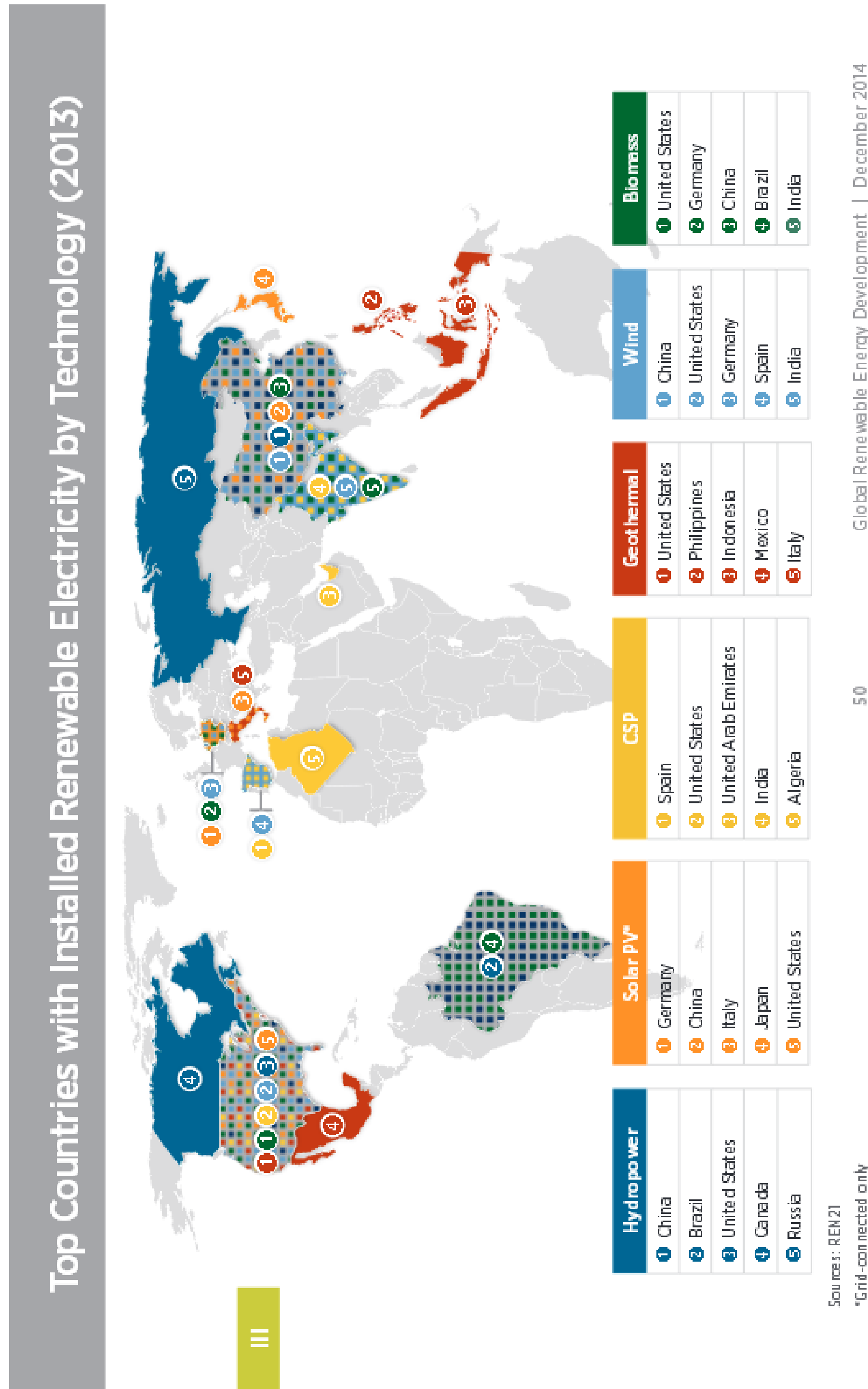

Figure 1.3: Top countries with installed renewable electricity by technology in 2013 according to NREL [19]

1.2 Present status and perspectives of photovoltaics

Among the renewable energies, photovoltaics (PV) is the most promising for the next future. It is non-polluting, requires minimum maintenance and no supervision, and has a long lifetime with low running costs. These and other advantages make PV the best candidate source of renewable energy.

Since 2000, the total production of photovoltaics has increased by almost two orders of magnitude, and the Compound Annual Growth Rate (CAGR) over the last decades has been about 44 % [20]. Figure 1.4 shows the annual PV module production by region from 1997 to 2014. Asia is the country with the most rapid growth in annual production over the last five years, where China and Taiwan today account for more than 70 % of the worldwide production[20]. Figure 1.4 illustrates the evolution of the worldwide percentage production of PV in the main regions around the world. In the last years, new investments continued to rise in Asia. The leading country in new renewable energy investment was China at USD 54.2 billion (EUR 40.2 billion), followed by the USA at USD 36.7 billion (EUR 27.2 billion) [21].

At the present status, the solar cell technologies are well established and provide a efficiency around 20 - 25 %, with an energy output for at least 25 years. Over 85 % of the actual production employs crystalline silicon wafer technology. In the next future, the entry of new technologies in the market will be the main factor to enable further cost reductions. Hence, to maintain a large growth rate of the PV industry, different solar cell technologies must be developed simultaneously [20]. Actually, the majority of thin-film manufacturers remain silicon based and use either amorphous silicon or microcrystalline silicon structure [22].

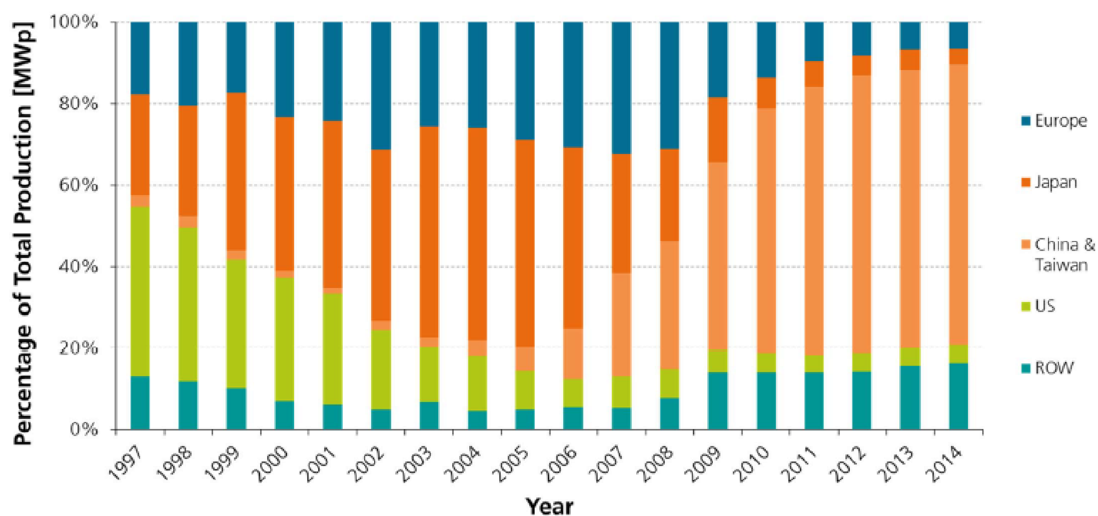

Figure 1.4: PV module production by region: percentage of total MW peak produced from 1997 to 2014 [20].

1.3 The physics of a solar cell

It was in 1839 when Alexandre Edmond Becquerel discovered the photovoltaic effect, which explains how electricity can be generated using light as a source. After attempts with selenium and cuprous oxide solar cells during the 19th century, a first silicon cell was developed in 1941[23]. However, the first solar cell with a reasonable efficiency of 6 % was announced by Daryl Chapin, Calvin Fuller and Gerald Pearson in 1954 [24]. During the first decades, solar cells were mainly used as power sources for space applications. It was in the early 1970s that the interest for the solar cells was reconsidered because of the energetic crisis of oil in the western world[23].

1.3.1 The solar spectrum

Only photons of appropriate energy can be absorbed and generate the electron-hole pairs in the semiconductor material of which is made a photovoltaic device. The energy of the visible photons of which is composed the sun radiation is sufficient to excite electrons to higher energy levels if the target material has an energy gap lower than the photon energy, but these excited electrons quickly relax to their initial ground state. The collection of the charge carriers generated by the sun radiation is performed by a *p-n* junction, which prevents the recombination by using a junction to spatially separate the electrons from the holes [24]. The carriers are separated by an electric field existing at the *p-n* junction. If the two regions of the cell are connected together, the photo-generated carriers flow through the external circuit to produce a current.

Photons incoming from the sun provide an unlimited energy flow for PV power sources. The solar radiation spectrum, i.e. the number of photons as a function of wavelength, can be described by two parameters, namely the spectral power density $P(\lambda)$ and the photon flux density $\Phi(\lambda)$. The spectral power density is defined as the incident radiation power per unit area and per unit wavelength. The photon flux density is the number of photons per unit area, per unit time and per unit wavelength. These two quantities are related by the following equation [1]:

$$\Phi(\lambda) = P(\lambda)\frac{\lambda}{hc} \quad (1.1)$$

Figure 1.5 shows the spectrum distribution of the solar radiation with various absorption peaks associated to the presence of air molecules in the atmosphere. The temperature at the center of the sun can reach 10^6 K, while on the surface is about 6000 K. The sun radiation can be approximated to that of a 6000 K black body (i.e. a perfect emitter and absorber of electromagnetic radiation), due to the near total absorption of radiation by the photosphere. The total power density of the solar radiation at the mean earth-sun distance on a surface normal to the sun direction and outside the earth's atmosphere defines the *solar constant* or air mass zero (AM0) radiation. Its value is a

constant parameter: 1353 kW/m^2 [1]. The earth's atmosphere attenuates the solar radiation over the 30 %. This is due to absorption and scattering by air molecules, dust particles and aerosols in the atmosphere. Oxygen and CO_2 are among the main cause of absorption, which acts as a wavelength filter. As a result, a different solar spectrum can be measured at the earth's surface, with the presence of gaps (e.g. ozone filters solar radiation with wavelength below 0.3 μm) [1], as depicted in Figure 1.5. The importance of this can be understood considering that the wavelength of the incoming solar radiation varies significantly the response of a solar cell. Except from the weather conditions, the main parameter that determines the solar spectrum at the earth's surface is the distance that the sunlight has to travel through the atmosphere.

The ratio between an actual distance and the minimal path length when the sun is at the zenith is called the *air mass*. When the path length is the shortest, with the sun at the zenith, it corresponds to air mass one (AM1). At an angle θ respect to the zenith, the air mass can be defined as follows:

$$AM = \frac{1}{cos\theta} \quad (1.2)$$

The terrestrial solar radiation standard has been defined AM1.5, because of the variability of terrestrial light and to allow comparisons between the performances of solar cells at different locations. The AM1.5 radiation has a power density content of 1000 W/m^2, which is close to the maximum irradiance at the earth's surface. However, the total solar radiation that reaches a particular region on the earth is extremely variable. The diffuse component of the solar radiation, which originates from the scattering with the air molecules in the atmosphere, represents about the 15 % of the total sunlight. The spectrum distribution of the diffuse part consists mainly in the shorter wavelengths. For these reasons, an optimal PV device must be designed depending on the solar radiation availability for each particular location.

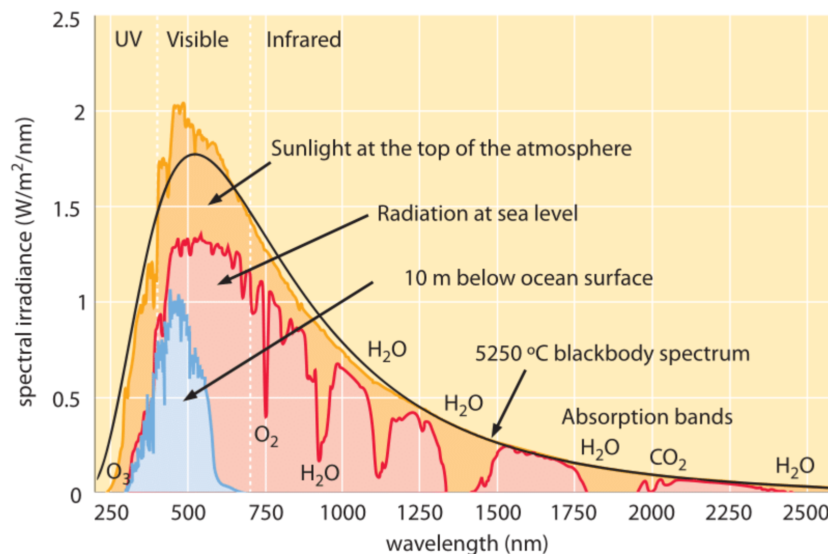

Figure 1.5: Spectrum distribution of solar radiation with various absorption peaks due to the presence of the atmosphere (labeled with the associated molecular species) [25].

1.3.2 *I-V* characteristic and main definitions of a solar cell

A PV device, or solar cell, involves a contact with different electronic properties that pulls the excited electrons away before they can relax, bringing them to an external circuit. The output potential difference obtained results from the extra energy of the excited electrons, and can be used to do electrical work. The efficiency of the solar cell is directly related to the choice of light absorbing materials and their connections to the external circuit [24]. The incoming photons are absorbed by the material to generate charge carriers. The rectifying properties of the solar cell drive the carriers toward the external circuit. An open circuit photo-voltage is made up in this way, and if the terminals are connected a short circuit photocurrent is generated. If a load is connected to the external circuit the cell delivers both current and voltage, which product gives the output power [24].

A solar cell develops a voltage when it is under illumination conditions, for this reason, the surface of a solar cell must result the less reflective as possible in order to absorb the largest amount of radiation. When the terminals are isolated, meaning an infinite load resistance is placed in the circuit, the voltage is called the *open circuit voltage* V_{oc}. The current originating when the terminals are connected together without a load is called the *short circuit current* I_{sc}. Introducing an intermediate load resistance R_L, the cell develops a voltage between 0 and V_{oc} and generates a current $I(V)$ determined by the current-voltage characteristic of the cell under illumination. The photocurrent density results proportional to the illuminated area, as follows by the relation [24]:

$$J_{sc} = q \int \Phi(E) QE(E) dE \tag{1.3}$$

where $QE(E)$ is the probability that an incident photon of energy E to send one electron to the external circuit, $\Phi(E)$ is the incident photon flux density and q the charge of the electron. The quantity QE is called the quantum efficiency and depends on the absorption coefficient of the solar cell material but not on the incident spectrum, which makes it a key quantity in investigating solar cell performance under different conditions [24]. Figure 1.6 shows the QE spectrum of various types of solar cells.

A solar cell in the dark under *I-V* measurements produces an exponential curve that is characteristic of diode, which is called the *dark current* $I_{dark}(V)$, and possesses an opposite direction respect to the photocurrent. It reduces the net current from the short circuit value. The dark current is also defined as the *I-V* characteristic of the solar cell under dark conditions, and it results much smaller than the current that it is developed under illumination. This rectifying behavior is the reason for which a solar cell is modeled like a diode. The dark current density for an non-ideal diode results [24]:

$$J_{dark}(V) = J_0 (e^{\frac{qV}{Ak_BT}} - 1) \tag{1.4}$$

where J_0 is the reverse saturation current of the associated diode, A is the ideality factor, k_B is the Boltzmann's constant and T is the temperature.

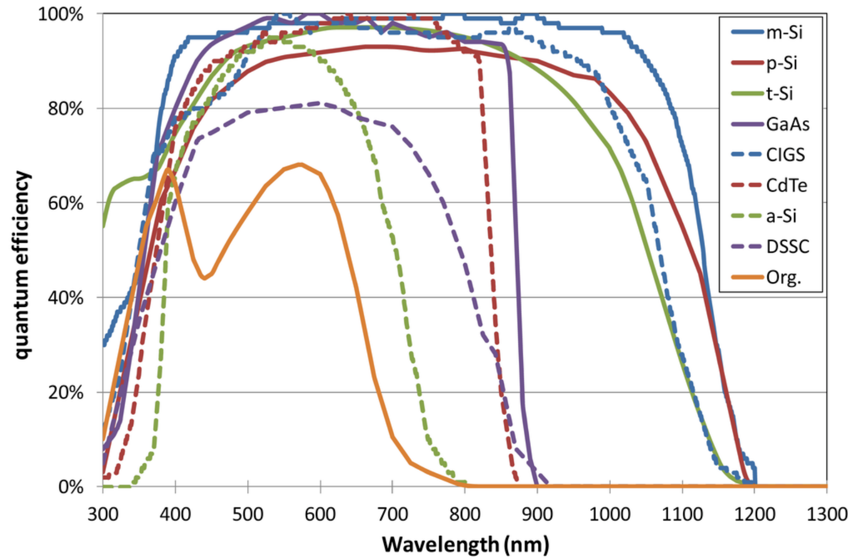

Figure 1.6: Quantum efficiency of different technology based solar cells [26].

The expression of the net current can be approximated by the sum of the short circuit photocurrent and the dark current. This step is known as the superposition approximation, which is reasonable for many PV materials. Figure 1.7 shows the *I-V* characteristic of the solar cell under dark and light conditions. Therefore, the net current density is given by:

$$J(V) = J_{dark} - J_{sc} \tag{1.5}$$

where the sign of the circuit photocurrent is conventionally taken negative in PV. Substituting the expression for $I_{dark}(V)$ in *Eq*. (1.5), the net current density results:

$$J = J_0(e^{\frac{qV}{Ak_BT}} - 1) - J_{sc} \tag{1.6}$$

When the dark current and the short circuit photocurrent exactly cancel out, the potential difference reaches its maximum, which is the open circuit voltage V_{OC} that increases logarithmically with the light intensity, as shown by the following relation [24]:

$$V_{oc} = \frac{Ak_BT}{q} ln\left(\frac{J_{sc}}{J_0} + 1\right) \tag{1.7}$$

When the cell is under illumination, it generates a photocurrent that is proportional to the light intensity. The voltage must lie between 0 and V_{oc} for the cell to generate power, which is the current-voltage product given by:

$$P = JV \tag{1.8}$$

The cell's maximum operating point for P occurs at the voltage V_m, corresponding to a current density J_m, as shown in Figure 1.7

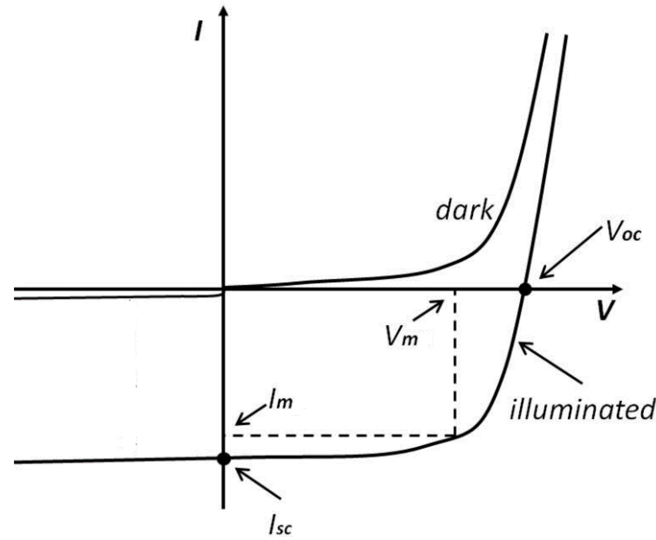

Figure 1.7: Current-voltage characteristic of the diode associated to a solar cell in dark and light conditions [27].

The ratio of the maximum power from the solar cell and the product of V_{oc} and J_{sc} is defined as the fill-factor (*FF*) [24]:

$$FF = \frac{J_m V_m}{J_{sc} V_{oc}} \tag{1.9}$$

The *FF* is a measure of the 'squareness' of the solar cell *J-V* curve. A fundamental quantity for characterize a solar cell is the efficiency η of the cell, defined as the ratio of power output from the solar cell to the incident light power density P_{il}:

$$\eta = \frac{J_m V_m}{P_{il}} \tag{1.10}$$

The efficiency is the most commonly used parameter to compare the performance of different solar cells.

In the equivalent circuit shown in Figure 1.8, the solar cell is modeled as a current generator in parallel with a non-linear resistive element with rectifying properties, i.e. a diode. For a non-ideal cell, the power is dissipated in various ways. The power dissipation of a solar cell can be modeled considering two parasitic resistances, namely the series (R_s) and shunt (R_{sh}) resistances. Figure 1.8 shows the equivalent circuit for a real solar cell, while Figure 1.9 depicts the effects of the series and shunt resistances on the *I-V* curve. The main causes of the presence of series resistance involve the contact resistance between the metal and the semiconductor [28]. The shunt resistance is typically due to manufacturing defects, meaning the leakage of current through the cell [24]. The impact of both the series and shunt resistances in a solar cell is to reduce the *FF*. In order to have an efficient cell, a small R_s and a large R_{sh} are required.

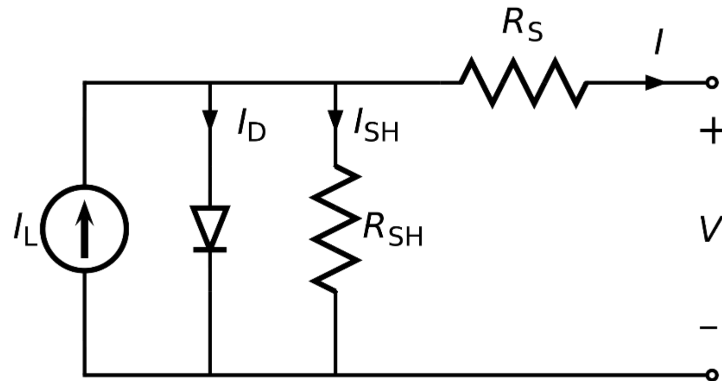

Figure 1.8: Schematic view of the equivalent circuit for a non-ideal solar cell including series and shunt resistances [29].

Including the parasitic resistance in the Eq. (1.6), the diode equation results [24]:

$$J = J_0\left(e^{\frac{q(V+JR_s)}{Ak_BT}} - 1\right) - J_{sc} + \frac{V + JR_s}{R_{sh}} \quad (1.11)$$

The four quantities J_{sc}, V_{oc}, FF and η define the main characteristics of a solar cell performance. Measurements made on these parameters must be performed at the same illumination conditions to compare different solar cells. The efficiency depends on the spectrum and intensity of the incident sunlight, and the temperature of the solar cell. Hence, conditions under which efficiency is measured must be carefully controlled in order to compare the performance of one device to another. Terrestrial solar cells are measured under AM1.5 conditions, at a temperature of 25 °C, and with an incident power density of 1000 W/m^2. This set of parameters is called the Standard Test Condition (STC). Solar cells intended for space use are measured under AM0 conditions [24].

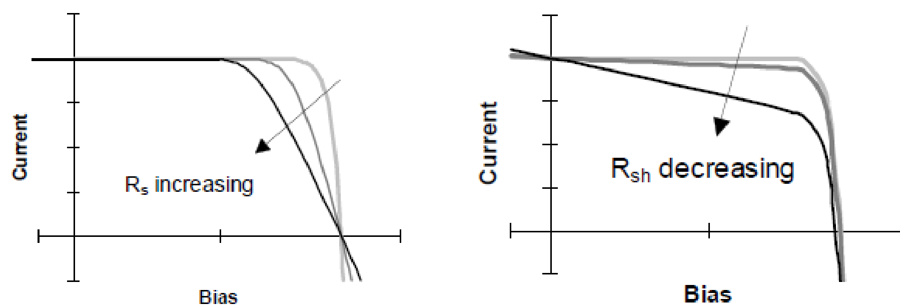

Figure 1.9: *I-V* curve of a solar cell with increasing series (R_s) and decreasing shunt (R_{sh}) resistances. The effect of both resistances is to reduce the *FF* of the cell [24].

1.3.3 Homojunctions and heterojunctions

Solar cells use several junction types, all of them with the aim of generating the electric field that acts to separate the charge carriers to extract them in the external circuit. The main devices used for PV applications are the homojunction and the heterojunction [30]. Figure 1.10 *(a)* and *(b)* show the energy band diagram for a homojunction and a heterojunction, respectively.

A homojunction occurs at the interface between the two parts of a semiconductor material, one n-doped and the other p-doped, are brought in contact to each other. The n-doped region has a high negative charge concentration, meaning electrons, and the p-doped region a high positive charge concentration, meaning holes. When the two regions are in contact, electrons diffuse from the n-doped to the p-doped region, while holes flow in the opposite direction. As the carriers diffuse, positive ions in the n-doped side, as well as negative ions in the p-doped side, will form at the junction [30]. Hence, a band bending will occur at the interface between the two doped regions because of the Fermi levels pinning. Then, an electric field is generated at the junction, which sweeps free carriers out. This region is called the *depletion region*. A *built in* potential difference due to the electric field is then formed at the junction. This diffusion potential is equal to the difference between the work functions of the two doped regions as follows [30]:

$$V_{diff} = e\phi_{diff} = e(\phi_{w_p} - \phi_{w_n}) \qquad (1.12)$$

The work function of a material can be defined as the external energy required to extract an electron from the material, meaning the energy difference between the Fermi level of the material E_F and the vacuum level E_{vac}:

$$e\phi_w = E_{vac} - E_F \qquad (1.13)$$

If the energy of the incoming photons is larger than the forbidden gap of the semiconductor, namely the energy gap E_g, free minority carrier electrons in the p-doped region and free minority carrier holes in the n-doped region then originate. These minority carriers diffuse toward the junction, where they can recombine with each other or continue to diffuse until they reach the external circuit and generate current. For this reason, a typical homojunction is realized using a thin layer (~0.1μm) for the illuminated part [30]. This allows the radiation to penetrate deep in the junction. However, a very thin layer with a high surface to volume ratio could rise some issues because of the large number of surface states that acts as recombination sites for the carriers.

A heterojunction is made of two different semiconductor materials, having different energy gaps and electron affinities. For a semiconductor, the electron affinity χ is defined as the energy obtained moving an electron from the vacuum level to the bottom of the conduction band. A fraction of the incoming photons penetrates through the n-doped region toward the p-doped region, thus increasing the radiative absorption. This is due to the lower energy gap of the n-doped region respect to the energy gap of the p-doped region [30]. However, the use of different semiconductor materials inevitably leads

to reticular mismatch at the junction, which increases the probability of recombination for the free-moving charges. Figure 1.10 shows a heterojunction where $E_{g1} < E_{g2}$ and with the same doping level for the two parts in order to have the same width for the depletion regions. In solar cells using a heterojunction device, the top layer acts as a window layer, that is a material with a high energy gap, which is transparent to the low energy photons. Almost all incident light can penetrate the window layer to reach the bottom layer, which is a material with a low energy gap to absorb another fraction of the photons [30].

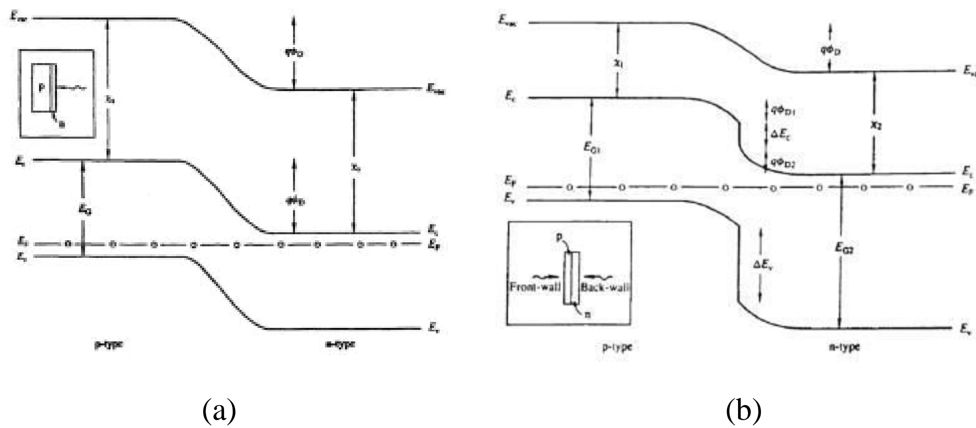

(a) (b)

Figure 1.10: Energy band diagram: *(a)* p-n homojunction (χ_s is the electron affinity); *(b)* p-n heterojunction ($\chi_1 < \chi_2$ and $E_{g1} < E_{g2}$); The different regions of both the junctions possess the same doping level [30].

1.3.4 The Shockley-Queisser limit

From thermodynamics, the maximum theoretical limit of efficiency for a solar cell is given by a Carnot heat engine operating between the sun temperature (~6000 K) and the cell temperature (~300 K). However, the highest efficiencies reached for solar cells are much lower than the thermodynamic limit, depending on the energy gap, the optical material properties such as the absorbance and geometrical factors.

In 1961, William Shockley and Hans Queisser showed that a lower theoretical limit of efficiency exists for a single p-n junction solar cell, which is known as the Shockley-Queisser (SQ) limit. The SQ limit is derived from the detailed balance principle. In this assumption, the photons absorbed by the solar cell must be compensated by the thermal emission of less energetic photons, since both the hole-electron pair creation and recombination processes are possible [24]. The main factors considered by the SQ limit include the black body radiation, the radiative recombination and the energy gap. To improve efficiency, a solar cell must have a high absorption coefficient, which permits

the cell to be modeled as a black body. Then, at thermal equilibrium a black body radiation is emitted by the cell depending on its temperature. The photons emitted by the cell cannot be re-absorbed, resulting in a loss of the available incoming energy [24]. The radiative recombination between holes and electrons is then considered. Even if the radiative recombination is only a fraction among all possible recombination events, then the efficiency of the cell will be reduced with respect to the maximum possible value. The energy gap of the solar cell material is another important parameter that contributes to reduce the efficiency limit [31]. Since only photons with an energy higher than the energy gap of the device can generate hole-electron pairs, photons of lower energy do not contribute to the electrical output power of the cell. Moreover, photons with a high energy do not provide their whole energy to the device, since the electrons lose this extra energy by Joule effect, converting it to heat. This provides the main efficiency loss factor for the solar cells. In addition to the radiative recombination considered in the SQ limit, other sources of recombination must be taken into account. Surface recombination plays an important role in reducing the efficiency of thin films solar cells. For this reason, a buffer layer is used in order to passivate the surface and reduce the recombination rate [4]. Figure 1.11 shows the maximum theoretical efficiency with the energy gap of absorber materials reported for comparison.

In the SQ model, the efficiency η is expressed as a function dependent upon four different variables [31]:

$$\eta = \eta(x_g, x_c, t_s, f) \tag{1.14}$$

where t_s is the probability that an incident photon with energy higher than E_g will generate a hole-electron pair, the factor f represents all other parameters (i.e. those involving transmission of radiative recombination and the solid angle subtended by the sun), x_c is the ratio between the temperature of the cell and that of the sun:

$$x_c = \frac{T_c}{T_s} \tag{1.15}$$

and x_g is the ratio of the energy gap E_g to the energy associated to the sun temperature:

$$x_g = \frac{E_g}{kT_s} \tag{1.16}$$

Efficiency can then be written as follows:

$$\eta\left(x_g, x_c, t_s, f\right) = t_s u(x_g) v(f, x_c, x_g) m(v x_g / x_c) \tag{1.17}$$

where u is the ultimate efficiency (according to an ideal photoelectric process with a

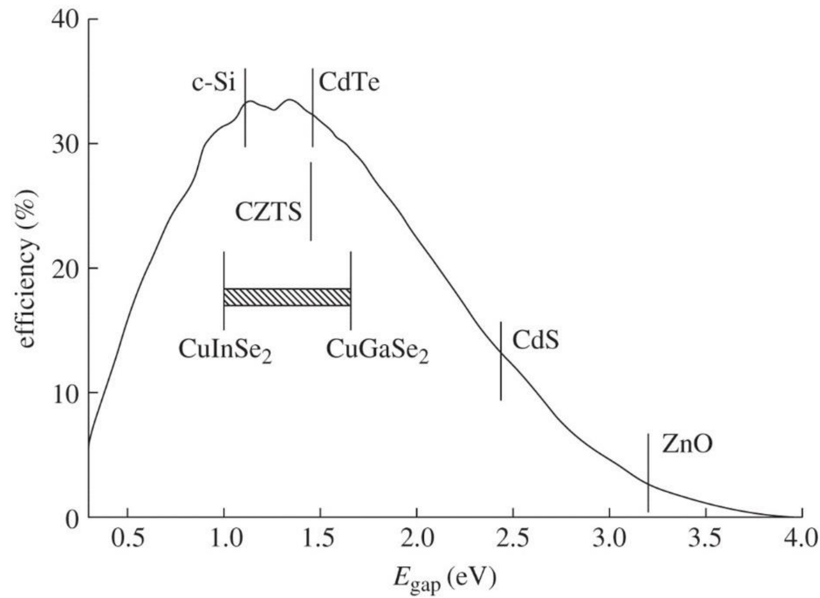

Figure 1.11: Efficiency as a function of the energy gap E_g showing the maximum theoretical value (the SQ limit) for solar cells under AM1.5 illumination conditions without concentration. The energy gaps of absorber materials (c-Si, CdTe, CIGS, CZTS) and window materials (CdS, ZnO) are shown for comparison [32].

single cutoff frequency in a device maintained at 0 K with a 6000 K black-body radiation surrounding it), v is the ratio of the open-circuit voltage to the energy gap of the cell and m is the impedance matching factor, which is a function of the ratio of the ratio of the open-circuit voltage to thermal voltage for the cell [31].

The SQ model proves that a maximum efficiency of 33 % results for solar cells with an energy gap E_g of 1.35 eV under AM1.5 illumination conditions. Suitable absorber materials that have energy gaps in this range include CdTe (1.44 eV) and $CuInGaSe_2$ (CIGS) solutions, which energy gap can be tuned by controlling the In/Ga ratio [32]. Monocrystalline silicon solar cells have already achieved efficiencies close to the SQ limit, while thin films solar cells still have to be improved.

1.3.5 Surface passivation

The surface or interface of a semiconductor possesses discontinuities in the crystalline structure. The partially bonded atoms give rise to many dangling bonds, resulting in a large density of defect levels (or surface states) found within the energy gap at the semiconductor surface. The process of reducing these dangling bonds is

known as surface passivation. The rate of surface recombination U_s, for a single defect can be derived from the Shockley-Read-Hall formalism, given by [33]:

$$U_s = \frac{n_s p_s - n_i^2}{\frac{n_s + n_1}{S_{p0}} + \frac{p_s + p_1}{S_{n0}}} \tag{1.18}$$

where n_s and p_s are the concentrations of electrons and holes at the surface, n_1 and p_1 statistical factors, S_{p0} and S_{n0} are related to the density of surface states per unit area N_{ts}, to the capture cross-sections σ_n and σ_p, and to the thermal velocity v_{th} for the specific defect:

$$S_{n0} = \sigma_n \, v_{th} N_{ts}$$

$$S_{p0} = \sigma_p \, v_{th} N_{ts} \tag{1.19}$$

The recombination lifetime τ and the surface recombination velocity S are defined as:

$$\tau(\Delta n) = \frac{\Delta n}{U(\Delta n)}$$

$$U_s = S \Delta n_s \tag{1.20}$$

where Δn is the excess minority carrier concentration and Δn_s is the excess minority carrier concentration at the surface. Neglecting carrier trapping, the excess densities of electrons and holes are equal ($\Delta n_s = \Delta p_s$), which gives [33]:

$$S(\Delta n_s) = \frac{n_0 + p_0 + \Delta n_s}{\frac{n_0 + n_1 + \Delta n_s}{S_{p0}} + \frac{p_0 + p_1 + \Delta n_s}{S_{n0}}} \tag{1.21}$$

The quantity S defines the surface recombination velocity that is typically used for quantifying surface recombination processes. A high surface recombination velocity can have a large impact on both the short circuit current and the open circuit voltage since it reduces the minority carrier lifetime. Figure 1.12 *(a)* and *(b)* show simulations of the open-circuit voltage V_{oc} as a function of the effective rear surface recombination velocity S_{eff} for solar cells having different cell thickness, in the case of high-efficiency silicon solar cells with a higher minority carrier lifetime τ_{bulk} = 750 µs and medium-efficiency silicon solar cells with a lower minority carrier lifetime τ_{bulk} = 100 µs, respectively. The result of both trends is an increased importance of an effectively passivated rear surface. It results that the influence of the rear passivation increases when the cells are getting thinner [34].

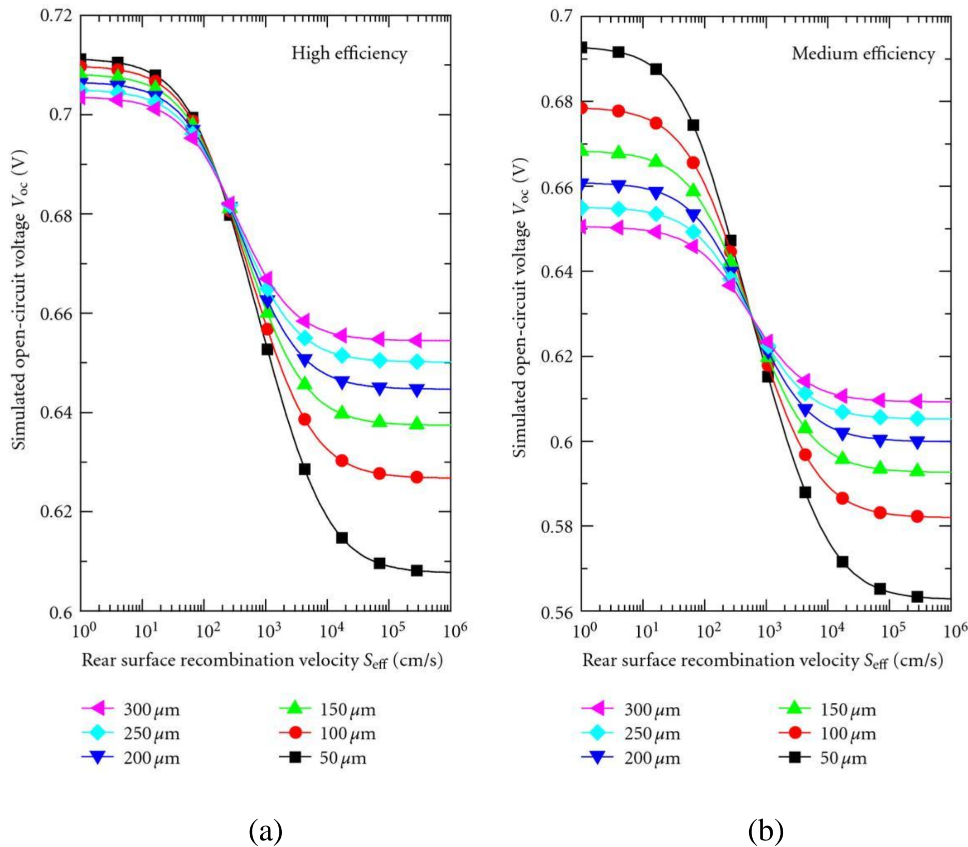

Figure 1.12: Simulations of the open-circuit voltage V_{oc} as a function of the effective rear surface recombination velocity S_{eff} for a-Si solar cells having different thickness, in the case of high-efficiency cells (τ_{bulk} = 750 μs) *(a),* and medium-efficiency cells (τ_{bulk} = 100 μs) *(b)* [34].

There are typically additional extrinsic surface defects, due to dislocations or chemical residues and metallic depositions on the surface. These defects are sites of several recombination mechanisms, namely surface recombination, Auger recombination and Shockley-Read-Hall (SRH) recombination [33]. Thus, passivation of the cell interfaces improves the efficiency. Figure 1.13 shows the external quantum efficiency spectrum of a Cu(In,Ga)Se_2 (CIGS) rear passivated solar cell with different Al_2O_3 passivation layer thickness. Actually, the presence of passivation layers in thin film solar cells technology is essential for efficiency increase, making the implement of an effective passivation method a near-term challenge in the PV industry.

Recombination losses at a semiconductor interface or surface can be reduced by two different passivation strategies. The first is to reduce the number of defects states at the interface by the growth of thin dielectric or semiconductor films. This method is known as the chemical passivation. The second strategy is the significant reduction of the electron or hole concentration at the interface, by means of a built in electric field [33]. This electric field can be obtained by either a doping profile below the interface or the

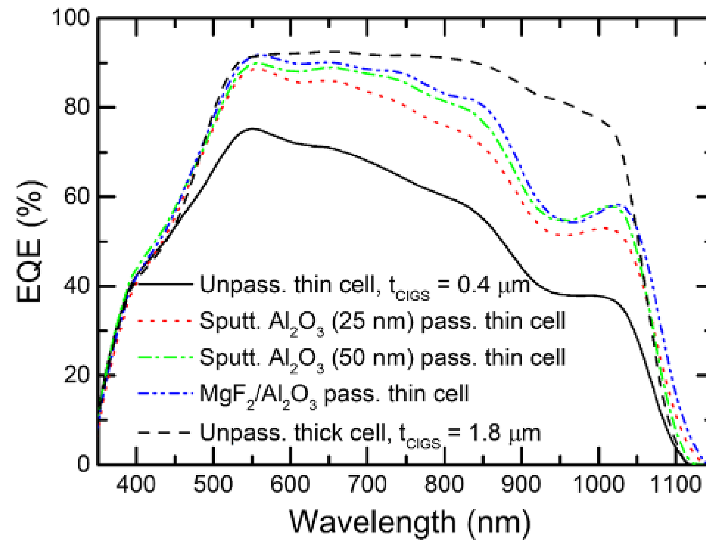

Figure 1.13: External quantum efficiency (EQE) as a function of the wavelength for a non-passivated and Al_2O_3 rear surface passivated $Cu(In,Ga)Se_2$ (CIGS) solar cell [35].

presence of fixed electrical charges at the semiconductor interface. As a result, field-effect passivation has limited applications but the effect can be employed successfully.

In silicon heterojunction solar cells, the passivation is obtained by placing a buffer layer with a larger energy gap between the metal contacts and the active material. In this way the open circuit voltage results increased and higher efficiencies can be reached with lower costs. The passivating layer at the front of the cell is often referred to as the window layer because it should have a high transmittance to let the photons passing through. These buffer layers with a higher energy gap have the role of a semi-permeable membrane for carrier extraction [4]. Front surface passivation is typically obtained by chemical vapor deposition of SiO_2 and TiO_2 layers. However, this requires very high temperature treatment, which degrades the bulk lifetime significantly as well as the stability of the passivated surface. In addition, SiO_2 has a very low refractive index and it is not a suitable choice for high antireflection coatings. Regarding TiO_2, it does not provide any electronic surface passivation[33]. Al_2O_3 has been found as an alternative material for rear passivation of high-efficiency silicon solar cells [33].

Recently, has been demonstrated that an exceptional high-level of c-Si surface passivation can be achieved for SiO_2 synthesized at low temperatures when combined with a very thin Al_2O_3 capping film. The excellent efficiencies reached (up to 21.3-21.5 %), the high voltages (680 mV), the large quantum efficiency and the high short circuit currents of these cells (40 mA/cm^2) have showed the low rate of surface recombination for these devices [33].

1.4 Solar cells generations

The first generation solar cells dominated the PV market until the recent years. These devices rely upon high volumes bulk mono-crystalline or poly-crystalline silicon wafers. However, the costs of the materials represent over a half of the total manufacturing costs, with little potential in cost reduction. The basic structure scheme of a c-Si cell is depicted in Figure 1.14.

Silicon solar cells have commercial efficiencies that are limited to around 20 % [36]. The efficiency of these cells is approaching the theoretical limit of 29.4 % calculated by recent studies [37]. Although efficiency of mono-crystalline silicon (c-Si) solar cells is higher than poly-crystalline silicon (pc-Si) solar cells, production of poly-crystalline silicon wafer is easier and cheaper, making them competitive with mono-crystalline ones [38].

These cells use two different *p*-type substrates: c-Si and pc-Si. The surface is textured to reduce the efficiency losses associated to incident light reflection. In addition, an anti-reflection (AR) coating of silicon nitride (SiN) or titanium oxide (TiO) is used in order to obtain the maximum reduction of reflectivity. The p-n junction is obtained by a phosphorous doped *n*-type region on the front surface of the cell and a boron doped *p*-type substrate. The silver contacts on the front and on the back of the silicon surface collect mobile electrons generated in the silicon bulk and diffusion layers [39].

The second generation of solar cells consists of thin films technology, including amorphous silicon, CdTe and $CuInGaSe_2$ (CIGS). The primary aim of these devices is to reduce material costs by using cheap semiconductor thin films deposited on low cost substrates to provide acceptable efficiencies of about 10-15 %. CdTe, CIGS and a-Si absorb the solar spectrum much more efficiently than c-Si or pc-Si and use only 1-10 μm of active material [36]. The thin-film technology is cheaper but less efficient than the first generation solar cells technology.

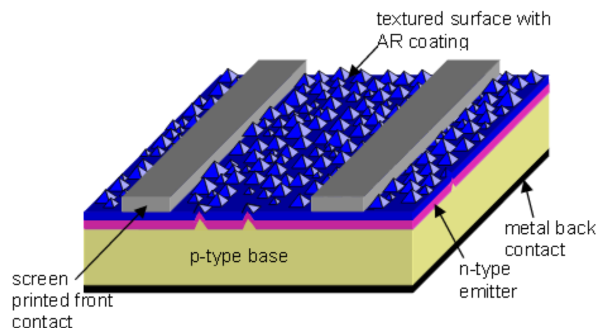

Figure 1.14: Schematic view of a first generation mono-crystalline silicon solar cell [36].

However, the ratio of efficiency to cost results competitive today. In recent years, significant improvements of the thin film technology have been performed, with efficiencies reaching 21 % for CdTe and CIGS devices [20]. Figure 1.15 shows the basic scheme of CdTe, CIGS and a-Si thin film PV devices.

Despite these results, the market of all thin-film technologies has been declining in the last years to about 9 % of the total annual production, while 85 % is held by crystalline silicon [20]. In Figure 1.16 the efficiencies reached as a function of the cost for the three generations of solar cells technology are shown.

The structure of both CdTe and CIGS thin film solar cells includes a *n*-type CdS buffer layer grown by chemical bath deposition on the *p*-type absorber. The front contact (usually TCO for CdTe and a-Si, ZnO for CIGS cells) serves as a transparent conducting material that collects and delivers the electrons to the external circuit [40].

A third generation of solar cells has been developed in the last years exceeding the SQ limit, with reached efficiencies of over 40 %. The main third generation devices include multi-junction (*tandem*) cells developed in the early 1960s. The tandem cell concept lies in splitting the solar spectrum in ranges of energy in order to use several junctions for the energy conversion. If this technology can be improved reducing the costs, the next future market will be dominated by the third generation solar cells [41].

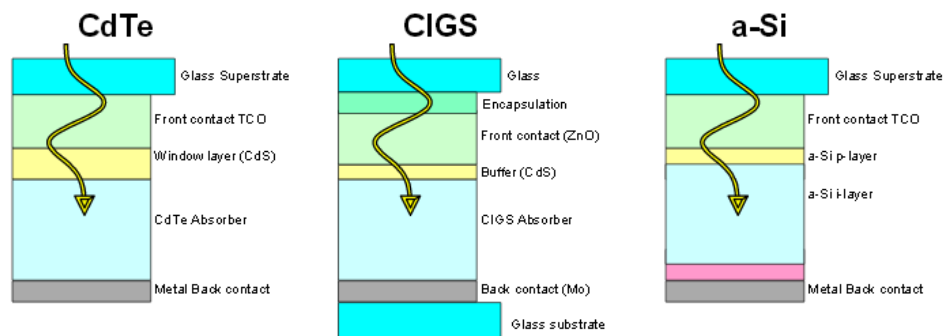

Figure 1.15: Schematic view of thin film solar cells using CdTe, CIGS and a-Si thin film PV devices [36].

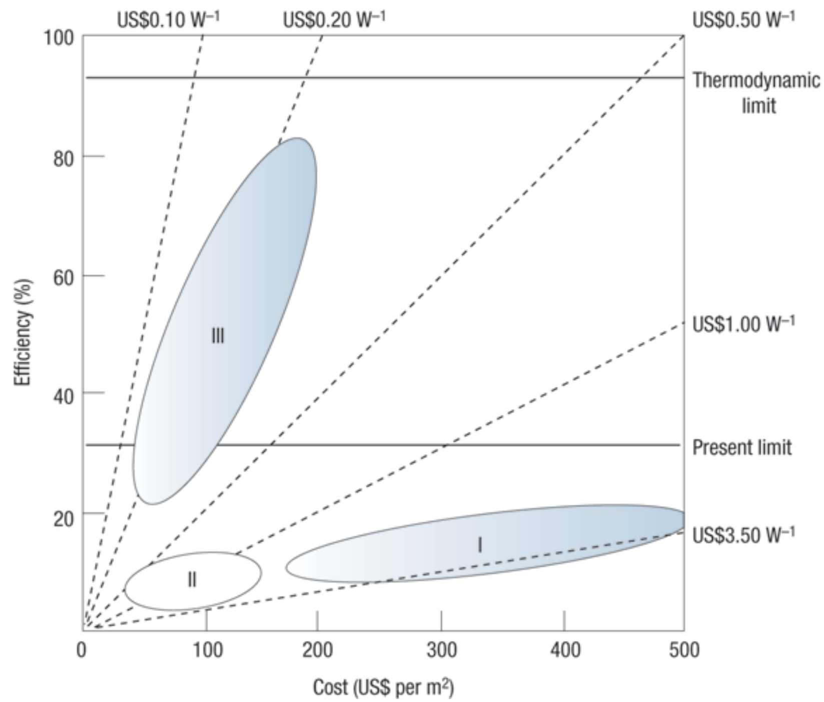

Figure 1.16: Efficiency limits of the three generations of photovoltaic cells technology (wafers, thin films and multi-junction) as a function of the areal cost in US$ [42].

Chapter 2
Zinc Sulfide State of the Art

Zinc sulfide (ZnS) exhibits interesting properties that have not yet been much investigated. ZnS thin films have been found useful in various devices, covering a wide area of applications, including antireflection coating for the solar cells, non-toxic buffer layer (compared to CdS layer in CIGS based thin film solar cells), wide energy gap material for electroluminescent and opto-electronic devices, photosynthetic coating and blue emitting laser diodes [7]. In this section, an overview of the actual state of the art about the ZnS properties and applications, with particular attention for the field of photovoltaics, has been reported.

2.1 Main characteristics

Zinc sulfide (ZnS) is among the first semiconductor materials discovered [43]. It results peculiar in various fundamental properties, i.e. a wide energy gap and a high transmittance. It results also a promising alternative material for different applications, including photovoltaic and optoelectronic devices. Its atomic structure and chemical properties are comparable to another Zn compound: ZnO [43]. Nevertheless, ZnS exhibits properties that are more advantageous with respect to ZnO. ZnS possesses a larger energy gap (in the range 3.5 - 3.9 eV) than ZnO (~3.4 eV) [43]. For this reason, ZnS is more suitable for UV-light based devices such as photosensors, and even more for electroluminescence devices. In addition, ZnS is non-toxic, abundant and cheap. Actually, the properties of ZnS have not yet been investigated in much detail, making this material an actual field of research for further studies.

2.1.1 Crystal structure

ZnS is found in nature in the mineral of sphalerite. It has commonly two available allotropes: the *zinc blende* (ZB) cubic form, which is more stable, and the *wurtzite* (WZ) hexagonal form. The ZB structure results in tetrahedrally coordinated zinc and sulfur atoms stacked in the ABCABC pattern, while the WZ form has the same structure with atoms stacked in the ABABAB pattern [43]. Figure 2.1 *(a)* and *(b)* shows three different views of the ZB and WZ structures, respectively. The lattice parameters of WZ are $a = b = 3.82$ Å, $c = 6.26$ Å and those of ZB are $a = b = c = 5.41$ Å. The energy gap difference between the two structures is about 0.05 eV [43]. The optical spectra, being related to the energy band structure, also results different.

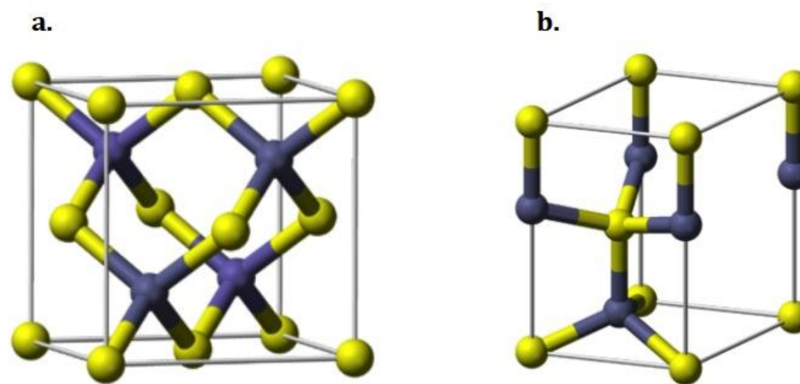

Figure 2.1: Schematic view of the zinc blende *(a)* and wurtzite *(b)* crystal structures for the zinc sulfide [44].

2.1.2 Optical properties

Zinc sulfide has a high refractive index of about 2.35 at wavelength of 632 nm [45]. Figure 2.2 *(a)* and *(b)* show the transmittance and the absorbance, respectively, of ZnS thin films deposited by Successive Ionic Layer Adsorption and Reaction (SILAR) at different annealing temperatures. The absorbance is low in the visible and near infrared regions, but is high in the UV region, with an enhanced absorption observed close to 360 nm [7]. The transmittance is very high in the visible and near infrared regions, and low in the UV region. The high transmittance of about 90 % in the visible range show in Figure 2.2 *(a)* leads to the conclusion that the ZnS films are actually efficient transmitting and antireflective materials. Figure 2.3 *(a)* shows the plot of $(\alpha h\nu)^2$ (where α is the optical absorption coefficient and $h\nu$ is the energy of the incident photon) as a function of the photon energy. Figure 2.3 *(b)* shows the energy gap as a function of the temperature.

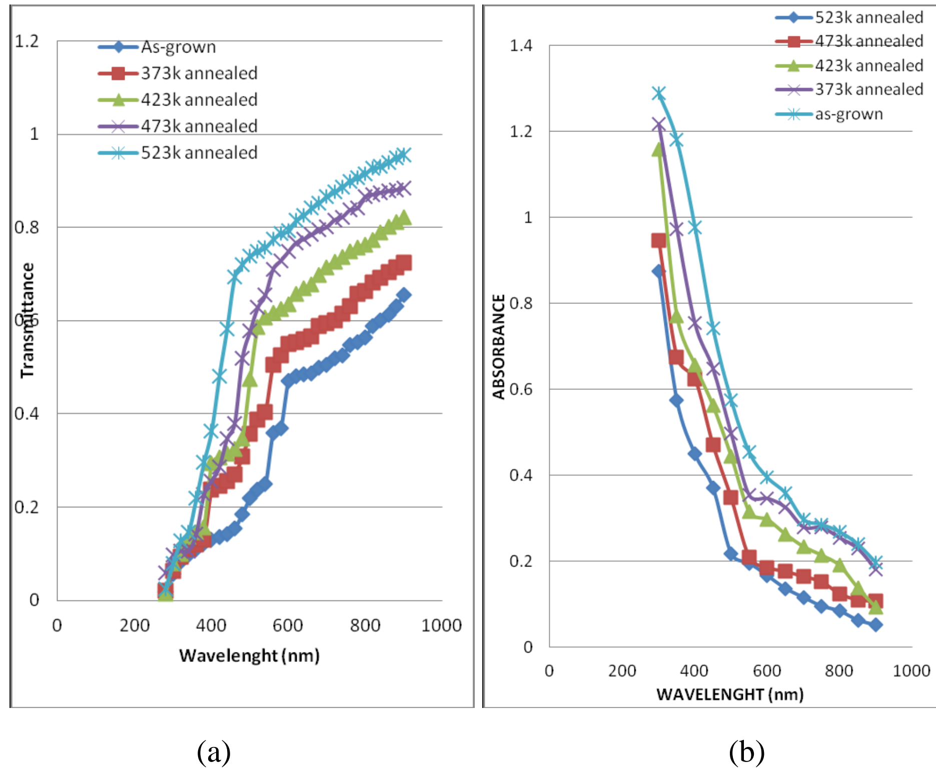

(a) (b)

Figure 2.2: Transmittance (a) and absorbance (b) as a function of the wavelength for ZnS thin films deposited by SILAR at different annealing temperatures [7].

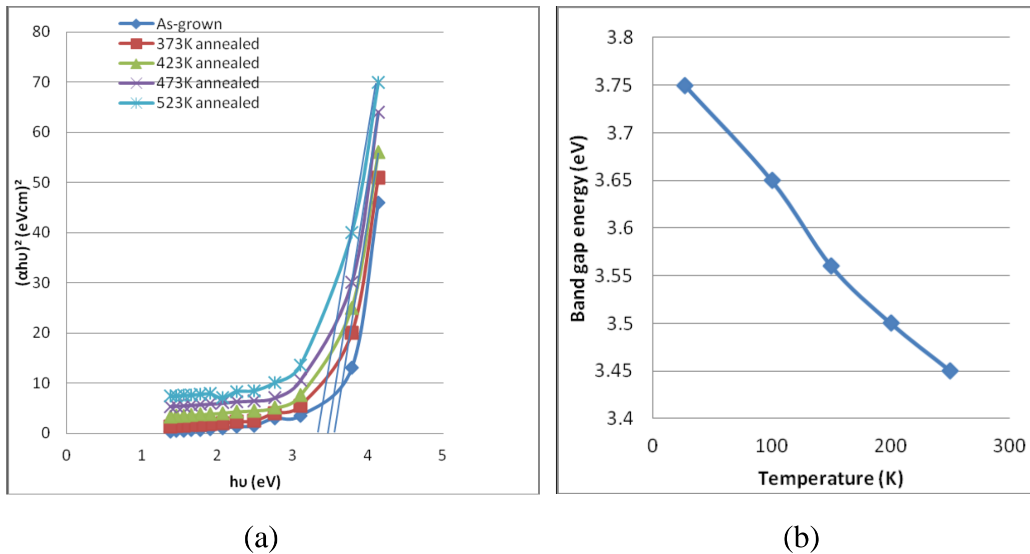

(a) (b)

Figure 2.3: $(\alpha h\nu)^2$ as a function of the photon energy *(a)* and energy gap as a function of temperature *(b)* for ZnS thin films deposited by SILAR at different annealing temperatures [7].

The decrease in energy gap with increasing annealing temperature could be attributed to improvement in the crystal quality or to possible variation of the grain size [7]. Because of these optical properties, ZnS may play an important role in photovoltaic devices as buffer layers in CIGS thin film solar cells.

2.1.3 Dielectric properties

Dielectric studies show that the conduction phenomenon in ZnS nanostructures depends on the temperature and the frequency of the external electric field applied [46]. The dielectric constant decreases with an increase in the frequency. In addition, it results much higher than that of the bulk ZnS, which can be treated as an insulator [46]. Therefore, the conductivity has the inverse trend. Figure 2.4 shows the dielectric constant and the conductivity plots of ZnS nanostructures as a function of the frequency. All the inhomogenities and defects, together with other phenomena such as space charge formation, produce an absorption current, which results in dielectric losses. The nature of frequency and temperature dependence of AC conductivity suggests an electronic hopping mechanism, which is compatible with the highly disordered or amorphous structure of the grain boundary layers, having high densities of localized levels [47].

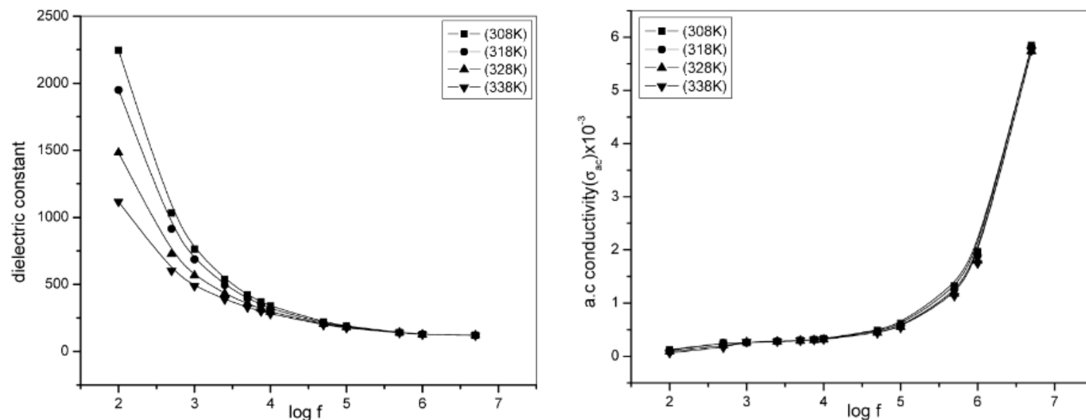

Figure 2.4: Variation of dielectric constant *(a)* and AC conductivity *(b)* as a function of the logarithm of the frequency for nano ZnS samples at different temperatures [47].

2.2 Applications in photovoltaics

Zinc sulfide (ZnS) has many opportunities for technological applications, e.g. opto-electronic devices such as blue light emitting diodes, electroluminescent devices and photovoltaic cells. Moreover, monocrystalline and polycrystalline ZnS thin films have received particular attention in recent years because of its possible important roles in the photovoltaic technology. One of the advantages of the ZnS films is that they can be easily prepared by several techniques, such as sputtering, molecular beam epitaxy, chemical vapor deposition, thermal evaporation, spray pyrolysis and chemical bath deposition [48].

Today the efficiency of solar cells is one of the most important features in the contest of renewable energy sources. In thin film solar cells, CdS has been the most common semiconductor material used as a buffer layer deposited on top of Cu absorbers. However, the use of Cd is associated to toxic hazards thus leading the attention to new materials having a less impact on the environment to be used as buffer layer. The ZnS is considered one of the most promising candidates among various alternative materials for its non-toxicity, abundance and cheapness [49]. In addition, ZnS has a direct wide energy gap of 3.5 – 3.9 eV at room temperature, which is larger compared to CdS which has an energy gap of 2.45 eV [49].

The efficiency of thin film heterojunctions solar cells strongly depends on the interfacial properties between absorber and buffer layers. The recombination of photo-excited electron-hole pairs that takes places at the surfaces and interfaces is still a limit from this point of view. ZnS thin films can act as excellent surface passivation layers because of their high transmittance, wide energy gap and insulating properties. Due to its low reflectivity, ZnS thin films could also find applications as antireflection coatings, which are essential part of the solar cells. Previous studies showed that the use of a ZnS buffer layer for a CZTSSe monograin solar cell results in similar functionality level as a CdS buffer layer [5]. In the experiment reported in reference [5], a higher transmission in the blue light region for the ZnS buffer compared to CdS has been observed. In addition, the substitution of the CdS buffer layer with ZnS, which is a higher energy gap material, has been observed to improve the quantum efficiency of CIGS thin film solar cells at short wavelengths leading to an efficiency of 13.3 % [6]. Furthermore, doped ZnS nanoparticles with dimensions below that of the Bohr diameter exhibit interesting opto-electronic properties due to quantum confinement effect and are potential candidates for a variety of applications among which the quantum dot solar cells [45].

Chapter 3
Materials and Methods

3.1 Materials

In this work, a sample set of zinc sulfide (ZnS) thin films has been analyzed by Atomic Force Microscopy techinque, which will be described in detail in the following section. In addition, two samples of a different zinc compound, zinc oxide (ZnO) thin films, have been studied in order to compare the properties of the two zinc compounds. ZnS layers are grown by Direct Current sputter deposition (DC Sputtering) using different sputtering power. Zinc sulfides are grown at the Department of Materials Sciences, University of Milano Bicocca, while zinc oxides are grown also by DC sputtering at the Physics Department, University of Konstanz.

Deposition by sputtering is a Physical Vapor Deposition (PVD) technique widely used in the thin film industry. Sputtering method involves the bombardment of a target, made of the material to be deposited, by positive ions which act to remove the material by colliding with its surface [50]. Ions are accelerated by gas discharge between two electrodes, where the negative electrode is bombarded by the positive ions generated in the plasma [51]. A sketch of a typical sputtering deposition system is shown in Figure 3.1. Sputtered atoms ejected this way can impact the substrate causing the layer to grow. A DC voltage applied in the presence of inert gas (usually Argon) kept at low pressure inside a vacuum chamber provides the discharge that originates the energetic ions [51]. The inert gas atoms become positively charged ions attracted to the negatively charged target material at a very high velocity that sputters off particles from the source. These particles cross the vacuum chamber and are deposited as a thin film of material on the surface of the substrate to be coated. Among the main advantages, sputtering deposition technique provides a reproducible deposition control, with the same deposition rate for same value of the parameters involved, meaning an easy film

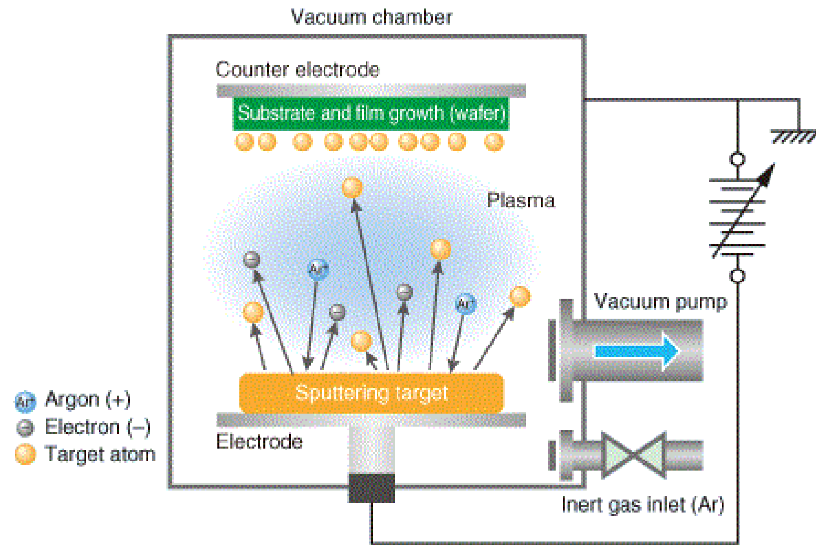

Figure 3.1: Schematic view of a sputter deposition device [52].

thickness control [53]. Another advantage is the absence of damage occurring from x-ray [53]. ZnS samples have been grown with different sputtering power. It will be shown in Chapter 4 that these different initial conditions will affect the morphology of the materials, yielding different surface parameters associated with that. ZnS samples have been grown through DC Sputtering using Argon as inert gas, on a 2 mm soda-lime glass substrate hold from fixed distance of 6 cm from the target. During the process a pressure of $6x10^{-3}$ mbar has been maintained for the Argon. The list of zinc sulfide samples investigated in this thesis is shown in Table 3.1.

Table 3.1: List of the ZnS samples with related thickness and sputtering power.

Sample name	Thickness (nm)	Sputtering Power (W)
35	75	50
36	75	75
60	75	125
53	75	150
93	75	75
94	75	75
95	170	75
97	370	75

where d represents the thickness of ZnS grown on the substrate and P the sputtering deposition power. Thickness of the ZnO layer is 900 nm for ZnO_96 and 1000 nm for ZnO_97, deposited on 2 mm of borofloat glass.

Characteristics of the ZnS thin films reported from previous studies made by the UniMIB Physics Department are reported in Figure 3.2. The average transmittance (measured in the wavelength range 400-800 nm in Figure 3.2 *(a)*) has a decreasing trend with increasing sputtering deposition power while the E_g value in dependence with power remains approximately constant around 3.2 eV, according to data from literature. The graph reported in Figure 3.2 *(b)* shows E_g as a function of the sputtering power holding a trend which is about a constant, although in the range 60 – 100 W it seems to assume the higher values. For the further results, it is important to note that the sample deposited with a 75 W sputtering power shows the greater transmittance in the higher wavelength range: 700 - 1000 nm (not on the graph).

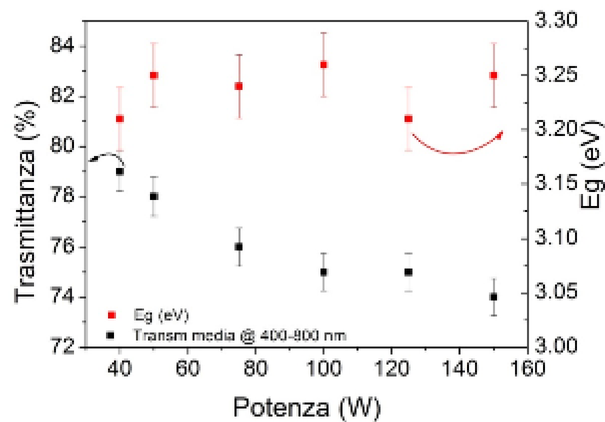

(a)

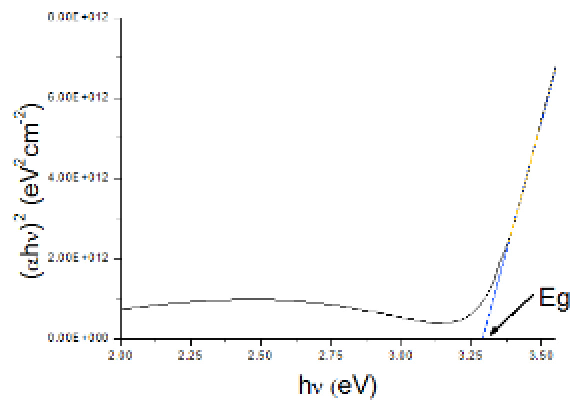

(b)

Figure 3.2: *(a)* Transmittance and energy gap vs deposition power for several ZnS samples; *(b)* Slope of $(\alpha h\nu)^2$ vs energy in order to get E_g from the intersection with the abscissa.

3.2 Methods

The experimental methods employed for the morphological and electrical characterization of the ZnS thin films have been reported in this section, including: a detailed description of the Atomic Force Microscopy (AFM) technique, the experimental instruments used in the measurements with a brief overview on their main components, the image processing with the statistical analysis performed, the dip analysis method, the electrical characterization by means Electrostatic Force Microscopy (EFM) and Kelvin Probe Force Microscopy (KPFM).

3.2.1 Atomic Force Microscopy

AFM analysis of the sample set have been carried out to obtain information on the morphological characteristics of the surfaces. This has been done obtaining several maps in different sizes (in the order of microns) and analyzing them with statistical methods. The main focus of the thesis is the morphological characterization of the ZnS thin films done by AFM measurements, in addition electrical analyses have been performed to prove that ZnS films totally act as insulators and a third step in which contact potential maps of the samples have been obtained by EFM and KPFM techniques.

The AFM is a type of Scanning Probe Microscopy (SPM), a branch of microscopy that forms images of surfaces using a physical probe that scan the specimen. It was invented by Binnig and co-workers in 1986, as a spin-off of its older sibling the Scanning Tunneling Microscope (STM) [54]. For single crystals the STM and AFM are capable of resolving surfaces with true atomic resolutions, as was shown in the case of the AFM for the first time in 1995 by Giessibl [55], resolving individual atoms on a single crystal Si(111)(7×7) surface under Ultra High Vacuum (UHV) conditions [56]. An AFM has several advantages over the Scanning Electron Microscope (SEM), which provides a two-dimensional image of a sample, being able to obtain three-dimensional surface profile. No special treatments are required for samples scanned by AFM that could lead to plastic deformation (damage) of the sample. Furthermore, where a SEM needs a vacuum environment to operate, an AFM can work perfectly without this expensive condition. However, some disadvantages place limits to the work of an AFM respect to a SEM: the scan area of an AFM is in the order of tens of microns while for a SEM it could easily reach square millimeters. Moreover, the scan speed of an AFM typically results extremely low.

As the name Atomic Force Microscopy implies, this technique utilizes forces arising from tip-sample surface interaction. The interaction occurs via the atoms of the sample surface and those of the tip-apex which probes the surface. For an atomic resolution imaging, it is of fundamental importance that the tip has a sharpness in the order of atomic size, which means having one atom or a cluster of atoms interacting with the surface. To obtain such a thin size super-sharp tips are used with the tip average radius typically lying on 10 nm. A flexible one-side-gripped cantilever free to oscillate in the

other side contain the tip, which is hold in the oscillating end of the cantilever. The tip-surface distance (typically about 0.1–10 nm) is decreased until the tip is in contact or, in the case of non-contact mode, very close to the sample surface. In the first case the deflections acting on the cantilever provide the signal from which a morphological map is constructed. In non-contact mode however, the cantilever is made to oscillate and the long and short force interactions with the surface, which have an attractive or repulsive influence on the tip and depend on the distance from the surface, cause the cantilever oscillation to change amplitude or frequency providing a signal proportional to the variation.

3.2.2 Experimental setup

In this work, two AFM instruments have been used in order to do combined measurements of samples: Solver P47H-Pro by NT-MDT and NX10 by Park. An image of the instruments used is shown in Figure 3.3 *(a)* and *(b)*, respectively. The AFM measurements have been controlled by the software NOVA for NT-MDT and XEP for Park.

Main components of an AFM include an AFM probe that scan the sample surface for the morphological characterization, a piezoelectric scanner which controls the tip-surface distance and moves the tip across the surface, an anti-vibration system which reduces external-environment mechanical vibrations, an optical system revealing the cantilever deflection and a digital control system which controls the raster scanning and the feedback unit. A schematic view of the main components of the AFM is shown in Figure 3.4.

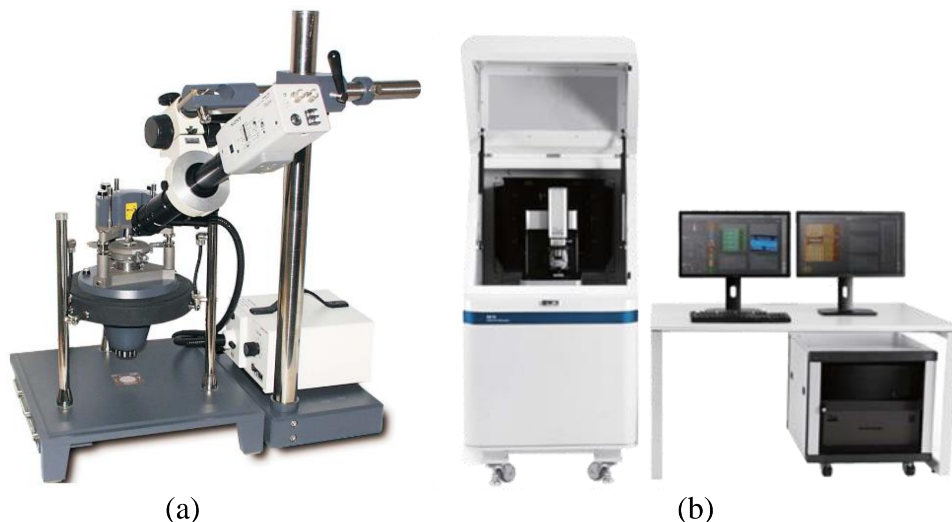

(a) (b)

Figure 3.3: The AFM instruments used in the analysis: *(a)* AFM NT-MDT; *(b)* AFM Park [57], [58].

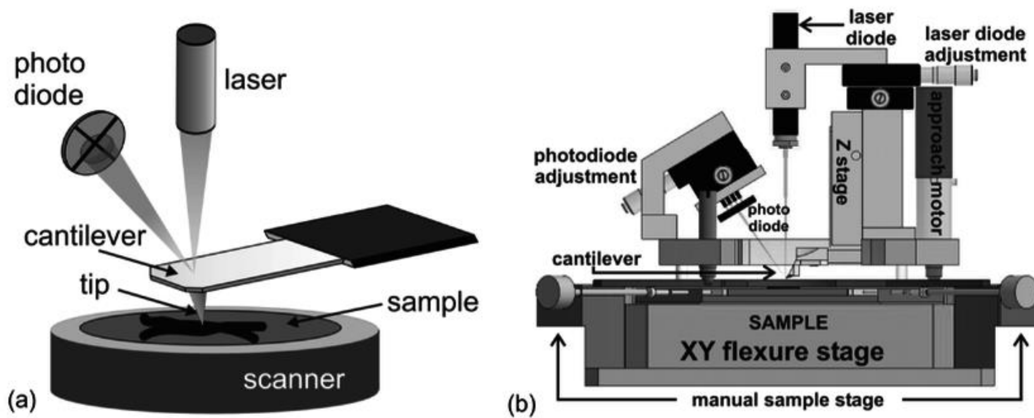

Figure 3.4: *(a)* Scheme of an AFM. A small nano-tip probes the sample surface. A light lever detection scheme is used to measure the deflection of the cantilever due to the surface topography; *(b)* AFM placed on top of an inverted optical microscope [59].

AFM Probes

Usually probes used in AFM are nanoscale elastic levers with a sharp apex on the free-oscillating end. The apex of the probe defines the resolution of the microscope, the sharper the probe the better the resolution. For atomic resolution imaging the probe must be terminated by a single atom. The probes are usually fabricated through photolithography, ionic implant and acid etching, usually from silicon nitride and silicon oxide deposited on a silicon wafer [60]. The rear of the levers is typically coated with a thin metal film made of aluminium or gold to increase reflectance but several types of interaction can be detected, depending on the interaction under investigation, the surface of the tip needs to be coated: making electrical measurements requires a thin conductive-material film coating (usually Cr, Au, Ti, Pt), while ferromagnetic coatings (as Fe, FeCr, Co, CoCr) are required for detecting magnetic properties of the surface [61]. The curvature radius of a tip-apex is in the order of nanometers (1 – 50 nm). AFM probes are often replaced when the tip-apex becomes dull or when the cantilever has been damaged, which happens relatively often during analyses. The interaction force acting on the probe can be estimated from the Hooke's law, where k is the elastic constant related to the cantilever, varying with material and geometry, in the range of 10^{-3} - 10 N/m, and the shift is that of the tip due to the cantilever deflection. The softer the lever (smaller k), the better for sensing the deflection, but this requires smaller mass to keep the high frequency, which usually lie from tens to thousands kHz. Among the cantilever properties there must be included: length l, cross section S, density ρ and Young's modulus E, related to the resonance frequency of oscillation by [62]:

$$\omega_{res} = \frac{\lambda}{l^2}\sqrt{\frac{EJ}{\rho S}} \tag{3.1}$$

where λ is a numerical coefficient depending on the oscillation mode of the cantilever.

The "quality-factor" (*Q-value*) of the oscillations, characterizing the resonator's bandwith relative to its center frequency, is another important (*dimensionless*) parameter and depends on the medium in which the cantilever oscillates: higher Q indicates a lower rate of energy loss relative to the resonator energy, that is oscillations dying out more slowly. Typical values of Q in UHV lie around 100 [62].

In this work two types of AFM probes have been used, listed in Table 3.2. The tip radius is one of the most important parameters for obtaining high resolution images, as tip-sample convolution effect is always present in AFM micrographs. Very sharp probes, with radius of the order of 2 – 5 nm, can be used to reduce this artifact (see e.g. SSS-NCHR in Table 3.2). In Figure 3.5 the AFM probe tips used for the morphological characterization of the samples are shown.

Table 3.2: Main features of the AFM probes used for morphological characterization of ZnS. Measurements have been done in semi-contact mode with NT-MDT and in non-contact mode with Park.

Probe (AFM)	NSG10 (NT-MDT)	SSS-NCHR (Park)
Radius (nm)	10	5
Length (μm)	95	125
Width (μm)	30	30
Resonant frequency (kHz)	240	330
Elastic constant (N/m)	11.5	42

Anti-vibration system

To reduce the influence of external mechanical oscillations on the measurement process an anti-vibration system is employed. Mechanical vibrations originating from the external environment can excite the resonance frequency ω_{res} of the tip-sample system, causing fluctuations on the tip-sample distance, observables as periodic noise in the resulting sample AFM image [62]. To reduce the external vibrations effect, active (used in AFM Park) and passive (used in AFM NT-MDT) anti-vibration systems are developed. Active anti-vibration systems include a vibration sensor with an actuator which stabilizes through a feedback the platform. The sensor generate a signal sent to the feedback, where is amplified and re-sent to the piezo-actuators, reducing the platform acceleration [62]. Passive anti-vibration systems are based on the following principle: external oscillations amplitude rapidly vanishes at frequencies far from the resonance frequency of the medium in which the oscillations act. Hence, placing the

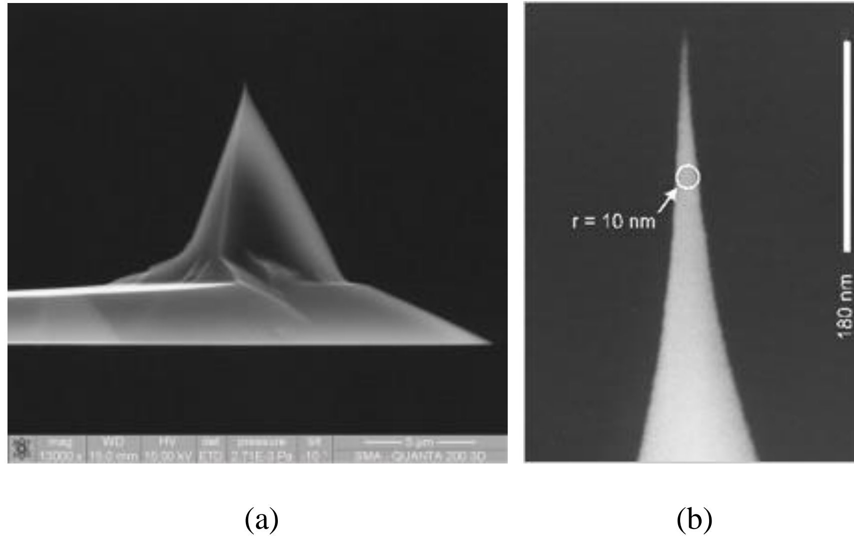

(a) (b)

Figure 3.5: AFM probe tips used for the morphological characterization. *(a)* NSG10 tip (used in NTMDT); *(b)* SSS-NCHR tip (used in Park) [63], [64].

tip-sample mechanical system onto an elastic platform with a very low resonance frequency, the platform acts as filter for the external high-frequencies vibrations, with the result of have an efficient anti-vibration system [62]. To obtain a very low resonance frequency anti-vibration system (less than 1 Hz), it requires a compression length of the elastic medium bigger than 20 cm [62]. This is achieved for AFM NT-MDT using three elastic cables which acts definitely as passive anti-vibration system.

AFM Scanner

To control the tip-sample distance with great accuracy a piezoelectric transducer (*scanner*) is employed. The scanner working-principle is based on the piezoelectric materials property of changing their geometric dimensions when undergoing to an electric field. The piezo-scanner is constituted of a single tubular element with the arrangement depicted in Figure 3.6. There is a single internal electrode while the external one is split in four different sectors. When applying a potential difference between two opposite sectors of the external electrode, the tube shortens in the case of the electric field and polarization having the same direction, or lengthens in the case of field and polarization having opposite directions. This make bend the tube resulting in a two-dimensional scan of the sample surface, while acting on the internal electrode potential is possible to shorten or lengthen the tube on the z axis. A piezoelectric tubular scanner like the one shown in Figure 3.6 is used by the AFM NT-MDT, while the AFM Park scanner is decoupled on the xy and z stages, resulting in a lower image distortion. Non-desirable effect can arise when treating piezoelectric materials. Deformations are never exactly proportional to the applied electric field, in fact at a certain field values

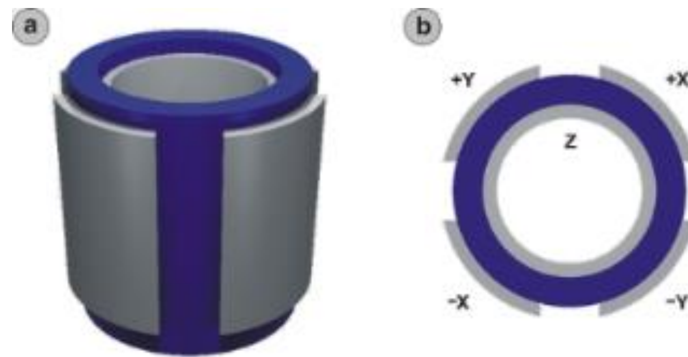

Figure 3.6: Schematic illustration of a piezoelectric AFM tubular scanner viewed from ahead *(a),* and on top *(b).* The blue tube is made of piezoelectric material, while the grey plates represent the external and internal electrodes to which a voltage is applied in order to control the tube's deformation in horizontal and vertical directions.

(over 100 V/mm) the linearity regime is lost [62], this is avoided by applying a restrained electric field. Another effect is the so-called *creep* phenomenon, it consists in a delay of response when suddenly changing the potential difference applied, causing image distortion. This is in some part removed including controlled-delays in the control system. Piezo scanners exhibit more sensitivity at the end than at the beginning of a scan, this causes the forward and reverse scans to behave differently and display an *hysteresis* effect between the two scan directions, in which the piezo-deformation depends on the potential difference applied at an instant before. To remove image distortion originated from this phenomenon, signals are stored only in a monotone way during the scan.

Optical system

To detect the cantilever deflections, both AFM employ a beam-bounce technique. It consists in a laser beam emitted from a source and focalized on the lever so that the reflected beam hits the center of the optical system which acquires the signal. In this way, attractive or repulsive forces acting on the cantilever are measured by the optical device composed by a four-sectors photodiode, allowing the measurement of the vertical and lateral component of the force associated with the tip-sample interaction. Considering I_n^0 (with n = 1,2,3,4) the reference values of the four photocurrents associated with the respective photodiodes, and I_n^{def} the same values when the cantilever is deflected, the interaction between the tip and the sample surface will be proportional to the shift intensity and direction of the cantilever detected in terms of photocurrent difference:

$$\Delta I = I_n^{def} - I_n^0 \tag{3.2}$$

where the difference proportional to the deflection due to the normal component of the force F_z is:

$$\Delta I_z = (\Delta I_1 + \Delta I_2) - (\Delta I_3 + \Delta I_4) \quad (3.3)$$

and that proportional to the lateral component of the force F_{xy}:

$$\Delta I_{xy} = (\Delta I_1 + \Delta I_4) - (\Delta I_2 + \Delta I_3) \quad (3.4)$$

Hence, the photocurrent difference ΔI_z is the main signal introduced in the feedback system of the AFM, which acts on the piezo-scanner to hold the value constant by varying the tip-sample distance to maintain the deflection Δz equal to the reference value before the scanning operations [62]. A schematic view of the optical device is shown in Figure 3.7.

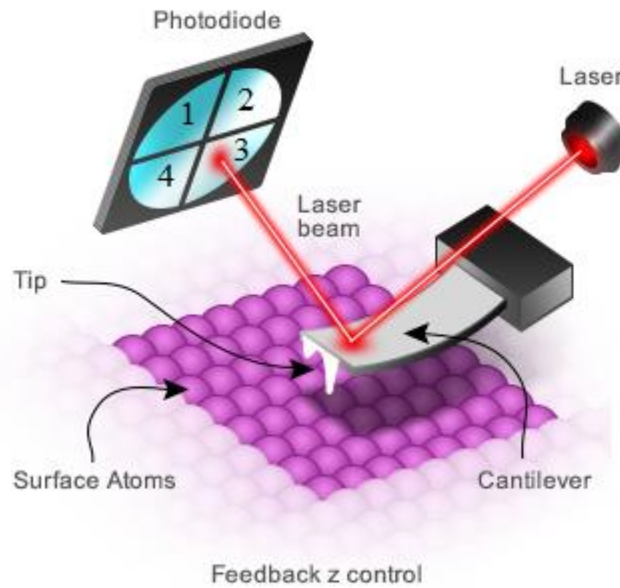

Figure 3.7: Schematic view of the four-sector photodiode optical device for the cantilever deflection measurement [65].

3.2.3 AFM modes of operation

In general, AFM measurements can be performed in three different modes: contact, non-contact and semi-contact (*tapping*) mode topography. In this thesis all the AFM measurements on ZnS have been done in semi-contact mode with AFM NT-MDT and in non-contact mode with AFM Park. The main differences and the basic features of the procedure used are described in the following section.

The main general disadvantage of contact mode is the direct mechanical interaction between the tip and the sample that usually lead to a permanent damage of the tip and, more important, of the sample surface. This is the main reason why contact mode has not been employed in this work. In contact mode a direct contact between the tip and the surface is established and the repulsive force acting between the tip-apex atoms and the sample surface ones is balanced by the elastic force originated from the cantilever deflection. For this reasons the elastic constant of cantilevers used in contact mode are relatively small compared to those used in non-contact, in fact a higher sensibility means a lower risk of an exaggerated tip-sample interaction. It was realized relatively early that force of magnitude such as that existing between single atoms lead to a high risk of irreversible damage ruining either the surface structure or the atomic sharpness of the tip making it blunt [56]. A blunt tip has more tip-apex atoms interacting with the surface, resulting in an apparent atomically resolved image of the sample surface but making the atomic defects invisible at all, as schematically depicted in Figure 3.8. Contact mode can be performed by maintaining either a constant force or a constant average tip-sample distance. During a constant force scan, the feedback system maintains a constant deflection of the cantilever, which reflects a particular interaction force, by applying a potential difference to the *z*-axis electrode of the piezo-scanner proportional to the topographic height in each point of the surface. In constant average distance mode there is no feedback acting on the scanner and the height trace of the AFM image is obtained as a signal proportional to the deflection of the cantilever measured by the optical system. This is however only applicable on samples with a very small roughness, which makes this mode of operation the less preferred of the two.

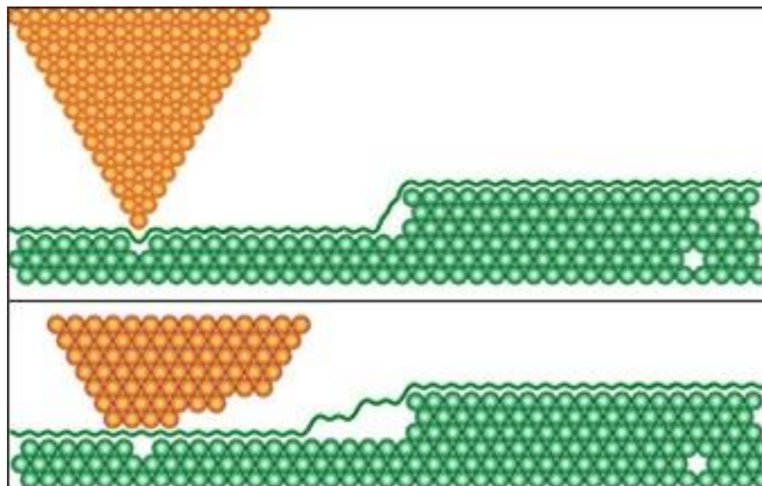

Figure 3.8: Schematic view of contact AFM imaging: *(up)* the intact tip maps perfectly the atomic structure of the surface; *(down)* the trace of the blunt tip fail to detect the point defect in the surface [66].

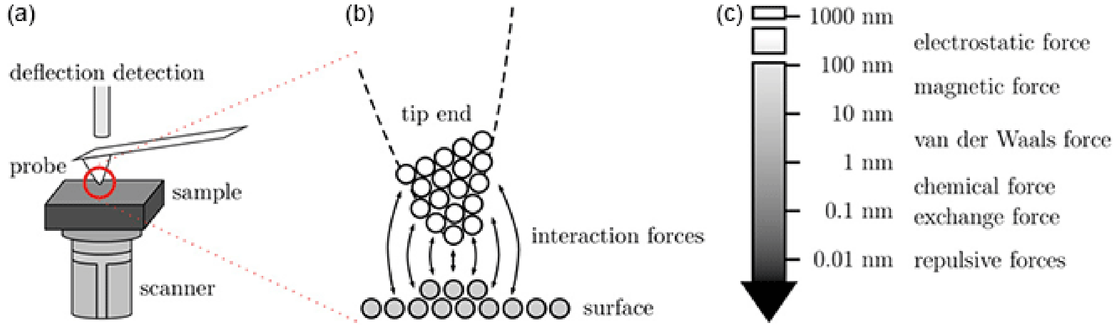

Figure 3.9: Schematic model of non-contact AFM mode. *(a)* Tip-cantilever-sample system from a macroscopic view; *(b)* Zoom illustrates the long ranged interaction of several tip and surface atoms, while the short ranged interaction principally only exists between the tip-apex atom and the surface atom directly below; *(c)* By approaching the surface from a certain height in the z-axis various distance dependent electromagnetic long and short ranged interatomic forces are detected [67].

Non-contact mode has been used in AFM Park measurements of ZnS. In this mode of operation, the cantilever oscillates at or near by its resonance frequency close to the sample surface but separated from a safe distance, which means that the minimum tip-sample distance achievable is such that no permanent damage can be done to either the tip or the sample, therefore the tip-cantilever system scans the surface in a dynamic mode, contrary to contact AFM. A schematic illustration of non-contact AFM mode is shown in Figure 3.9. Any tip-sample interaction influences amplitude, frequency or phase of the cantilever. During non-contact mode, signal associated with height and phase topography is acquired from these variations of the amplitude or frequency (or phase) of the cantilever oscillation, which are detected by the optical system. Main features of an oscillating-lever-surface interaction can be described by a classical mechanic model of the z-axis motion of the cantilever, considering the tip mass as a point-like mass on the free end of an oscillating lever with an elastic constant k_{cant} and treating the tip-cantilever system as an effective mass m_{eff} , through the following equations [56]:

$$m_{eff}\ddot{z} = F_{dr}\cos(\omega_{dr}t) - k_{cant}z - \gamma m_{eff}\dot{z} + F_{ts}$$

(3.5)

$$k_{cant} = \frac{Ewt^3}{4L^3}$$

where F_{dr}, ω_{dr}, k_{cant} and γ are the magnitude and frequency of the excitation force driving the oscillation, the cantilever spring constant and the oscillation damping, respectively, and E, w, t, L are Young's modulus, width, thickness, length of the cantilever. F_{ts} is a force term which includes all the interaction forces between the tip and the surface, meaning the total tip-surface force. However, an exact expression for F_{ts} requires a detailed knowledge of all interacting atoms resulting quite complex to

model exactly. Neglecting the total tip-surface force term F_{ts}, Eq. (3.5) has the followings solutions for the tip motion [56]:

$$z(t) = A\cos(\omega_{dr} + \varphi)$$

$$A = \frac{F_{dr}}{m_{eff}} \frac{1}{\sqrt{(\omega_0^2 - \omega_{dr}^2)^2 + \left(\frac{\omega_{dr}\omega_0}{Q}\right)^2}} \tag{3.6}$$

$$\varphi = \arctan\left(\frac{\gamma\omega_{dr}}{\omega_{dr}^2 - \omega_0^2}\right), \quad \omega_0 = \sqrt{\frac{k_{cant}}{m_{eff}}}, \quad Q = \frac{\omega_0}{\gamma}$$

where A, φ, ω_0 and Q are the oscillation amplitude and phase, the mechanical resonance frequency of the free oscillating tip-cantilever system and the quality factor (Q-value) of the oscillation, respectively. Eq. (3.6) describes a forced damped harmonic oscillator, however system including F_{ts} into the equation of motion of the tip-cantilever requires to make the so called small amplitude approximation.

For small oscillations around the z_0 distance from the surface, the total tip-surface force term F_{ts} can be approximated with a series expansion truncated at the second term [56]:

$$m_{eff}\ddot{z} = F_{dr}\cos(\omega_{dr}t) - k_{cant}z - \gamma m_{eff}\dot{z} + z\left.\frac{dF_{ts}}{dz}\right|_{z=z_0}$$

$$m_{eff}\ddot{z} = F_{dr}\cos(\omega_{dr}t) - k_{eff}z - \gamma m_{eff}\dot{z} \tag{3.7}$$

$$\text{with} \quad k_{eff} = k_{cant} - k_{ts}$$

where the first order derivative of F_{ts} is a variation from the "effective" elastic constant k_{eff}, included as an additional term k_{ts}, as shown in Eq. (3.7). The main consequence is that the only difference from the equation of motion described by Eq. (3.5) is that the resonance frequency changes, in fact Eq. (3.7) still describes the motion of a forced damped harmonic oscillator.

The new resonance frequency can therefore be expressed as follows:

$$\omega_{res} = \sqrt{\frac{k_{eff}}{m_{eff}}} = \omega_0 - \frac{\omega_0 k_{ts}}{2k_{cant}}$$
$$f_{res} = f_0 + \Delta f\,, \qquad \Delta f = \frac{f_0 k_{ts}}{2k_{cant}} \tag{3.11}$$

As a result, the resonance frequency of the cantilever will decrease if the tip-surface interaction corresponds to a positive force gradient k_{ts}, while increasing in the case of a negative force gradient. From Eq. (3.11) it is clear that probing in the attractive regime will result in a positive frequency shift Δf, while in the repulsive regime will result in a negative one. The total force and its gradient are plotted in Figure 3.10. The tip-surface separation distance dependence of the force gradient k_{ts} and thus of the resonance frequency is the main link used to obtain a topographic map of the surface under investigation by detecting the mechanical resonance frequency changes of an oscillating tip-cantilever which is very close to the sample surface. The two most common modes of non-contact AFM operation, frequency modulation (FM) and amplitude modulation (AM), are described below.

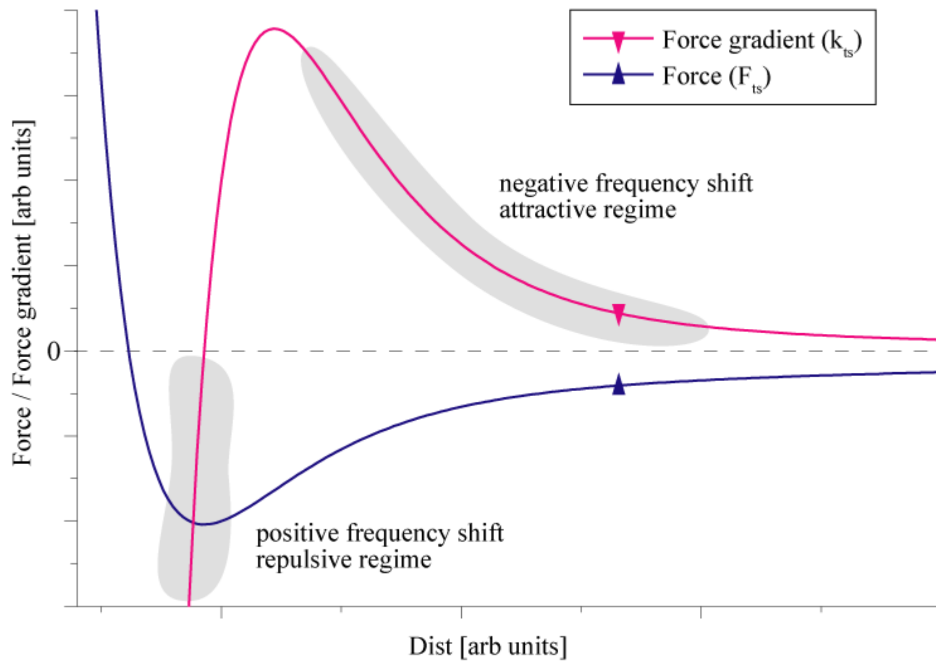

Figure 3.10: A plot of the total tip-surface interaction force (F_{ts}) and force gradient (k_{ts}). Shaded regions are available for probing with a positive or negative resulting frequency shift [56].

In frequency modulation mode, which was first introduced by Albrecht *et al.* in 1991 [68], the cantilever oscillates separated from the surface with a constant amplitude maintained by the feedback system [69]. The signal used to generate the image is obtained by the detection of changes in the resonant frequency of the cantilever [70]. The difference between the actual resonant frequency, which depends on the tip-surface forces, and that of the free lever can be measured to find the frequency shift associated to the tip-surface separation distance [71]. Then the frequency shift can be recorded as function of position during the scan to generate a topographic image of the sample surface.

In amplitude modulation mode, which was first introduced by Binnig and Quate in their seminal 1986 AFM paper [72], the cantilever is excited over its resonant frequency making possible to detect forces that change the resonant frequency by detecting the amplitude of oscillation, as shown in Figure 3.11. When the tip approaches the sample surface, the force gradient causes a change in both the amplitude and the phase of the cantilever. These changes are used to produce the signal that generate the image. The AFM control system then uses amplitude as the reference channel, either in feedback mode, or it can be recorded directly in constant height mode. When the tip-cantilever system is driven exactly at its resonance frequency, the resulting oscillation amplitude reaches a maximum. If the driving frequency is shifted from resonance, either higher or lower, the oscillation amplitude will decrease [56]. Amplitude modulation can fail if a sudden change to a more repulsive (less attractive) force can shift the resonance over the drive frequency causing it to decrease. In constant height mode this will only lead to an image artefact, but in feedback mode the feedback will read this as a stronger attractive force, causing positive feedback until the feedback saturates.

In the semi-contact or tapping mode, which has been used in AFM NT-MDT measurements, the cantilever oscillations are excited near the resonance frequency with a high amplitude usually varying from several nm to 200 nm [56]. The cantilever in close proximity with the surface during the lower semi-oscillation get in contact with the sample surface, meaning in the repulsive force region.

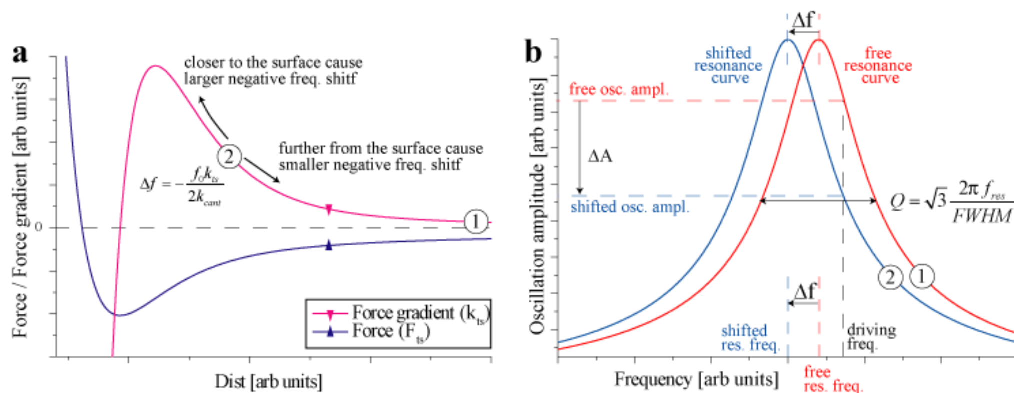

Figure 3.11: Plots showing the basic principles of amplitude modulation AFM. *(a)* Force and force gradient between the tip and the surface; *(b)* Resonance frequency for the free oscillating cantilever (red) and resonance frequency shifted cantilever (blue), relating to distances (1) and (2) in *(a)*. The resulting decrease in oscillation amplitude (ΔA) due to the force gradient induced frequency shift (Δf) is shown [56].

The Van der Waal's forces, dipole-dipole interactions and electrostatic forces cause the amplitude of the cantilever's oscillation to change as the tip gets closer to the sample [56]. The amplitude is the parameter used by the feedback system to maintain a set cantilever oscillation amplitude adjusting the height above the sample. A tapping AFM image is therefore obtained by mapping the force of the intermittent contacts of the tip with the sample surface, storing the potential difference signals provided by the feedback system to the z-axis electrode of the scanner [62]. At the same time, the phase shift variations are stored as a "phase contrast" image, which can give rise to regions of varying stiffness or with different adhesion properties that are not visible in the topographic image. Although the peak forces applied during the contacting part of the oscillation can be much higher than typically used in contact mode, tapping mode generally decreases the damage done to the surface and the tip compared to the amount done in contact mode [62].

3.2.4 Image processing

To obtain clear AFM images it is of primary importance to set the correct values of the main AFM parameters during the measurement. First of all, the set point (the measure of the force applied by the tip to the sample) must be adjusted to reach the optimal value for each scan. Too high values lead to minor interaction between the tip and the sample, with the possibility of lose it completely. However, a too low set point provides a large force, which often means better imaging, but also more wear on the tip and the sample, i.e. lower tip life and less chance of getting a complete sample without the tip getting contaminated or broken [73].

In this thesis, each AFM measurement has been started with a high value of the set point to avoid fast tip degradation. The set point has been subsequently lowered until the value for the best tip-sample interaction was reached, depending on the attractive or repulsive regime. In the analyses performed, both attractive and repulsive regimes have been used to obtain the better image quality. Other parameters have been chosen to improve the measurements: the amplitude of oscillations, the amplitude gain and the scan rate, which is of particular interest since AFM measurements usually take a long time to perform, this is the reason for a high scan rate is often preferred. However, this could result in an image distortion along the scan direction due to an exaggerated scan speed. During the scan, the phase of oscillations is another important parameter to check continuously, since its value reflect in what interaction regime the scanning is going through, that is attractive or repulsive. Standing in a halfway-regime, meaning a phase around 90° (so called *instable phase*), could lead to artifacts which compromise the clearness of the image. Measurement done in this work has been taken in either attractive or repulsive regime, depending on the better quality result.

Once the AFM measurements have been done, a series of corrections have been applied to the maps in order to remove distortions and artifacts originated from several causes. Main artifacts that may occur are divided in three types

- Tip effects, meaning the various artifacts that can occur due to the interaction of the tip with the sample;
- Scanner artifacts, effects due to the peculiarities of the piezoelectric scanner;
- Other artifacts;

Tip effects include the general tip-sample convolution, or a contaminated tip which introduces strange shapes into the image, and the case of a blunt tip which reduce image quality, as was shown in Section 3.2.3. Among scanner artifacts the piezo-creep and the edge overshoot must be included, the first described in Section 3.2.2 and the second occurring when the scanner moves further than it should vertically, with the result of an exaggerated sharpness of the image features [73]. Other artifacts include sample thermal drift movement which cause distortions and artifacts (see Figure 3.12 and 3.13) due to problems with the feedback. In the following part of this section, the main methods that have been used in order to get the best quality morphological images for ZnS, that will be shown in Chapter 4, are described in detail.

AFM measurements lead usually to not leveled data. This is due to a non-perfectly flat sample surface or to a sample which has been assembled with an inclination. A very inclined image occupies a great portion of the z-axis, with the result of a small contrast for the smaller details in the map. The choice of levelling method is based on the AFM configuration. For systems with tubular scanner moving in all three axes a plane leveling must be performed [74]. In the image processing made for ZnS, a series of tools from the software Gwyddion have been used. Plane leveling is typically the first function applied to raw AFM data. With this tool the plane is computed from all the image points and is subtracted from the data [74]. The matrix of values associated with the map obtained has a very lower portion of values occupying the z-axis, which allow to detect the smallest details, increasing the image contrast. An example of the filtering process which has been applied to ZnS_35 is shown in Figure 3.14 and Figure 3.15.

A line averaging by matching height median filter has been applied to all the measurements presented in this work. Micro-shifts in parts of the probe-head or micro-particles captured by the tip-apex could lead to fluctuations in the tip-sample distance during a scan, resulting in a step-effect in the lines parallel to the scan direction. This filter shifts the lines so that the differences of medians (between vertical neighbor pixels) becomes zero, preserving better large features [74]. Another very common scanning error is the local fault of the closed loop. As a result, scars or stripes are parts of the corrupted image, looking similar to line defects usually parallel to the scan direction. A filter that removes scars filter has been applied to all measurements, which finds and removes scars using neighborhood lines to fill in the gaps [74]. An example of line averaging application is shown in Figure 3.14 and Figure 3.15.

Moreover, one of the most important error sources in AFM measurements is the tip convolution artefact, which is shown in Figure 3.13. Since the AFM tip is never a delta-like function, meaning ideal, is often observed a certain degree of image distortion due to this effect and usually AFM tips are also imaged on the surface scan [74]. The AFM image is always a convolution between the tip geometry and that of the sample surface structure. If the precise form of the tip is known, then an AFM image can be partially reconstructed by a numerical deconvolution algorithm which uses an image of the tip obtained scanning structures with a known topography.

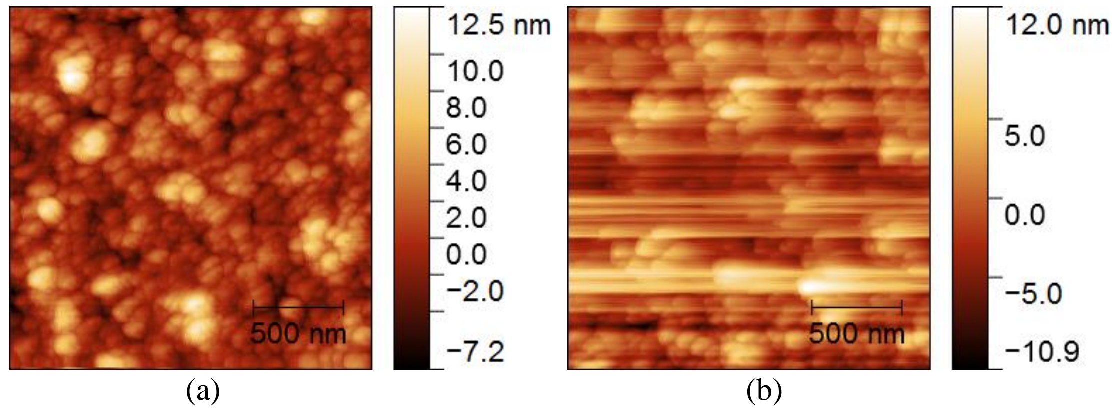

Figure 3.12: An example of thermal drift effect on ZnS_95: (*a*) An image obtained without with correct parameters after waiting the system to stabilize; (*b*) Another image of the same topography where the thermal drift effect is present.

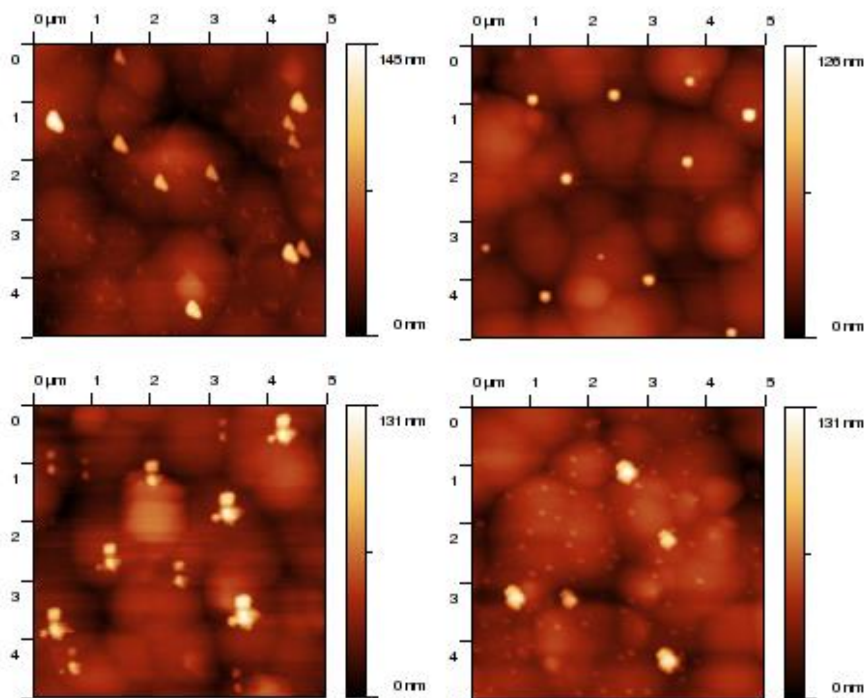

Figure 3.13: Tip convolution effect example images: various AFM probes are viewed as artifacts on the images due to the multiple contact points of a “bad” tip with the sample which produces a repetition of topographic features [74].

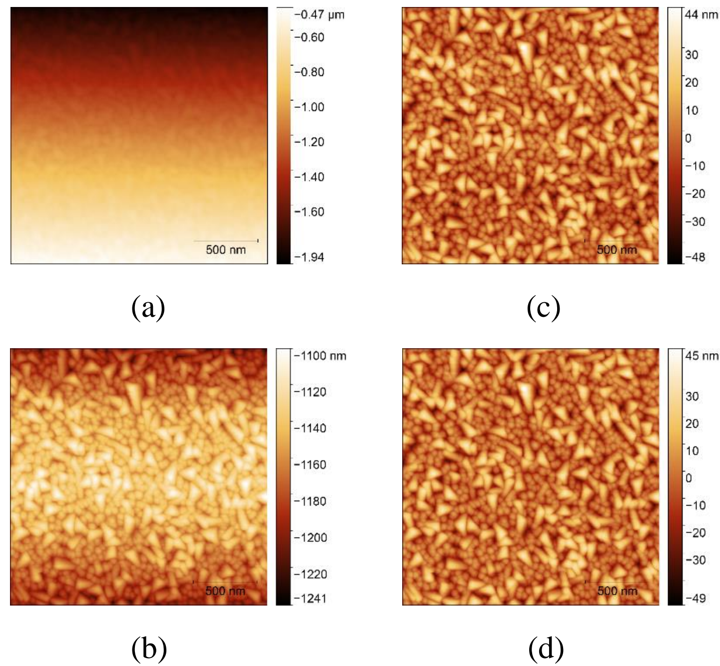

Figure 3.14: Image processing, application of various filters on ZnO_96: *(a)* original map; *(b)* plane level applied; *(c)* 2nd order polynomial background subtraction applied; *(d)* line averaging applied.

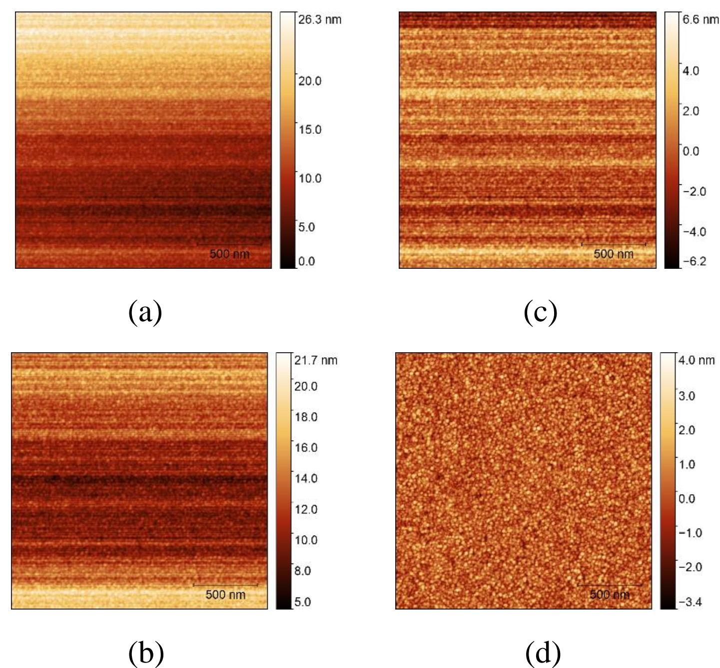

Figure 3.15: Image processing, application of various filters on ZnS_36: *(a)* original map; *(b)* plane level applied; *(c)* 2nd order polynomial background subtraction applied; *(d)* line averaging applied.

3.2.5 Image analysis

Once the samples have been scanned providing a number of topography maps, the next step of the work, the image analysis, has been done. The analysis done in this thesis consists in large part in measurement of the surface parameters associated with the morphology of the ZnS, meaning surface roughness, mean grains number and size. Values have been calculated with different methods: firstly, a general statistical evaluation of the main parameters (roughness, mean grains number and size) has been made using the software Gwyddion 2.40, and then the same parameters have been calculated from the theoretical approach described in detail in the following section using the computation software OriginPro 8.5. Dips measurement and the *I-V* characteristic are separated parts of the analysis, described in detail in the following section.

AFM data are usually represented as a two-dimensional data matrix of size *NxM*, where *N* and *M* are the number of rows and columns of the data field, respectively [74]. Assuming that is possible to describe the surface height at a given point (x,y) by a random function $\xi(x,y)$ that has given statistical properties, numerical characteristics of each row or column can be evaluated as functions of (x,y). In this way, an average value with its error is directly calculated by the software [74]. As a result, a statistical parameter has been evaluated: the Root Mean Square Roughness (R_{RMS}), which is the standard deviation of the height distribution, defined as follows [74]:

$$R_{RMS} = \sqrt{\frac{1}{N}\sum_{i=1}^{N}(z_i - \bar{z})^2} \tag{3.12}$$

where z_i is the value of the *i-th* point and $\bar{z}$ is the mean value over the evaluation length and N is the number of pixels on a row/column. Moreover, extrapolating the distribution of R_{RMS} is possible to calculate the standard deviation by rows or columns, that is averaging all values over the whole map, to obtain the average roughness R^* that avoids noise effects in the scanning line. However, since these calculations belong to the first-order statistical quantities describing only the statistical properties of the individual points, for a complete morphological description of the samples a higher order function has been considered. This function is the Height-Height Correlation Function (*HHCF*), which is provided by Gwyddion software and it is useful to obtain the surface parameters. *HHCF* is defined as follows [74]:

$$HHCF(r) = \frac{1}{N(M-m)}\sum_{l=1}^{n}\sum_{n=1}^{M-m}\left(z_{n+m,l} - z_{n,l}\right)^2 \quad \text{with} \quad m = \frac{r}{\Delta x} \tag{3.13}$$

where N and M are the number of rows and columns of the data field, z is the height associated at every point of the matrix and m is related to the sampling interval Δx (i.e. the distance between two adjacent points) of the AFM measurement, as in Eq. (3.13), in

which *r* is the lateral separation of two surface heights [75]. For AFM measurements, the one-dimensional *HHCF* is evaluated, based only on profiles along the fast scanning axis, assuming the surface to be *self-affine*. This results in a simpler form for the *HHCF* that is an approximation consisting of an exponential function, which has been used to fit the *HHCF* data extrapolated by Gwyddion. The general characteristics of a self-affine surface can be described by the following model.

For a surface profile *h(x)* with $r \ll \xi$ it follows the relation [75]:

$$[h(x+r) - h(x)] \sim (mr)^{\alpha} \tag{3.14}$$

where the left side term represents the surface roughness, α is the roughness exponent (the Hurst exponent) and *m* denotes the local slope of the surface profile. Remaining in the one-dimensional case, the following equation also holds [75]:

$$[h(\varepsilon x+\varepsilon r) - h(\varepsilon x)] \sim (\varepsilon mr)^{\alpha} \tag{3.15}$$

that can be rearranged to obtain:

$$[\varepsilon^{-\alpha} h(\varepsilon x+\varepsilon r) - \varepsilon^{-\alpha} h(\varepsilon x)] \sim (mr)^{\alpha} \tag{3.16}$$

which compared to Eq. (3.14), yields to the following relation:

$$[h(x)] \sim \varepsilon^{-\alpha} h(\varepsilon x) \tag{3.17}$$

A surface profile for which Eq. (3.17) holds is said to be self-affine [75]. In this case α represents the local roughness of the self-affine surface, where larger values of α ($\alpha \approx 1$) correspond to a greater roughness, while smaller values ($\alpha \approx 0$) correspond to a lower roughness [75]. An exemplificative illustration of surfaces with different α is shown in Figure 3.16.

For a self-affine surface profile, for which Eq. (3.17) holds, the *HHCF* data can be fitted by the exponential function given by the following equation:

$$HHCF(r) = 2{R_{HHCF}}^{2}\left[1 - exp\left[\left(-\frac{r}{\xi}\right)^{2\alpha}\right]\right] \tag{3.18}$$

where σ denotes the root mean square deviation of the heights, meaning the *HHCF* evaluated surface roughness R_{HHCF} and ξ denotes the autocorrelation length (or lateral correlation length) [74]. The lateral correlation length ξ is defined as the maximum lateral separation that two points of the surface can have to be considered correlated.

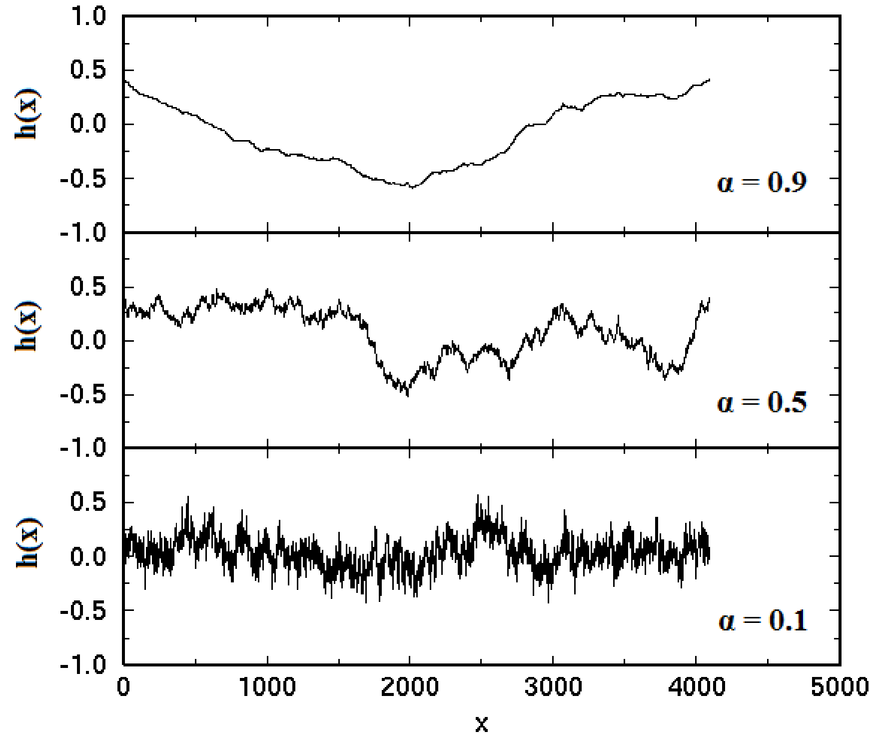

Figure 3.16: Three surface profiles showing different values for the Hurst exponent. From the profiles is visible that the larger is the value of α the smoother is the associated morphology, while a near zero value of α means a very rough surface profile [76].

For the ZnS films, 2μm x 2μm maps have been acquired to perform the statistical analysis described above. Values of surface roughness evaluated from HHCF analysis (R_{HHCF}) have been compared with root mean square roughness (R_{RMS}) provided by Gwyddion and with the rows/columns statistic average roughness (R^*). The results and their comparisons will be shown and discussed in Chapter 4.

Other important parameters, such as the mean grain density and average equivalent disc radius of the grains, have been extrapolated from the image segmentation tool developed by the software Gwyddion. Image segmentation method includes two stages of the grain analysis [74].

At first, a grain location is performed placing a virtual water drop at each point of the inverted surface. In this way the local minima of the surface are filled. After repeating the process several times, the positions of the grains for segmentation in the next step are identified by the larger lakes that have been formed. Secondly, the segmentation process is applied. This involves the marking of grains that have been found in the first step with different numbers. As the virtual water drops continue to be placed on the inverted surface filling the local minima, the possible results are [74]:

1. The drop fills the lake that has been previously marked as a grain. In this case the drop is marked as a part of the same grain.

2. The drop fills a place without the presence of grains. In this case, if in the nearest neighborhood another grain is present, the drop is marked as a part of

the same grain. However, if no grains are present close to the drop, it is not marked at all. Moreover, in the case of more than one grain lying in the nearest neighborhood of the drop, it is marked as a grain boundary.

3. The drop fills a place marked as grain boundary. In this case the drop also is marked as grain boundary.

By default, the segmentation algorithm marks valleys, therefore to mark upward grains the height has been inverted in the process. Before the evaluation of the main surface parameters (grain positions, sizes and number) by the segmentation method, a two-pixels threshold filter has been applied on each map in order to remove grains one-pixel wide under the assumption that they have been formed in the local minima originated by noise. With the application of this filter it is possible to evaluate correctly the grain number for each map without the contribution of false one-pixel grains incorrectly identified, which otherwise would have overestimated the total grain number and underestimated the mean grain size. Segmentation method involves the choice of several parameters, meaning that it is fundamental to set the optimal values of these parameters in order to get a mask perfectly matching with the grains boundaries. Incorrect grain segmentation could occur during the process (e.g. an individual grain can be split in several ones, grains could merge in a single one, one-pixel grains) and lead to over/under estimation of grain number and size.

The preprocessing segmentation has the following parameters, which vary in the range 0 – 100 %, except Gaussian smoothing that varies between 0 - 20 [74]:

- Gaussian smoothing: a Gaussian blur filter is applied to the data to reduce image noise and reduce detail, where applying a zero value means no smoothing.
- Add gradient: variations of the local gradient of the data originate grain boundaries in the regions associated with a high local slope.
- Add curvature: variations of the local gradient of the data originate grain boundaries in the regions locally concave.
- Barrier level: applies a height level above which pixels are not assigned to any grain.
- Prefill level: applies a height level up to which the surface is prefilled. Details at the bottom are removed.
- Prefill from minima: acts as the prefill level but the surface is prefilled from the local minima. Details at the bottom are removed.

Figure 3.17 shows exemplificative images of the image segmentation process, in which the segmentation parameters have been varied to show the different results. Grain results have been obtained using the grain-statistics Gwyddion tool which calculates the total number of marked grains, their total projected area, total length of grain boundaries and the mean area and equivalent disc radius of one single grain. The results of these calculations will be shown in Chapter 4.

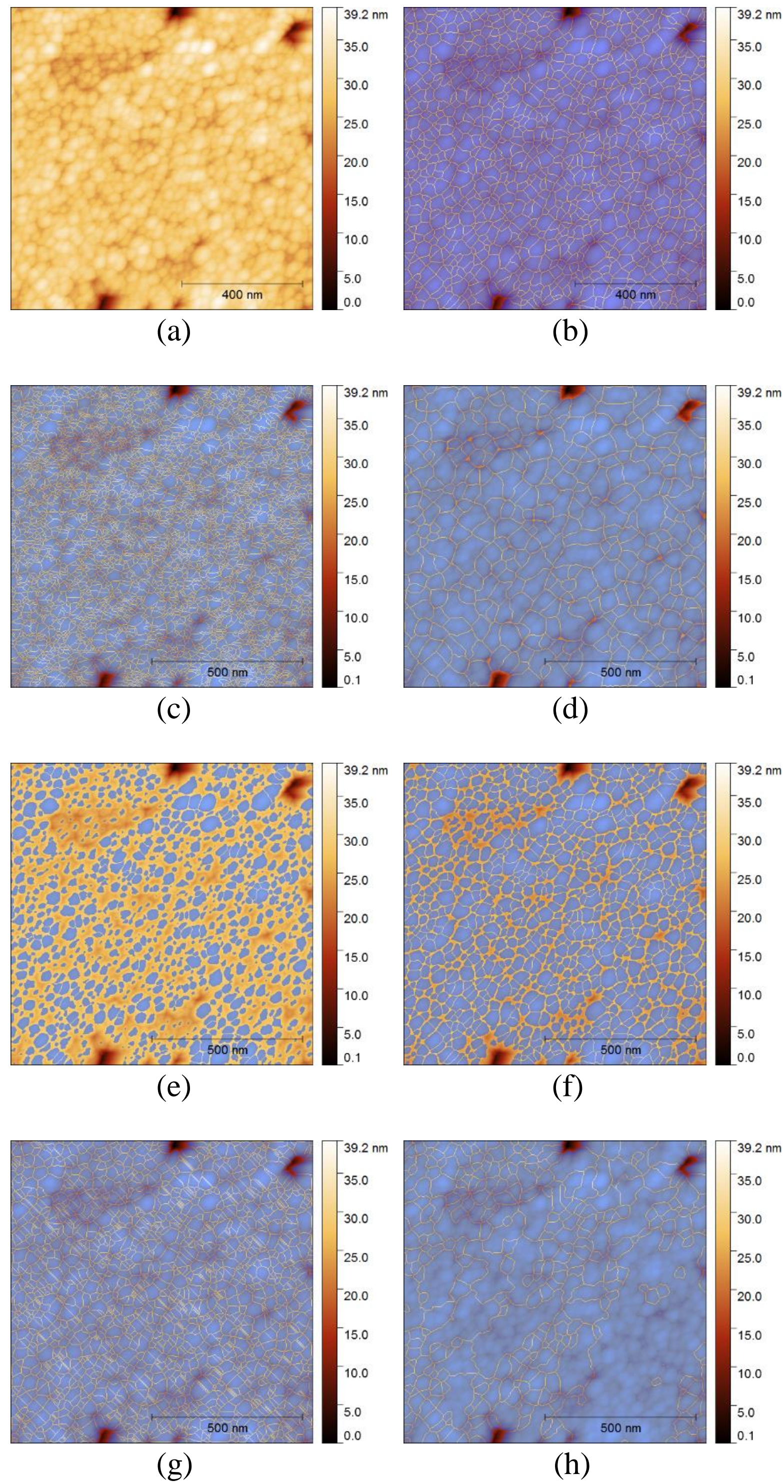

Figure 3.17: Exemplificative application of the segmentation parameters for a ZnS_53 map, where the blue mask marks the grains: *(a)* Original AFM image; *(b)* The same image with a correct choice of parameters; *(c)* A lower Gaussian smoothing; *(d)*A higher Gaussian smoothing; *(e)* A too low barrier level; *(f)* A too high barrier level; *(g)* A too low prefill from minima; *(h)* A too high prefill from minima.

3.2.6 Dips analysis

For a complete morphological characterization of the ZnS a dips analysis has been carried out in order to investigate the dips-associated parameters of the samples like mean dips density, mean dips size and area, in relation to either the sputtering deposition power or the surface parameters like roughness, lateral correlation length, exponential factor and mean grain size. Results with dips distribution for ZnS samples are reported in Chapter 4.

The technique, which has been applied to four 20μm × 20μm maps per sample in order to have a larger statistical confidence for the films, involves the following main steps:

1. Calculation of the mean plane height value z_{plane};
2. Marking grains with height threshold;
3. Map processing;
4. Dips parameters calculation;

In the first step the mean value of the plane has been calculated by extracting five linear profiles for each map with the software Gwyddion to get a series of height distribution for the sample, as shown in Figure 3.18. Then the average height value of the plane z_{plane} has been calculated.

The second step consists in applying a height threshold to the AFM processed image in order to identify the grains of the map with a negative height respect to the mean value of the plane z_{plane}. To do this a height threshold tool from the software Gwyddion has been used. The algorithm marks with a mask each point of the map which have a height lower than the set value z_{segm}. The choice of this parameter has been done for each map starting from observational considerations of the three-dimensional AFM image more than a theoretical approach.

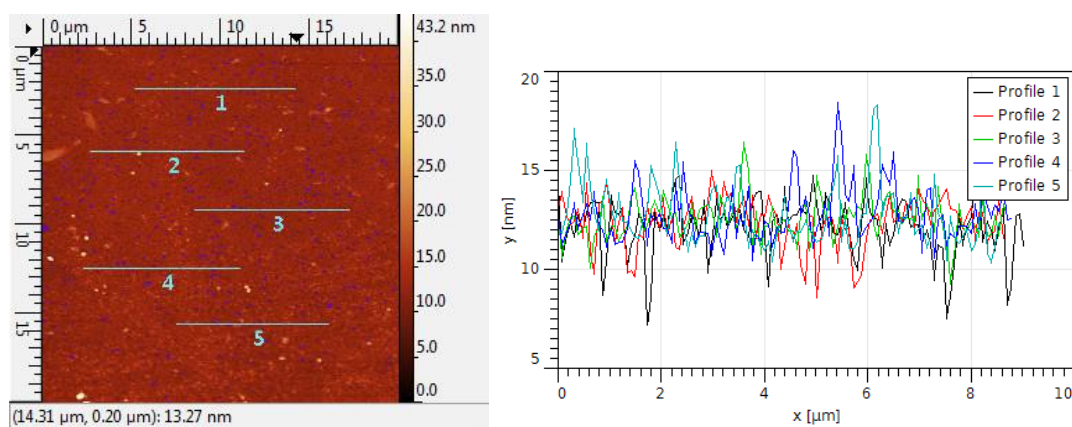

Figure 3.18: Step 1: extraction of five linear profiles from a ZnS_60 map to calculate the mean height value of the plane z_{plane}

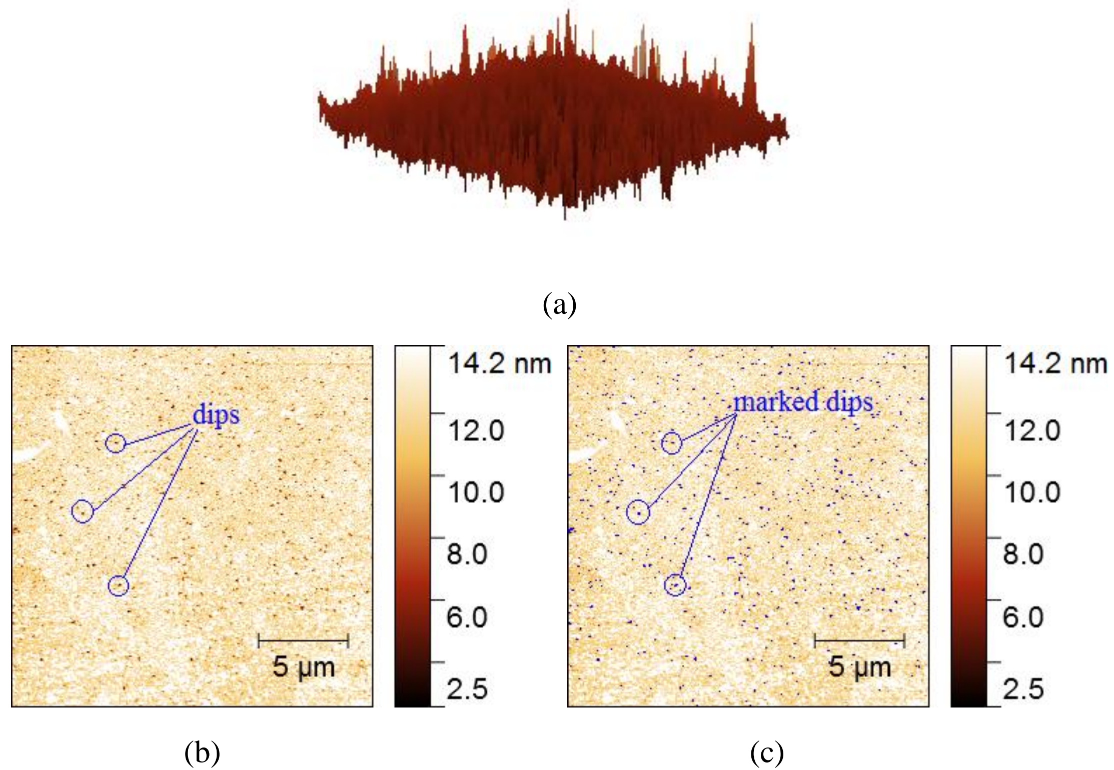

Figure 3.19: Step 2: ZnS_60 dips analysis example of application. *(a)* Three-dimensional profile showing the presence of dips; *(b)* Original AFM processed map; *(c)* Marking with a height threshold application.

The value of this parameter is of primary importance for the dips distributions that have been calculated, but, as it will be shown in Chapter 4, the choice of z_{segm} has been done in such a way to remain in the range of lowest z_{segm} dependence of the dips density but at the same time to get the better marking matching with the dips. The values of z_{segm} that will be reported in Chapter 4 are the result of the very best choice for each processed map in comparison with the original. Each point on the surface that has been defined as dip in this analysis have a height negative value larger than z_{segm}. An exemplificative visual approach of dips and height threshold algorithm application is shown in Figure 3.19.

At this point, as third step, the height scale of each map has been scaled of - z_{plane} to have the plane associated with 0 nm and the dips with a negative z. Then the map color range has been set between $- z_{segm}$ and 0 nm to get in the final image the plane associated with white and everything with height lower than z_{segm} saturated with dark. An exemplificative view of the process is shown in Figure 3.20. With this process the final image obtained represents the mean plane of the sample surface with dips clearly visible also without the application of a mask. In fact, each point with height below the

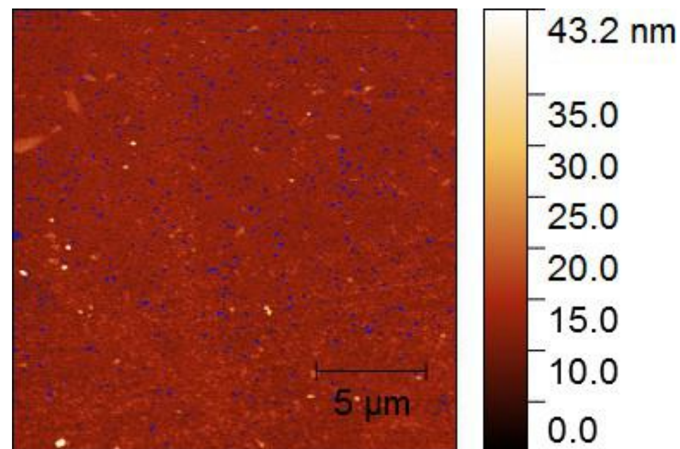

(a)

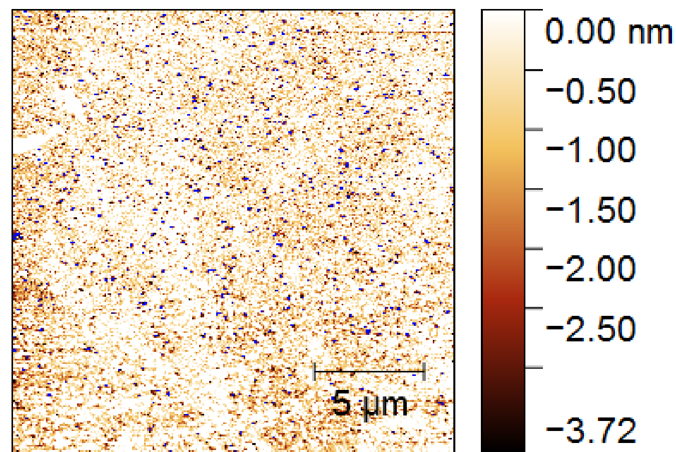

(b)

Figure 3.20: Step 3: *(a)* ZnS_60 map with height threshold; *(b)* Height scaling of $-z_{plane}$ with color range set between -z_{segm} and 0 nm to have the plane associated with white and dips saturated with dark.

set value z_{segm} in this analysis has been defined as a dip for the map, as a result each point in the final image saturated with dark represents a dip, which has been marked to get the dips distribution.

In the fourth and last step the dips density, the mean dip size and area have been calculated with the statistical grains analysis tool provided by Gwyddion, further calculations have been done with OriginPro. All the results, displayed with the sample images, are reported in Chapter 4.

3.2.7 Sheet resistance measurement

An electrostatic characterization of ZnS has been done in two parts, in order to get a more complete description of the samples. At first, sheet resistance has been measured with a four-contacts method, then several maps of surface contact potential have been obtained using Electrostatic Force Microscopy (EFM) and Kelvin Probe Force Microscopy (KPFM) techniques. KPFM maps also have been used to obtain an evaluation of the work function difference between ZnS and Al. All the experimental results of these analyses are reported in Chapter 4.

The sheet resistance is an extensive property of conductors associated to thin films that depends only upon the resistivity and the thickness of the film [77]. For this reason, it is used in characterization of thin film deposition on a substrate, as is the case of the ZnS samples. The definition of the sheet resistance (R_{sheet}) is given by the following equation [78]:

$$R = \frac{\rho}{t}\frac{l}{W} = R_{sheet}\frac{l}{W} \tag{3.19}$$

where R is the electrical bulk resistance, ρ the resistivity, t, l and w the sheet thickness, length and width, respectively. R_{sheet} has been measured with a four-contacts method to obtain an accurate measurement of the real value, avoiding the contact resistance between the metal of the electrode and the semiconductor (ZnS). The four contacts method or four-point probes method, is useful to measure the sheet resistance of thin layers grown by sputtering [79]. The four-point probes has proven to be a tool that makes more accurate measurements than a common two-terminal method [80]. A two-terminal measurement always approximates in excess the real resistance value since it includes the resistance of either the wires or the contacts [80]. The four contact method of measurement is often used to measure sheet resistance of semiconductor thin film because it neglects the contact resistance that forms in a metal-semiconductor junction, which is incorporated in the resistance of the cables [80].

The measurement of R_{sheet} has been done for ZnS_36 which, as it will be shown in Chapter 4, is the sample with the best morphological characterization, meaning the minor dips density. In order to measure R_{sheet} with a four contacts method, four aluminium thin layers have been deposited on the ZnS_36 surface. This has been done applying an Al foil mask at the borders of the sample, with three Au wires placed to separate the four channels. Then, 50 mg of Al has been deposited by thermal evaporation on the ZnS_36 sample, leading to a 125 nm Al-layer, at a vacuum pressure of 2×10^{-2} Torr. Figure 3.21 shows the Al mask and the Al deposited layers.

The measurement of R_{sheet} has been done by applying the four electrodes on the four Al layers, leading current to flow in two terminals and voltage to measure between the other two avoiding the contact resistance.

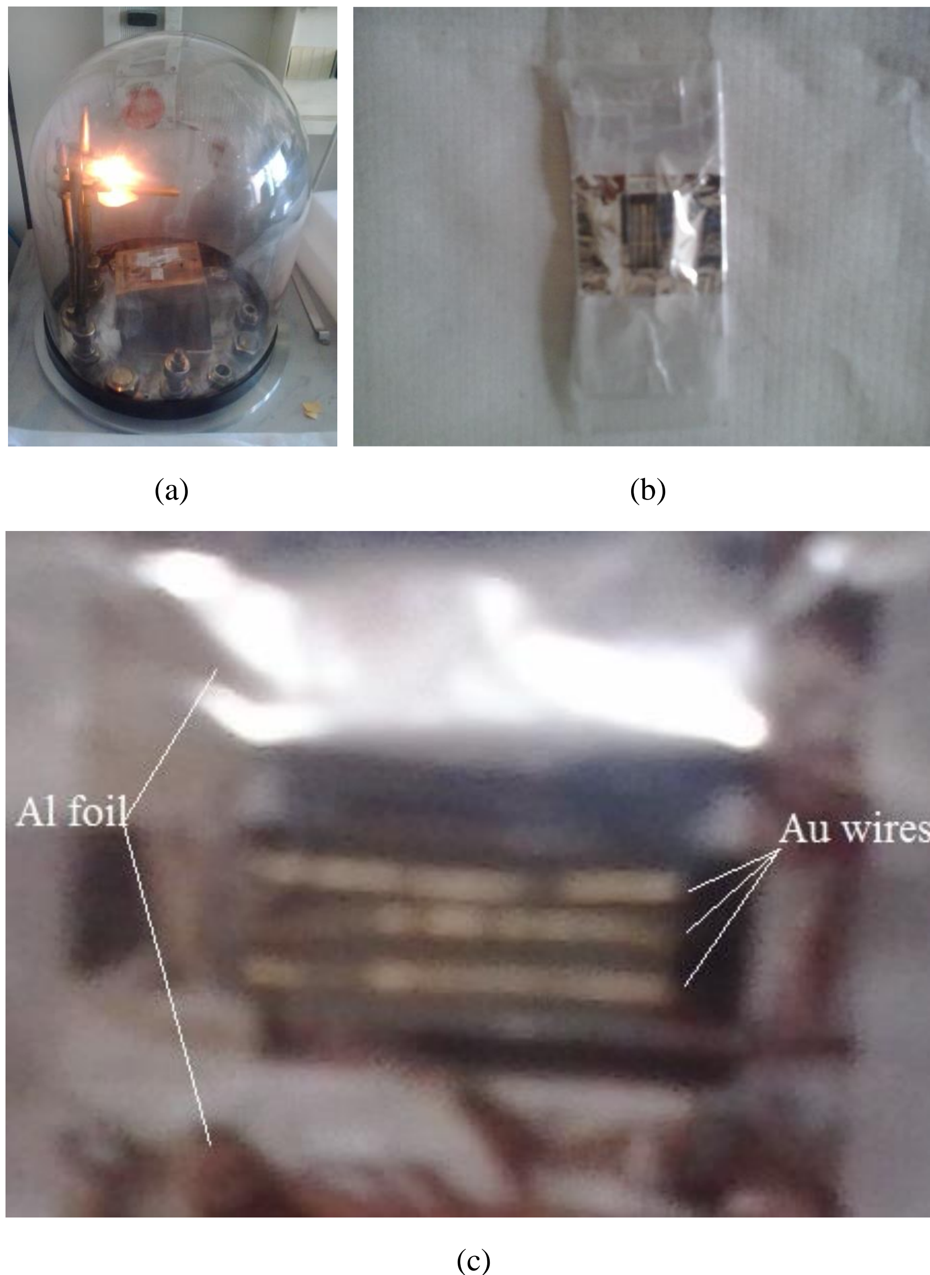

(a) (b)

(c)

Figure 3.21: Preparation of the ZnS_36 sample for the 4-points probe method: *(a)* Thermal evaporation of Al on ZnS_36; *(b)* Macroscopic view of the mask; *(c)* Mask zoom detail; The three Au wires are placed to separate the Al-layers that will be deposited and an Al foil has been put on the borders.

3.2.8 EFM – KPFM characterization

In the last part of ZnS characterization, Electrostatic Force Microscopy (EFM) and Kelvin Probe Force Microscopy (KPFM) have been used in order to obtain contact potential maps and a contact potential difference measurement between the tip and the sample. Both EFM and KPFM provide contact potential maps but where EFM directly measures electrostatic force, KPFM uses a compensation technique to allow a more accurate quantitative determination of the local surface potential [81]. As a result, EFM is more sensitive to topographic artifacts than KPFM. A schematic view of the main principle by which an EFM works is shown in Figure 3.22.

EFM is a dynamic mode non-contact atomic force microscopy used to probe the electrostatic force on a surface by applying a bias voltage between a conductive cantilever tip and the sample [58]. Then a capacitor (*C*) is formed between the two and the *z*-axis component of the electrostatic force between the tip and the surface can be defined as follows [82]:

$$F_{el} = \frac{1}{2}\frac{\partial C}{\partial z}\Delta V^2 \tag{3.20}$$

This force is always attractive because the derivative is negative. The electrostatic force can thus be probed by changing in the voltage: in order to maintain the feedback, the applied voltage on the tip is adjusted such that a constant amplitude is maintained [82].

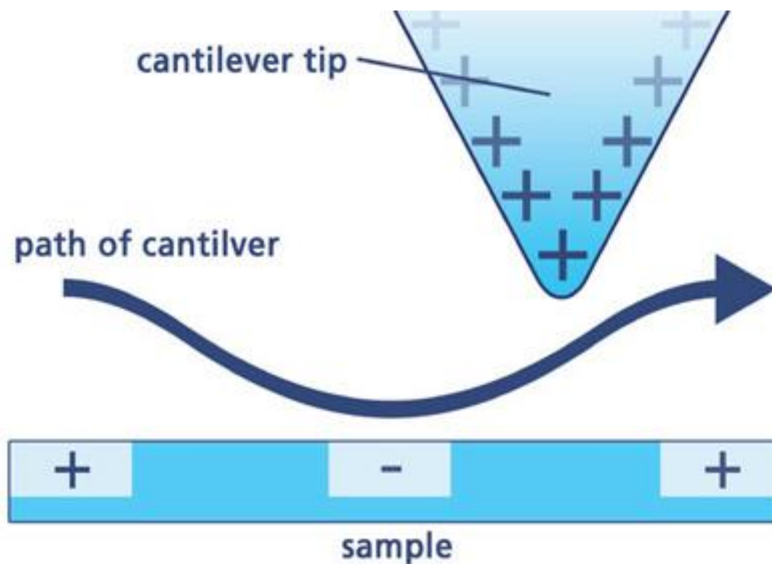

Figure 3.22: Schematic view of the main path followed by the cantilever due to the electrostatic force originated from locally charged domains on the sample surface [58].

Another EFM mode is the constant height mode, where the deflection (or resonance frequency change) of the cantilever, proportional to the electrostatic force, can be measured using the standard optical system [81]. However, to map the surface contact potential, it is crucial to keep the tip at constant height to remove the effect of surface fluctuation. Therefore, first a surface topography is acquired in tapping mode, then the tip is lifted up and retrace the surface profile maintaining a constant tip-surface distance. In this way an EFM can be used to distinguish conductive and insulating regions in a sample [81].

KPFM is also a dynamic mode non-contact atomic force microscopy. With KPFM it is possible to measure the work function of a surface at atomic scales. The work function map obtained by a KPFM scan provides information about the composition and electronic state of the local structures on a sample surface. KPFM is a scanning probe method where the cantilever is a reference electrode which forms a capacitor with the surface [81]. Contrarily to other dynamic modes of operation, the cantilever is not driven at its mechanical resonance frequency, but an alternating current (AC) voltage is applied at this frequency. By applying a direct current (DC) potential difference between the tip and the surface, the sum of the voltages will cause the cantilever to oscillate. This oscillation is detected using the standard optical system. The feedback then changes the DC tip voltage until the frequency associated with the AC component of the voltage vanishes. The DC voltage signal being equal to the contact potential of the surface, i.e. the work function difference between the tip and the sample, is then stored to obtain a work function distribution image of the sample surface [81].

At first, a series of maps have been obtained from a test sample. This consists of two comb shaped Au electrodes on a Si substrate. Each tooth of one electrode lies between teeth of the other, electrically connected to the metal plate sample holder, resulting in one series of electrodes connected to a voltage of 5 V and the other connected to ground. The contact potential difference between two consecutive Au teeth has been measured resulting about 4.9 V. This value is lower than the potential difference applied because the two electrodes are not completely isolated, meaning that a voltage drop exists due to the resistance between electrode and potential source. Images obtained from the test sample measurement have been reported in Figure 3.23. For each measurement, a first morphological scan has been done using standard non-contact mode to set the lift height from surface, obtaining height and phase profile of the sample. Then, a second scan with a conductive tip has been made to obtain a surface contact potential map with an applied potential difference of 5 V between the electrodes.

Once the test sample maps have been obtained, measurements on the ZnS_36 sample have been done. For the ZnS samples, contacts have been made using silver paste applied on the borders. The results for the ZnS films are reported and discussed in Chapter 4.

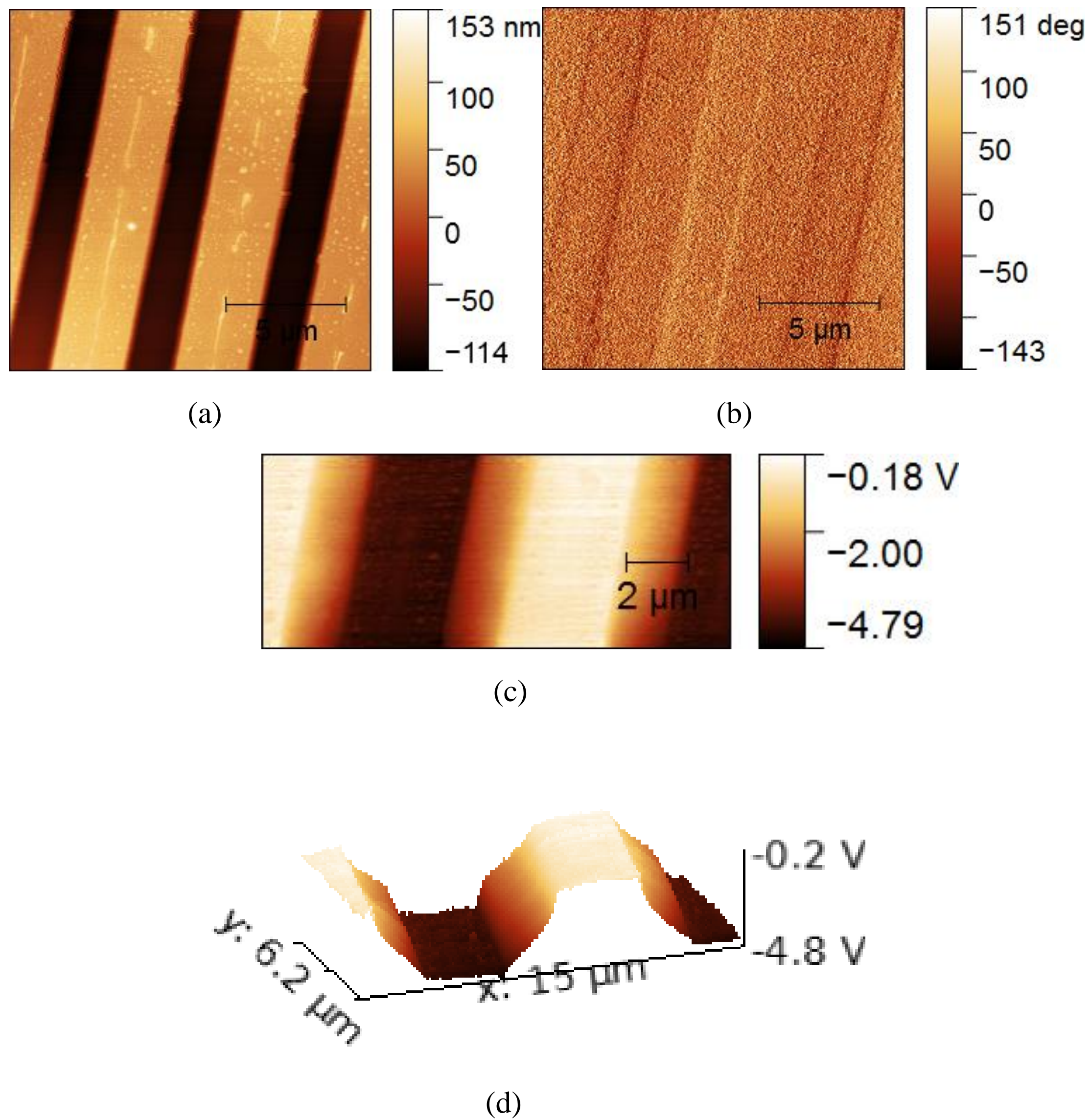

(d)

Figure 3.23: EFM analysis on the test sample. *(a)* Height topography showing the Au electrodes with residuals of the photolithography fabrication process; *(b)* Phase topography; *(c)* Contact potential EFM map. The lighter structures are the Au electrodes connected to the 5 V voltage, while the darker regions are those connected to the ground; *(d)* Three-dimensional contact potential profile.

Chapter 4
Experimental Results

The morphological AFM images resulting for the ZnS and ZnO thin films with all the parameters mentioned in Chapter 3 are reported in Section 4.1. The presence and density of dips are discussed in Section 4.2 with graphs showing the mean associated parameters as a function of the sputtering deposition power (SDP). Surface parameters like roughness R_{HHCF}, lateral correlation length ξ and roughness exponent α have been reported in Section 4.3, in association with the *HHCF* graphs for each sample. Grains analysis results and parameters, that is the equivalent disc radius (EDR) and the grain number (GN), have also been reported in Section 4.3. Furthermore, a more complete characterization is provided by comparisons between ZnS and ZnO structural and grain parameter results that are discussed in Section 4.4. EFM and KPFM contact potential maps have been reported in Section 4.5, where also the *I-V* measurement results of sheet resistance for ZnS are discussed.

4.1 Morphological characterization

In this section the more representative AFM height topography images for the ZnS and ZnO samples are reported, with a brief description of the main AFM parameters used to get the better surface clearness for each sample. Different modes of operation have been used for both AFM NT-MDT and AFM Park, either in attractive or in repulsive interaction regime. Experimental results for parameters characterizing the surface structural and grain properties will be reported in Section 4.3. In the following subsections, the main features of the ZnS and ZnO films morphology are reported.

4.1.1 ZnS morphology

From the AFM images shown in Figure 4.1 and 4.2, is possible to visualize the surface structure and determine the contribution of the sputtering deposition power (SDP) to the main structural properties of the ZnS films. In all cases the ZnS samples cover the substrate in a non-uniform manner, with the presence of dips randomly distributed. From the images depicted in Figure 4.1 and 4.2, it results a dependence on the SDP of the morphology of the ZnS films, but in a way not yet well defined. Indeed, considering the sample with the lowest SDP (ZnS_35), it results a surface structure very similar to that of the samples with the highest SDP (ZnS_60 and ZnS_53), meaning that the grain size is about the same. However, the intermediate SDP sample (ZnS_36) has a totally different morphology, with a large number of smaller grains and a very low presence of dips. This proves a non-linear dependence on the SDP of the ZnS films morphology.

Images of ZnS_35 (SDP_{ZnS_35} = 50 W) depicted in Figure 4.1 *(a)*, show a uniform morphology on large scale (in the order of μm) with the presence of dips. However, the surface structure results flat, as it is visible from the three-dimensional profile. For the ZnS_60 (SDP_{ZnS_60} = 125 W), the situation is about the same, meaning the presence of uniformity and dips of similar size randomly distributed on the surface. Sample ZnS_53 shows a different morphology from the previous two. The sample surface exhibits a discontinue structure in which the last grown epitaxial layer shows non-filled regions, as visible from Figure 4.2 *(b)*. This sample is the one with the largest sputtering power (SDP_{ZnS_53} = 150 W), leading to the conclusion that a very high SDP results in a discontinuous growth deposition, which yields to a non-uniformity of the surface plane. At last, the ZnS_36 sample (SDP_{ZnS_36} = 75 W) is the one that exhibits the better surface morphology. The surface structure results the one with the lowest mean roughness and presence of dips, as visible from the three-dimensional profiles depicted in Figure 4.1 *(b)*. For these reasons, as it will be shown in the Section 4.5, ZnS_36 has been considered the best candidate for the EFM and KPFM characterization.

A further analysis has been performed on a second set of ZnS films (93, 94, 95 and 97) to confirm the properties of samples with a sputtering power of 75 W, namely the absence of dips. Thus the further analyses have been performed on ZnS_36 and not on the whole set of 75 W samples. AFM images of the second set of ZnS thin films are reported in Figure 4.3. From the three-dimensional profiles is visible the peak-valley like structure of ZnS 93, 94 and 95. Sample ZnS_97 is the one showing the more uniform surface profile. From all AFM maps is visible that there is a near total absence of dips, as it is for ZnS_36. This lead to the conclusion that the surface morphology with the lowest presence of dips is the one obtained using a SDP of 75 W. In addition, the surface morphology evolves with different thicknesses, showing more complex structures. In the framework of photovoltaic applications, especially in thin film solar cells, it is important to manage with thin layers, meaning the lowest roughness and density of dips. For this reason, further analyses of these maps, which have proved the absence of dips, have not been performed.

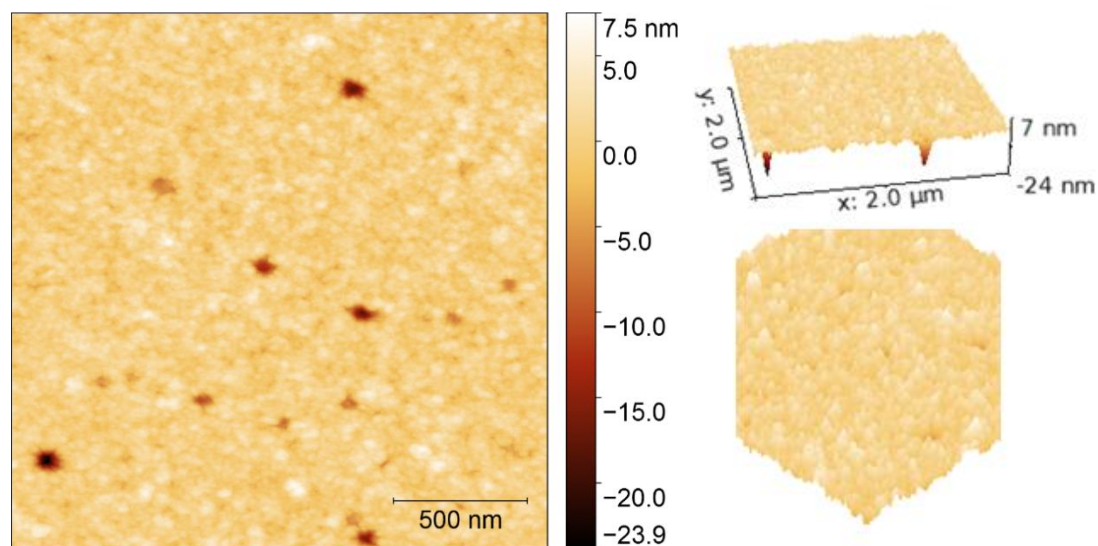

(a)

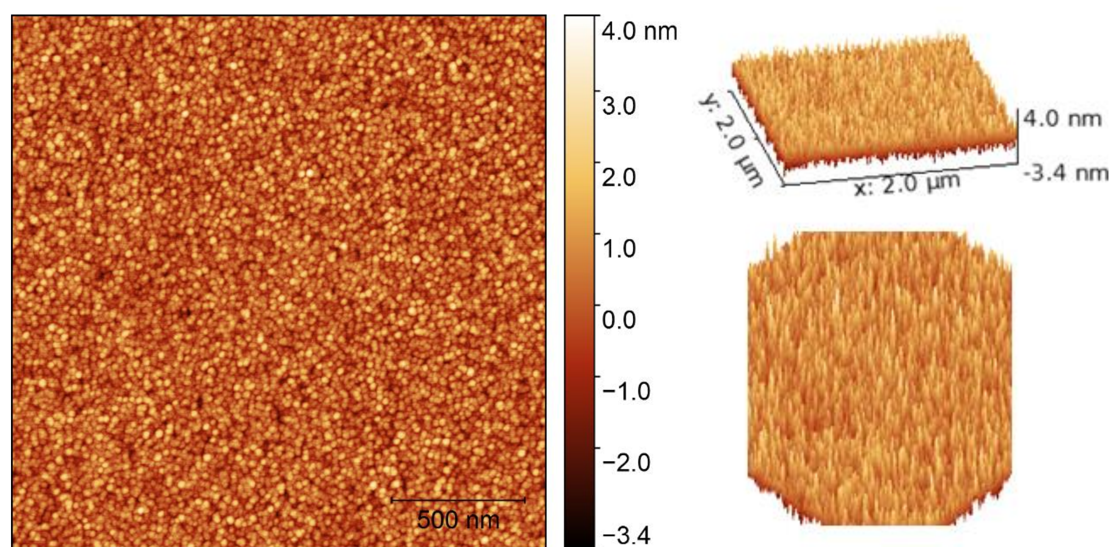

(b)

Figure 4.1: Morphological maps of ZnS_35 (SDP = 50 W) *(a)*, and ZnS_36 (SDP = 75 W) *(b)*, with 3-D profile and its detail. Image obtained using AFM Park. (*Area 2µm × 2µm; Resolution 1024 × 1024 px*^{2})

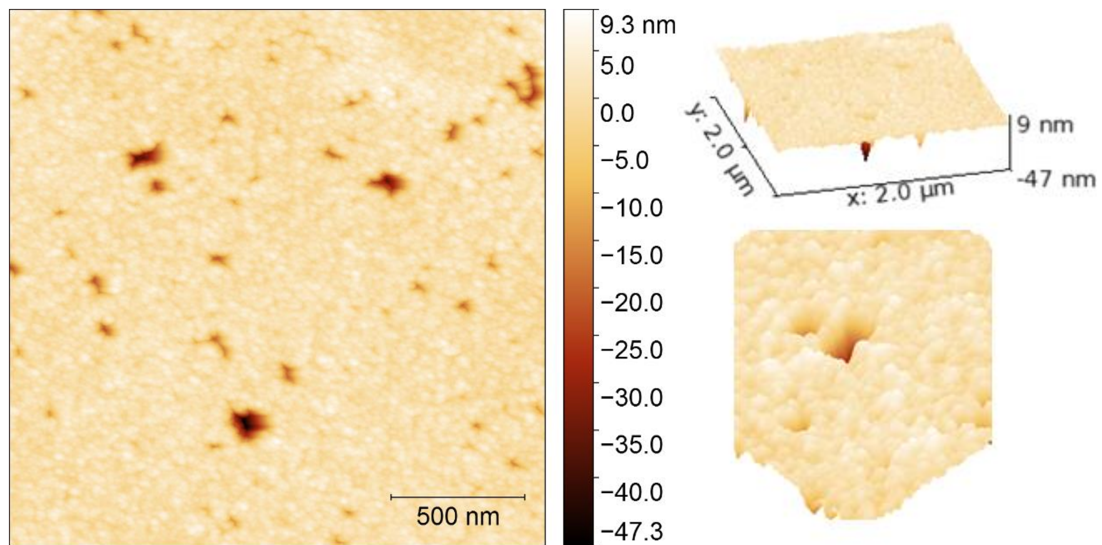

(a)

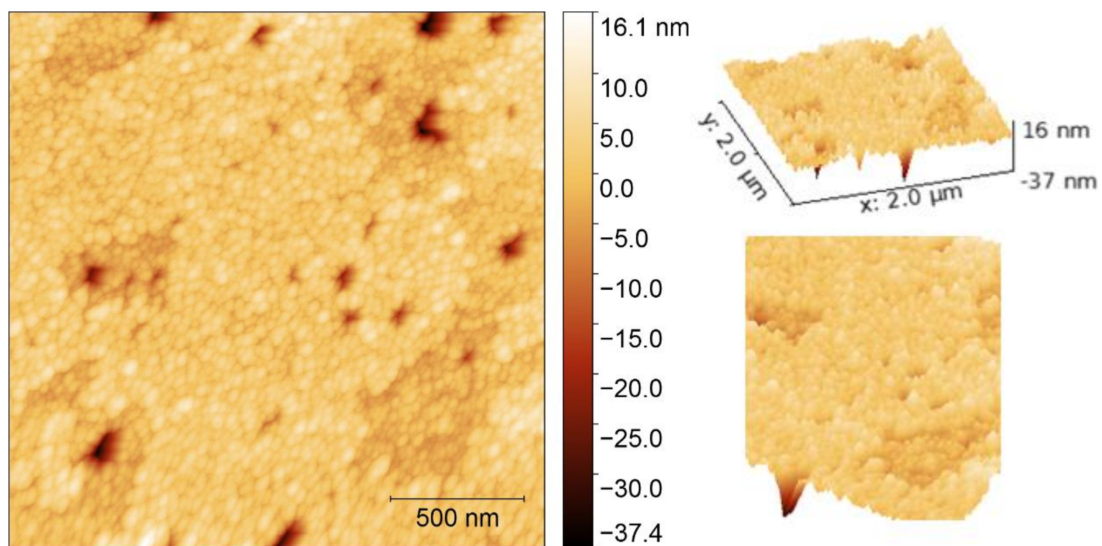

(b)

Figure 4.2: Morphological maps of ZnS_60 (SDP = 125 W) *(a)*, and ZnS_53 (SDP = 150 W) *(b)*, with 3-D profile and its detail. Image obtained using AFM Park. (*Area 2µm × 2µm; Resolution 1024 × 1024 px*^{2})

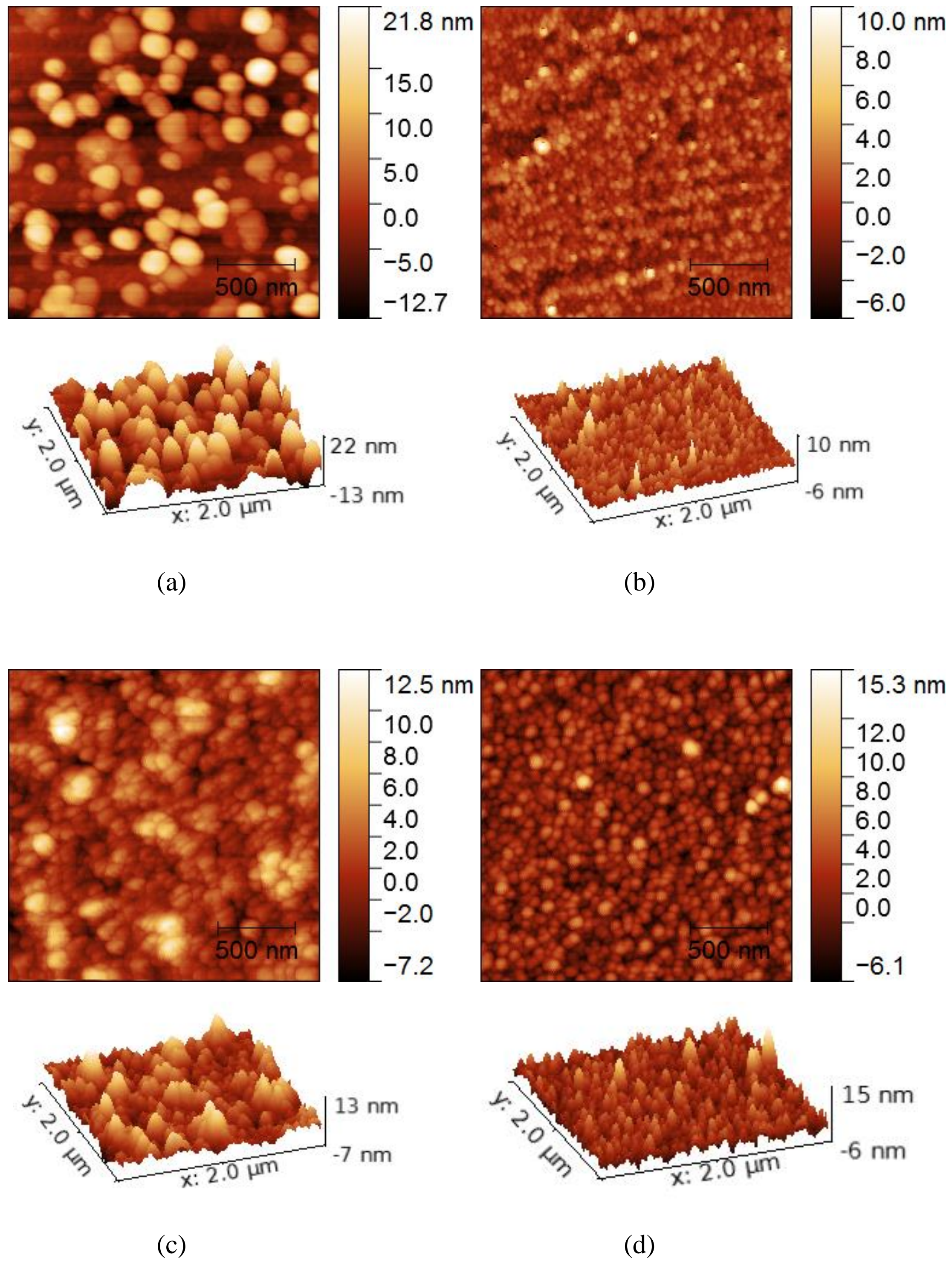

Figure 4.3: Morphological maps of four different ZnS samples grown at a 75W with 3-D profile: *(a)* ZnS_93; *(b)* ZnS_94; *(c)* ZnS_95; *(d)* ZnS_97; Images show a uniform grain distribution and a near total absence of dips. Images obtained using AFM NT-MDT. (*Area 2μm × 2μm; Resolution 256 × 256 px*^{2})

4.1.2 ZnO morphology

AFM measurements have been performed for another zinc compound, as mentioned in Chapter 3: the zinc oxide (ZnO). The characterization of the two ZnO samples, namely ZnO_96 and ZnO_97, has been done mainly as a reference, disregarding of their growth process, with the only motivation to compare morphological features and experimental results associated with the surface and grain analysis with the properties of the ZnS films, as it will be reported in Section 4.3. However, a brief description of the most evident surface features is reported below, with a comparison between the main surface features of ZnS. The AFM images obtained for the ZnO films are depicted in Figure 4.4.

The main structure of ZnO_96 is in general similar to that of ZnS_36, apart from the size of the grains. From the AFM images is possible to view the uniform morphology of ZnO_96, where the grains are homogeneously distributed on the surface This can be viewed from the three-dimensional detail in Figure 4.4 *(a)*. Grains are very near-packed and the presence of dips is totally absent. This is visible from the morphology of the two samples, as it was for ZnS 93, 94, 95 and 96.

For ZnO_97 the surface structure is quite different, due to the presence of bigger grains with a triangular shape randomly distributed among the smallest ones. Uniformity for this sample exists only on very small scale, as it was the case of ZnS_93 and ZnS_95, and the general surface structure is similar to the two ZnS samples.

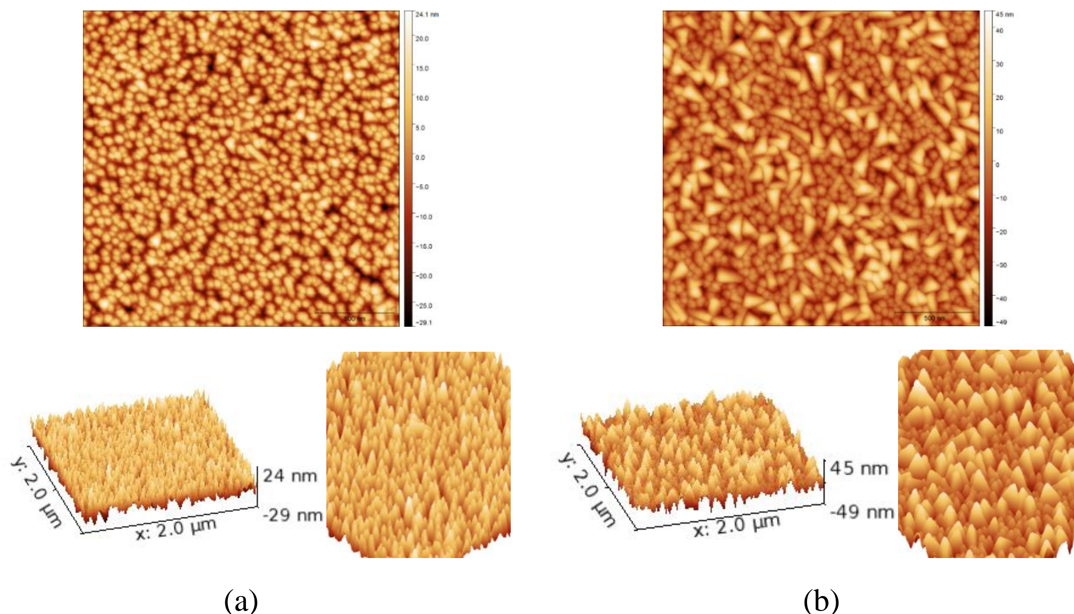

(a) (b)

Figure 4.4: Morphological maps of samples ZnO_96 *(a)*, and ZnO_97 *(b)*, with 3-D profile and its detail. Images obtained using AFM Park. (*Area 2µm × 2µm; Resolution 512 × 512 px*^{2})

4.2 Presence and density of dips

One of the main parameters associated with the quality of the ZnS films is represented by the presence of dip defects, where the lower density of dips means the better choice for ZnS applications. The analysis presented in this section has been performed to characterize the ZnS films in dependence of the sputtering deposition power (SDP). The further electrostatic EFM and KPFM analyses, that will be reported in Section 4.5, have been performed on the sample that shows the lowest presence of dips. Results involving the density and the mean size of dips, calculated from the dip analysis described in Chapter 3, have been reported and discussed in this section. In this work, the motivations behind the existence of dips have not been investigated.

4.2.1 Choice of z_{segm}

In Subsection 3.2.6, Chapter 3, it was described in detail the technique used in order to obtain the mean dip density for each ZnS sample. In this technique, a fundamental role was played by the height threshold value z_{segm}. The choices of z_{segm} performed for ZnS_35 and ZnS_53 are reported as vertical lines in the graphs depicted in Figure 4.5. From the graphs it is possible to view the dip number variation in function of z_{segm}. The careful choice of z_{segm}, as mentioned in Chapter 3, means that the value of height threshold marking during the analysis has been made outside the region with the highest slope, that is outside the region of highest z_{segm} dependence for the dip number. The choice of z_{segm} was done mainly on the better match between the dips and the marking mask. However, looking from the graphs depicted in Figure 4.5, a superior limit over which the choice of z_{segm} would have led to the possibility of an incorrect evaluation of the parameters has been established. In Table 4.1 is shown the dip number variation for two different regions of the plot, corresponding to different slopes of the function. The calculation of parameters associated with dips has been done in two steps: first, obtaining results from 20µm × 20µm maps with the technique described in Chapter 3, and then averaging the experimental results of four different maps for each sample to get more accurate values.

Table 4.1: Mean variations of the dip number corresponding to a z_{segm} change of ± 0.1 nm in the regions of lowest and highest slope shown in Figure 4.5.

ZnS sample	35	53
Low-slope dip number variation	±120	±25
High-slope dip number variation	±440	±240

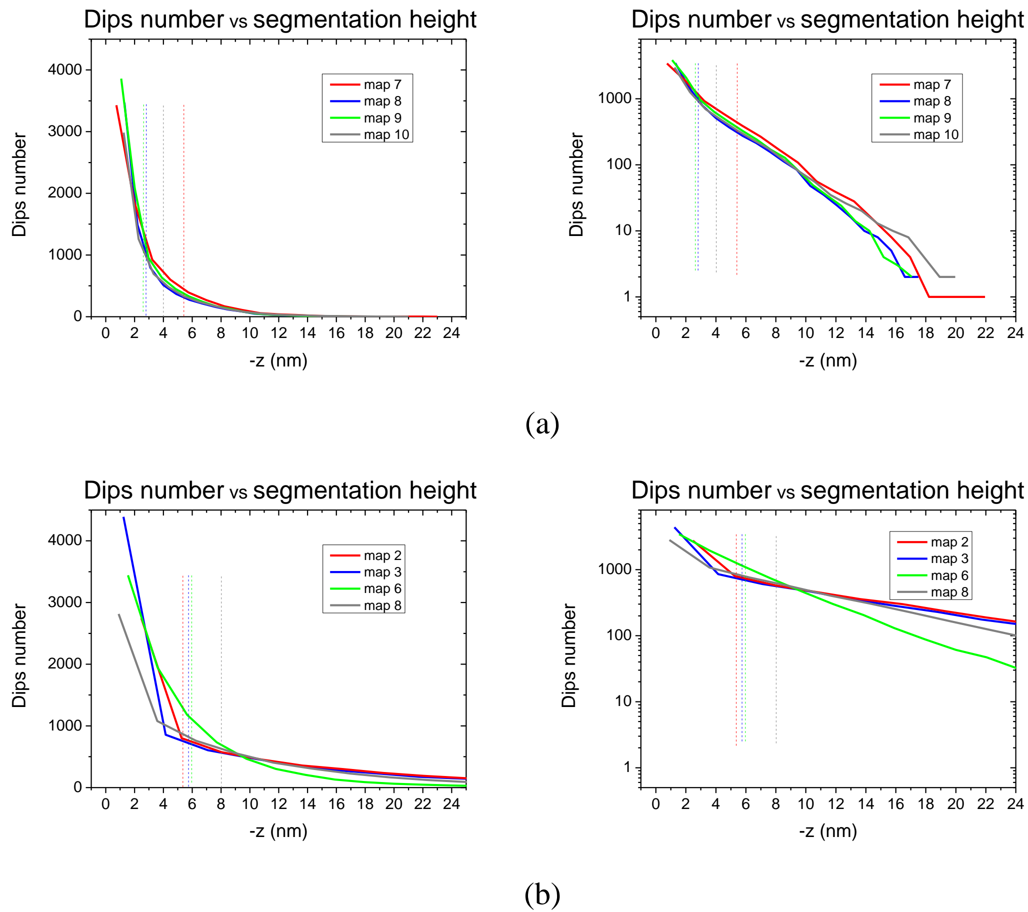

Figure 4.5: Plots of the total mean dip number calculated over four 20μm×20μm maps per sample in function of the z_{segm} chosen value shown in linear (*left*) and logarithmic (*right*) profile, for the analysis of ZnS_35 *(a)* and ZnS_53 *(b)*. The vertical lines intercept the z_{segm} value of each map. From the graphs is possible to view the careful choice of z_{segm} done outside the region of highest slope.

The images after the dip analysis are shown in Figure 4.6 and 4.7. As described in Chapter 3, the value of z_{segm} represents the negative height value at which a point on the surface begins to be defined as a dip. Thus this distance is referred to the mean plane height value, namely z_{plane}, which has been calculated for each map.

Table 4.2: Mean z_{segm} for each sample. Values have been obtained by averaging over four maps per sample.

ZnS sample	35	36	60	53
$\bar{z}_{segm}$**(nm)**	3.7	2.4	3.6	6.3

In Table 4.2 the mean z_{segm} values for each sample are reported. These results have been calculated by averaging the four values of z_{segm} associated to the four maps per sample. These values do not show the deepness of dips, but the average negative height at which a point on the surface starts to be considered a dip in the analysis. The results are not only in the same order of magnitude, but very close to each other, apart from ZnS_53, which is the sample showing the larger z_{segm} average value.

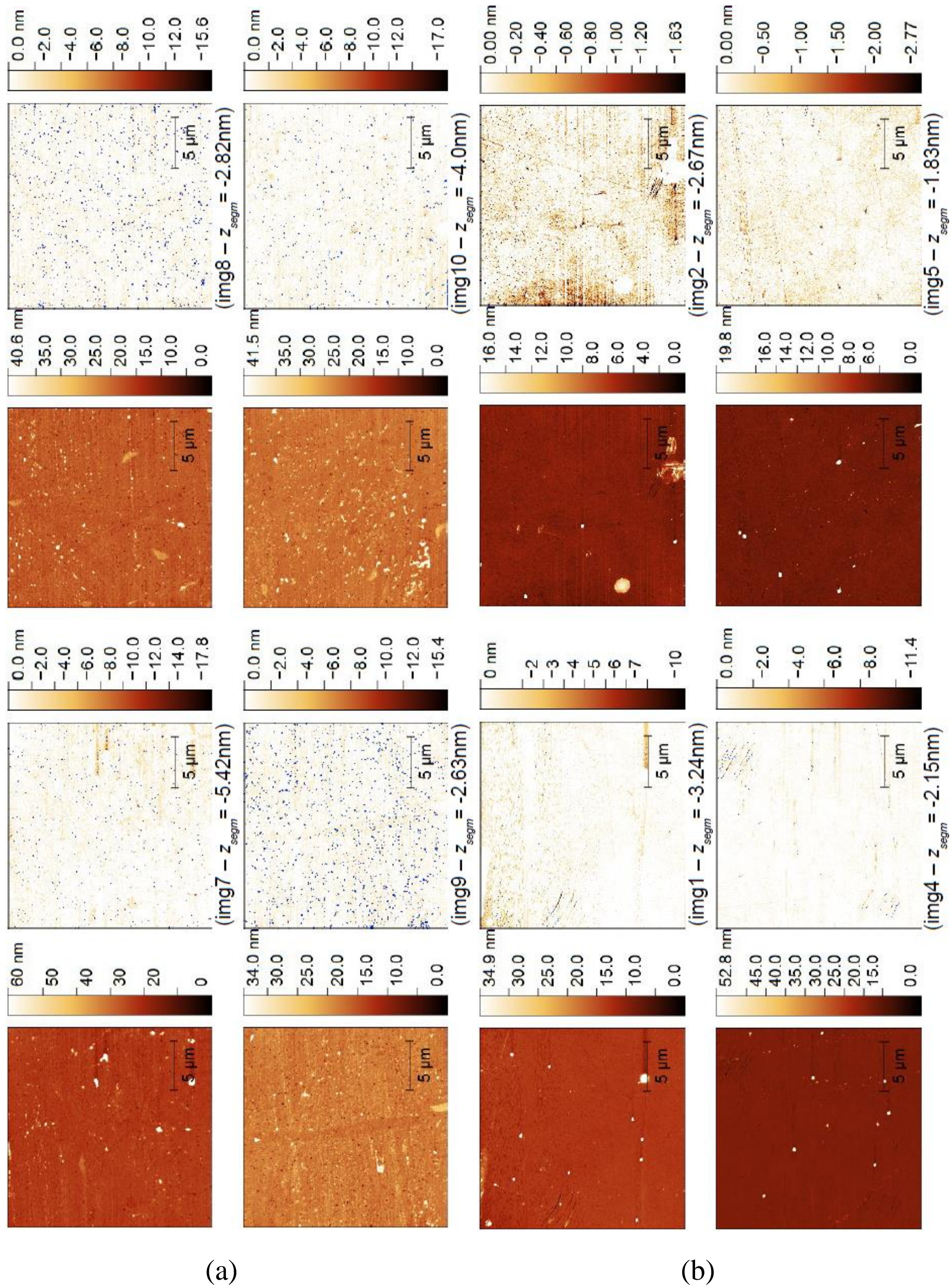

Figure 4.6: Dip distribution evaluation analysis: AFM morphological images (*left*) and final results of the four-step dip marking technique (*right*) for ZnS_35 *(a)* and ZnS_36 *(b)*. Images show the grains marked as "dips" and the relative choice of z_{segm}. In the right-side images the 0.0 nm height value represents the mean height value of the plane z_{plane} after the z-shifting of the original maps. Note the near absent presence of dips for ZnS_36. Images obtained using AFM NT-MDT. *(Area: 20µm × 20µm; Resolution: 256 × 256 px²)*

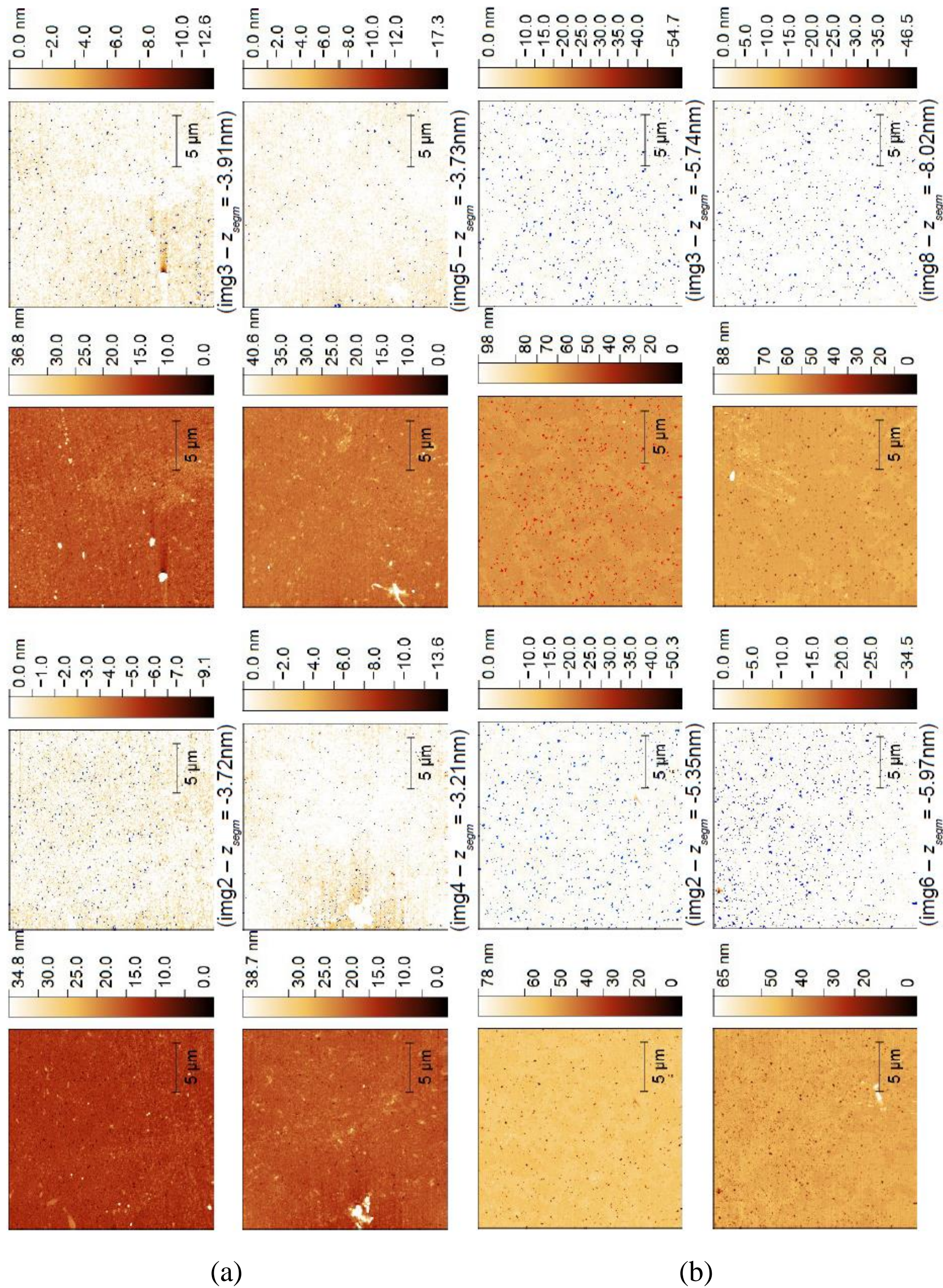

Figure 4.7: Dip distribution evaluation analysis: AFM morphological images (*left*) and final results of the four-step dip marking technique (*right*) for ZnS_60 *(a)* and ZnS_53 *(b)*. Images show the grains marked as "dips" and the relative choice of z_{segm}. In the right-side images the 0.0 nm height value represents the mean height value of the plane z_{plane} after the z-shifting of the original maps. Images obtained using AFM NT-MDT. (*Area: 20µm × 20µm; Resolution: 256 × 256 px*^{2}*)*

4.2.2 Dip analysis results

After the dips are marked, the associated parameters have been calculated at first for each map and then averaging the results of four maps per sample. Results have been reported in the following graph depicted in Figure 4.8, in which the dependence on the SDP has been shown. From the AFM images depicted in Figure 4.6 and 4.7, the density distribution of dips for ZnS_35, which is very similar to the distribution of dips shown by ZnS_53, results large. The main differences in the analysis between the two samples is the value of z_{segm} chosen for each sample. The mean size of dips has been evaluated of about 100 nm, further analyses of the dip size and area have not been done because of the too low resolution achievable in the measurement.

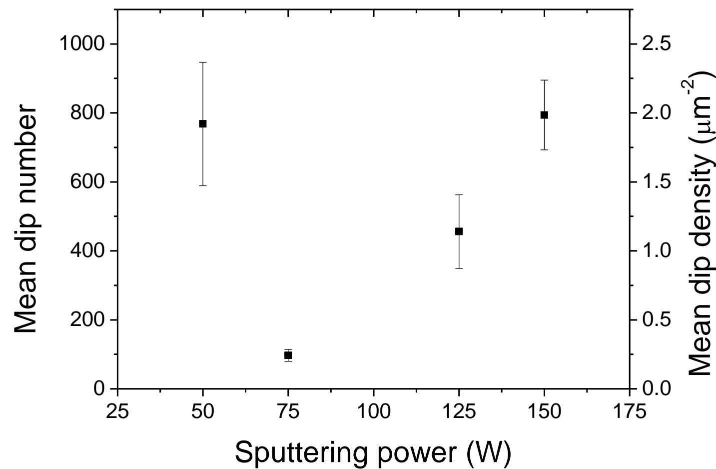

Figure 4.8: Mean dip number per map and density as a function of the sputtering deposition power (SDP) for the ZnS samples.

From the results, the 50 W and the 150 W samples are those with the largest total number of dips and thus the larger dip density, as visible from Figure 4.8. The dip arrangement can be viewed both from the two and the three dimensional morphological profiles shown in Section 4.1, Figure 4.1 and 4.2. Another important consideration has to be made about ZnS_36, which shows a near-absent dip distribution.

Those results yield to the conclusion that a non-linear SDP dependence of the dip associated parameters exists. The main motivation it is shown from the graphs above, in which the 75 W sample (ZnS_36) exhibits the lowest values of the dip density. An analogous consideration may be done about the 50 W sample (ZnS_35): this is the sample with the lowest SDP, and exhibits a large dip density. The sample with the largest SDP (150 W), also exhibits a large dip density, which is very similar to ZnS_35. The experimental results show that ZnS thin films grown with a 75 W possess a morphology associated to a surface with a low presence of dips. As it will be shown in Section 4.3, the 75 W sample is the one with the highest number of grains, while ZnS

films with the largest dip density, that is the 50 W and 150 W samples, will result as the those with the lowest number of grains, leading to the conclusion of an inverse dependence between the two parameters.

The second set of ZnS films grown with a 75 W, namely ZnS 93, 94, 95, 97, has been checked in order to verify that at 75 W a minimum dip density is obtained. In fact, as mentioned in Section 4.1, these films exhibit a surface structure very similar to that of ZnS_36, which also has been grown with a 75 W. From the analysis of the AFM morphological maps of these film it results that the presence of dip on the surface is totally absent, thus confirming the conclusion that a 75 W provides for ZnS thin films the lowest dip density. From the images depicted in Figure 4.3 it is possible to view the absence of dips, while in the first ZnS set of samples dips were visible with black points randomly distributed on the surface.

4.3 Structural and grain properties

Experimental results from the ZnS thin films structural and grain analyses have been reported in this section. For each sample, both the graphs and the parameters obtained from the analyses have been displayed in a single subsection, where a brief discussion about the values calculated for the structural and grain associated parameters has been also reported. Experimental results have been obtained in different ways. First, the surface roughness (R_{HHCF}), the lateral correlation length (ξ) and the Hurst exponent (α) have been extracted from the self-affine fit of *HHCF* data. In addition, the average surface roughness $R*$ has been calculated by averaging all values over the map.

Secondly, the image segmentation method has been applied on the AFM processed images with a correct choice of the segmentation parameters that also has been reported. From the segmentation, the grain number (GN) has been extracted for each sample. Moreover, the equivalent disc radius (EDR) distribution has been obtained to calculate the mean EDR (MDR) value associated to the grains of each sample. The results for both R_{HHCF} and $R*$ are shown and discussed in this section, where are also reported all the *HHCF* data graphs obtained from the analysis, in which the self-affine fitting function has been displayed. *HHCF* data have been extrapolated from the five best AFM height topography 1μm × 1μm maps and then fitted by the exponential function shown in Eq. (3.18), in the approximation for a self-affine surface. From the self-affine fit of the *HHCF* data, the statistical parameters that characterize the surface grain properties have been extracted for each sample, namely the surface roughness R_{HHCF}, the lateral correlation length ξ and the Hurst exponent α.

Furthermore, the mean values of the parameters have been calculated by averaging the values of the five maps per sample. The image segmentation method described in Chapter 3 has been applied averaging values of five maps per sample. The choice of segmentation parameters has been also reported and discussed for one map per sample in this section. Furthermore, as for the ZnS, AFM maps of the ZnO films were also acquired. A direct comparison between the ZnS and the ZnO structural and grain properties will be done in Section 4.4.

4.3.1 50 W - ZnS_35

Figure 4.9 shows the optimal agreement of the self-affine fit with the *HHCF* experimental data distribution in the graph. The resulting values for the parameters are reported in Table 4.3. The R_{HHCF} value results to be within the $R*$ error range. The roughness exponent α is comparable to the other samples, which means a lower roughness of the surface profile. Furthermore, the lateral correlation length ξ has almost the largest value among the ZnS samples, as it will be shown in Section 4.4.

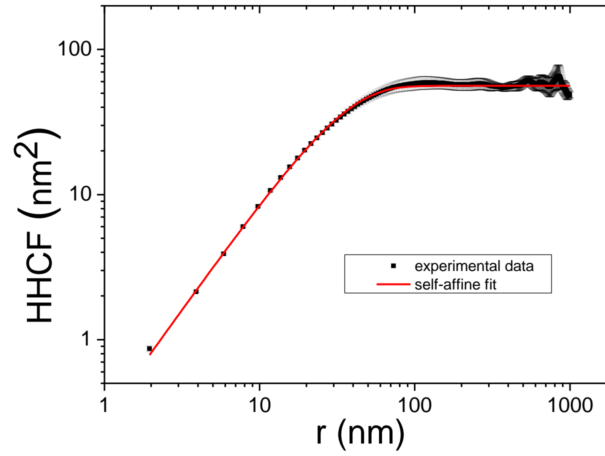

Figure 4.9: *HHCF* experimental data (*black dots*) as a function of the distance between points on the surface in logarithmic scale for ZnS_35. *HHCF* has been fitted by the self-affine function (*red line, see Eq. 3.18*). Parameters extrapolated from the fit have been reported in Table 4.3.

Table 4.3: Mean values of parameters for ZnS_35. R_{HHCF}, ξ and α evaluated from self-affine fitting of *HHCF* data. $R*$ evaluated by averaging over all maps.

Parameters	Value
R_{HHCF} (nm)	1.675 ± 0.003
ξ (nm)	33.7 ± 0.2
α	0.748 ± 0.003
$R*$ (nm)	1.5 ± 0.6

From the image segmentation depicted in Figure 4.11 *(a)* and *(b)*, it is possible to view the grain arrangement on the surface of the sample. The results reported in Table 4.5 show a EDR that is smaller than the lateral correlation length. This could mean that at a 50 W sputtering power a grain clustering occurs in the ZnS films. The grain clusters formed on the surface are also visible from the images shown in Figure 4.1 *(a)* (Section 4.1), where can be viewed as bigger grains distributed among the smaller ones. The GN value results to be 1200, which is a high value compared to the other samples. The image segmentation shows a very packed structure of the grain boundaries, which lead to the elevated GN value calculated. From the results, the following conclusion can be drawn about the grain analysis of the 50 W ZnS film: the surface profile is smooth, apart from the presence of dips, with a structure composed by about 1200 grains with a mean size of 14.5 nm, alternated with few bigger grains that result from a grain clustering process, which is due to the large lateral correlation length value (larger than the EDR) of the sample.

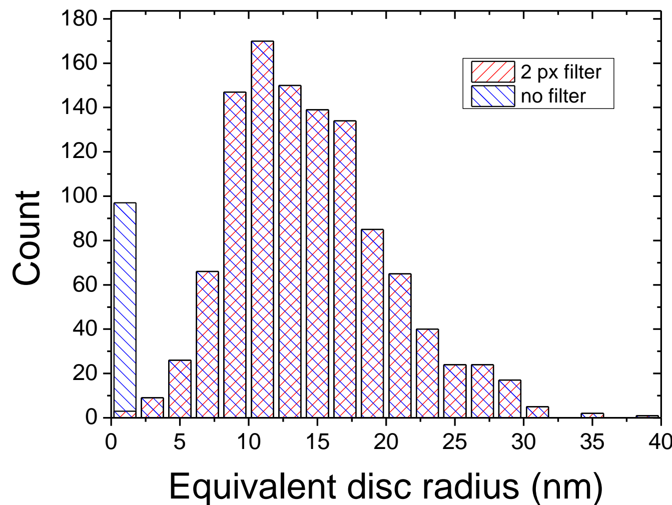

Figure 4.10: Equivalent disc radius distribution of the grains with the application of the 2 px^2 filter (*red*) and without (*blue*) for ZnS_35. The MDR has been calculated by averaging the distribution without the contribution of grains with an area smaller than 2 px^2 (represented by the blue column on the left of the histogram), which would have led to an incorrect evaluation of the parameter.

Table 4.5: Grain number and equivalent disc radius results for ZnS_35. MDR has been calculated by the equivalent disc radius distribution shown in Figure 4.12.

Parameters	Value
GN	1200
MDR (nm)	14.5 ± 0.1

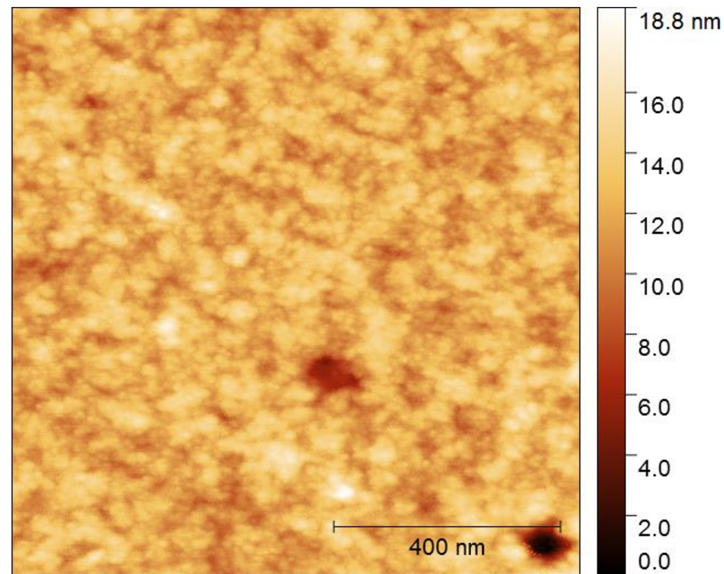

(a)

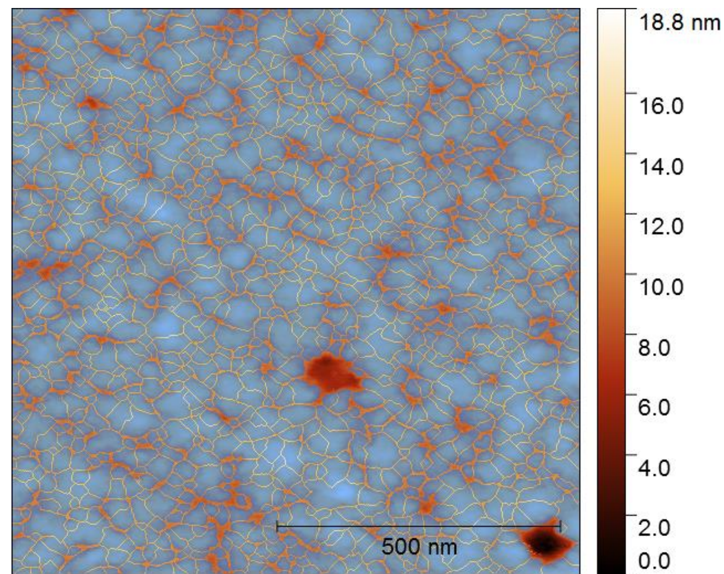

(b)

Figure 4.11: Image segmentation of the ZnS_35 1µm × 1µm map for the evaluation of the GN and EDR. *(a)* Height topography map acquired in non-contact mode; *(b)* Application of the segmentation mask on the map. The segmentation parameters are listed in Table 4.4. (Image obtained using AFM Park)

Table 4.4: Segmentation parameters values used for the grain analysis of the ZnS_35. The parameters description is reported in Section 3.2.5, Chapter 3.

Parameters	GS	AG	AC	BL	PL	PFM
Set Value	5.00 px	0.00 %	49.01 %	55.02 %	0.00 %	5.00 %

4.3.2 75 W - ZnS_36

The graph depicted in Figure 4.12 shows an optimal self-affine fit for the *HHCF* data of the sample. From the results shown in Table 4.6, the values of R_{HHCF} and R^* are very close to each other, with the statistical error for R_{HHCF} extremely small. The lateral correlation length exhibits a low value compared to the other samples. The roughness exponent α results to be close to 1. However, from the calculated values it results a lower surface roughness for ZnS films grown at a 75 W respect to other samples.

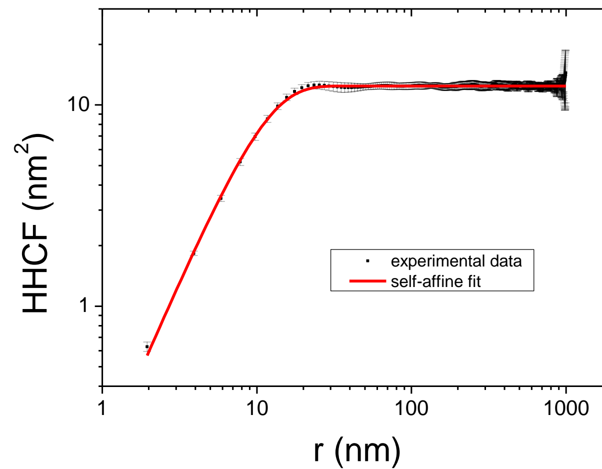

Figure 4.12: *HHCF* experimental data (*black dots*) as a function of the lateral separation of surface heights in logarithmic scale for ZnS_36. *HHCF* has been fitted by the self-affine function (*red line, see Eq. 3.18*). Parameters extrapolated from the fit have been reported in Table 4.6.

Table 4.6: Mean values of parameters for ZnS_36. R_{HHCF}, ξ and α evaluated from self-affine fitting of *HHCF* data. R^* evaluated by averaging over all maps.

Parameters	Value
R_{HHCF} **(nm)**	0.7879 ± 0.0002
ξ **(nm)**	10.82 ± 0.07
α	0.893 ± 0.006
R^* **(nm)**	0.78 ± 0.07

The results reported in Table 4.8 show that the value of GN is the largest obtained among the ZnS samples. This value is visible from the images depicted in Figure 4.14 *(a)* and *(b),* where is possible to view the arrangement of the grains for the sample. The EDR value results the lowest between the ZnS samples, which means that the smallest grains are formed by a 75 W sputtering power growth. Hence, the smallness of grains leads to the large value of GN calculated. Furthermore, the MDR value is higher than the lateral correlation length calculated. Therefore, no clustering processes exist for this sample. Considerations from the results are the following: at 75 W the ZnS film shows a very flat surface profile (with the absence of dips shown in Section 4.2), where the main structure is formed by tiny grains not clustered to each other, leading to a reduced roughness on the surface.

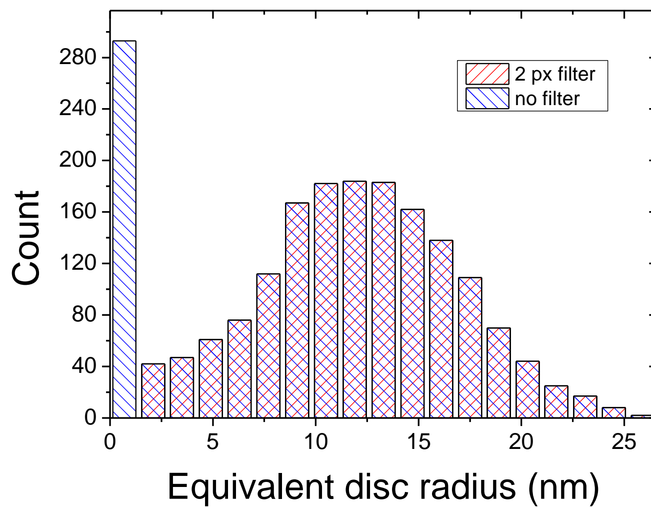

Figure 4.13: Equivalent disc radius distribution of the grains with the application of the 2 px^2 filter (*red*) and without (*blue*) for ZnS_36. The MDR has been calculated by averaging the distribution without the contribution of grains with an area smaller than 2 px^2 (represented by the blue column on the left of the histogram), which would have led to an incorrect evaluation of the parameter.

Table 4.8: Grain number and equivalent disc radius results for ZnS_36. MDR has been calculated by the equivalent disc radius distribution shown in Figure 4.15.

Parameters	Value
GN	1630
MDR (nm)	12.2 ± 0.1

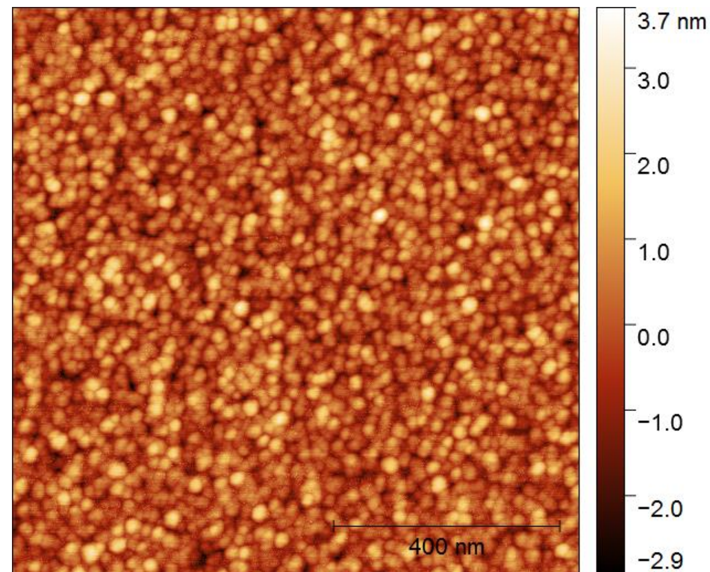

(a)

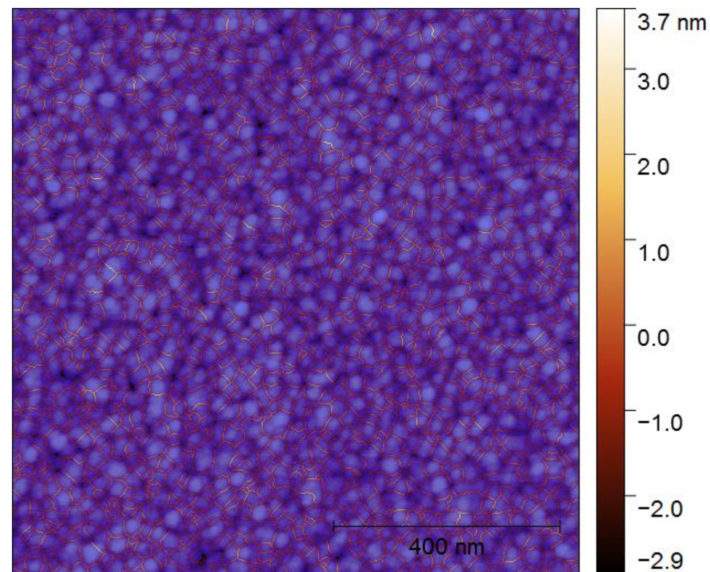

(b)

Figure 4.14: Image segmentation of the ZnS_36 1µm × 1µm map for the evaluation of the GN and EDR. *(a)* Height topography map acquired in non-contact mode; *(b)* Application of the segmentation mask on the map. The segmentation parameters are listed in Table 4.7. (Image obtained using AFM Park)

Table 4.7: Segmentation parameters values used for the grain analysis of the ZnS_36. The parameters description is reported in Section 3.2.5, Chapter 3.

Parameters	**GS**	**AG**	**AC**	**BL**	**PL**	**PFM**
Set Value	1.89 px	0.00 %	3.85 %	90.12 %	0.00 %	3.69 %

4.3.3 125 W - ZnS_60

The self-affine fitting of the experimental data does not provide an optimal match, as it was for the ZnS 35 and 36 samples, as visible from the graph depicted in Figure 4.15. In Table 4.9 are shown the experimental results calculated for the sample. R_{HHCF} and R^* show large values that are in agreement to each other. The lateral correlation length value is close to that of the ZnS_35 sample. The roughness exponent α results to be large.

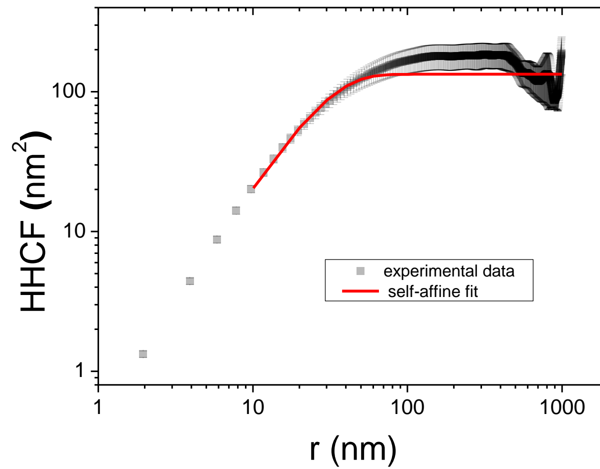

Figure 4.15: Graph showing the *HHCF* experimental data (*black dots*) as a function of the lateral separation of surface heights in logarithmic scale for ZnS_60. *HHCF* has been fitted by the self-affine function (*red line*). Parameters extrapolated from the fit have been reported in Table 4.9.

Table 4.9: Mean values of parameters for ZnS_60. R_{HHCF}, ξ and α evaluated from self-affine fitting of *HHCF* data. R^* evaluated by averaging over all maps.

Parameters	Value
R_{HHCF} **(nm)**	2.58 ± 0.01
ξ **(nm)**	29.0 ± 0.8
α	0.84 ± 0.01
R^* **(nm)**	2.5 ± 1.2

Images depicted in Figure 4.17 *(a)* and *(b)* show the grain arrangement on the surface of the ZnS_60 sample. As visible from the images, grain boundaries are spatially very separated from each other, with grains varying in size from small ones to

large clusters. The lateral correlation length results larger than the MDR. The GN is about the same of the 50 W sample (ZnS_35), that is a high number of grains is present on the surface. From the results, a dense grain structure is present on the sample, similar to that of ZnS_35. Both R_{HHCF} and α result to have large values.

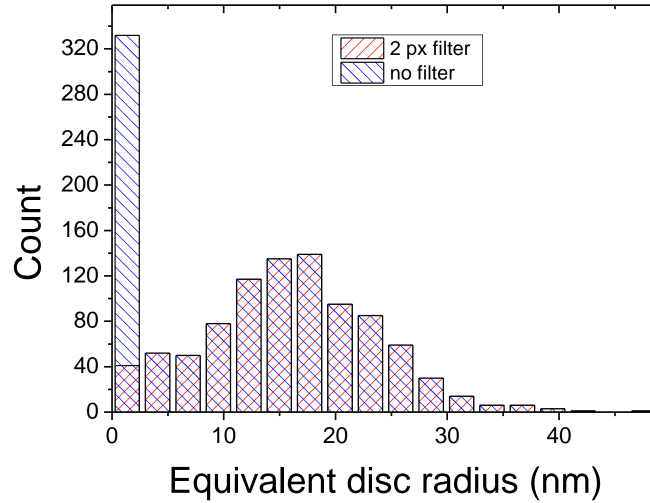

Figure 4.16: Equivalent disc radius distribution of the grains with the application of the 2 px^2 filter (*red*) and without (*blue*) for ZnS_60. The MDR has been calculated by averaging the distribution without the contribution of grains with an area smaller than 2 px^2 (represented by the blue column on the left of the histogram), which would have led to an incorrect evaluation of the parameter.

Table 4.11: Grain number and equivalent disc radius results for ZnS_60. MDR has been calculated by the equivalent disc radius distribution shown in Figure 4.18.

Parameters	Value
GN	1200
MDR (nm)	16.0 ± 0.2

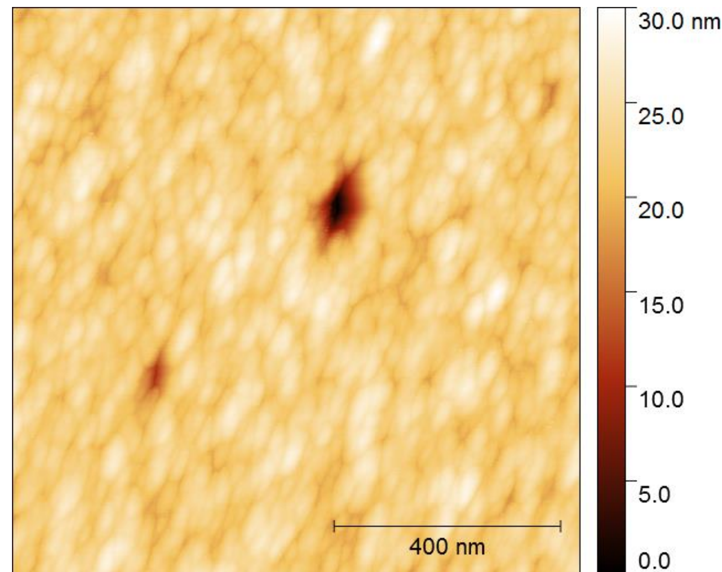

(a)

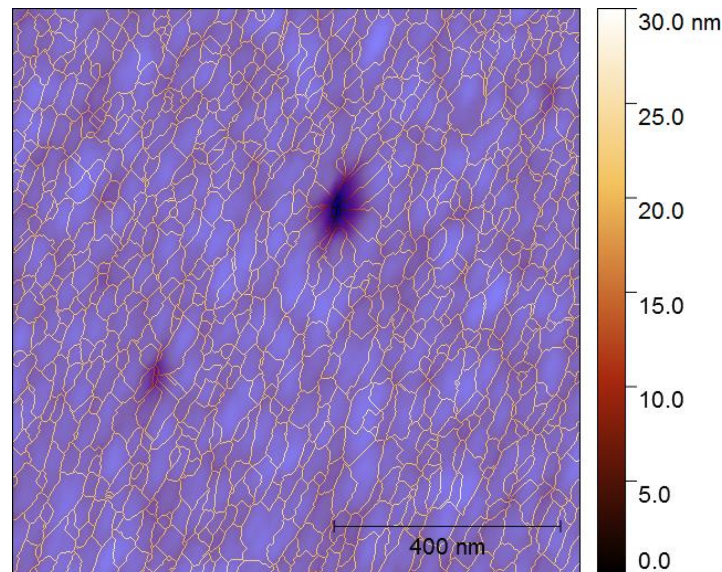

(b)

Figure 4.17: Image segmentation of the ZnS_60 1µm × 1µm map for the evaluation of the GN and EDR. *(a)* Height topography map acquired in non-contact mode; *(b)* Application of the segmentation mask on the map. The segmentation parameters are listed in Table 4.10. (Image obtained using AFM Park)

Table 4.10: Segmentation parameters values used for the grain analysis of ZnS_60. The parameters description is reported in Section 3.2.5, Chapter 3.

Parameters	**GS**	**AG**	**AC**	**BL**	**PL**	**PFM**
Set Value	2.93 px	28.4 %	11.11 %	100.00 %	0.00 %	2.29 %

4.3.4 150 W - ZnS_53

The results reported in Table 4.12 show that the values of R_{HHCF} and $R*$ differ to each other more than the standard error. This is due to the non-optimal fit of the self-affine function for the *HHCF* data, which is shown in Figure 4.18. The main reason for this is that the sample, as described in Section 4.1, possesses a non-uniform surface profile, with regions where the last epitaxial layer is totally absent. In addition, the sample shows the largest mean dip number and size, as found in Section 4.2, which contributes to the non-uniformity of the surface.

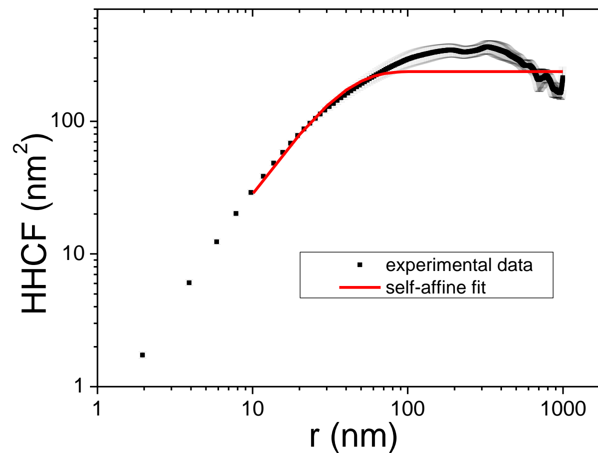

Figure 4.18: Graph showing the *HHCF* experimental data (*black dots*) as a function of the lateral separation of surface heights in logarithmic scale for ZnS_53. *HHCF* has been fitted by the self-affine function (*red line*). Parameters extrapolated from the fit have been reported in Table 4.12.

Table 4.12: Mean values of parameters for ZnS_53. R_{HHCF}, ξ and α evaluated from self-affine fitting of *HHCF* data. $R*$ evaluated by averaging over all maps.

Parameters	Value
R_{HHCF} **(nm)**	3.44 ± 0.02
ξ **(nm)**	34 ± 1
α	0.83 ± 0.02
$R*$ **(nm)**	3.09 ± 0.02

From the image segmentation depicted in Figure 4.20, the grain arrangement results in a good match with the mask. From the experimental results reported in Table 4.14,

the GN value is shown to be the smallest over the ZnS samples. The MDR value is about the same of that of the 50 W sample (ZnS_35), and it is shown to be lower than the lateral correlation length. From the experimental results, the sample shows a low density of grains on the surface, which possesses a non-uniform structure. This non-uniformity lead to a large surface roughness for the sample, also shown by the values of R_{HHCF} and α reported in Table 4.12.

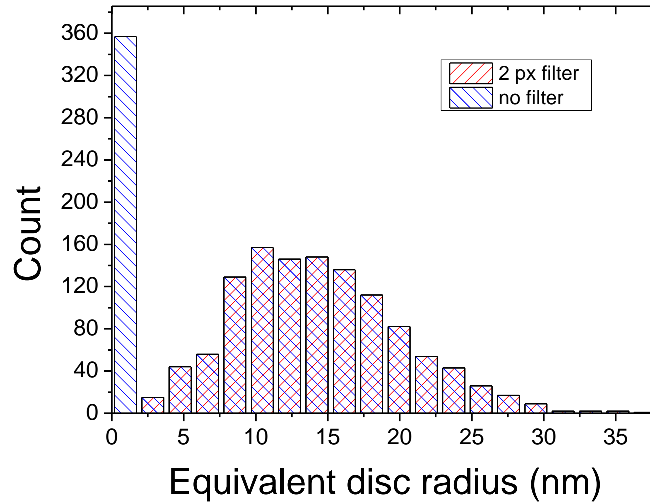

Figure 4.19: Equivalent disc radius distribution of the grains with the application of the 2 px^2 filter (*red*) and without (*blue*) for ZnS_53. The MDR has been calculated by averaging the distribution without the contribution of grains with an area smaller than 2 px^2 (represented by the blue column on the left of the histogram), which would have led to an incorrect evaluation of the parameter.

Table 4.14: Grain number and equivalent disc radius results for ZnS_53. MDR has been calculated by the equivalent disc radius distribution shown in Figure 4.21.

Parameters	Value
GN	1110
MDR (nm)	14.4 ± 0.2

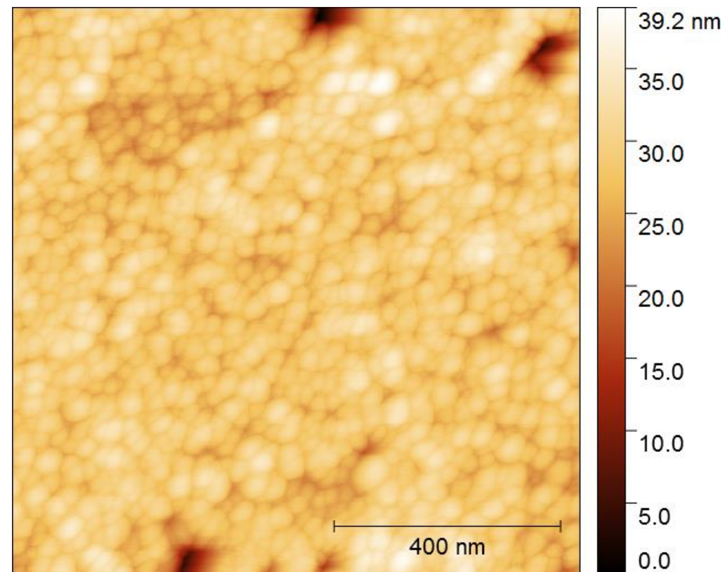

(a)

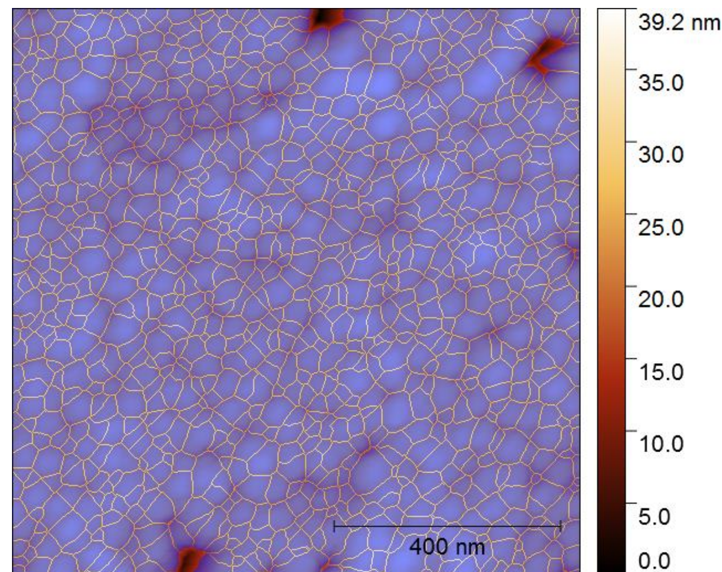

(b)

Figure 4.20: Image segmentation of the ZnS_60 1μm × 1μm map for the evaluation of the GN and EDR. *(a)* Height topography map acquired in non-contact mode; *(b)* Application of the segmentation mask on the map. The segmentation parameters are listed in Table 4.13. (Image obtained using AFM Park

Table 4.13: Segmentation parameters values used for the grain analysis of ZnS_53. The parameters description is reported in Section 3.2.5, Chapter 3.

Parameters	**GS**	**AG**	**AC**	**BL**	**PL**	**PFM**
Set Value	5.00 px	0.00 %	49.01 %	55.02 %	0.00 %	3.70 %

4.3.5 Choice of segmentation parameters

The image segmentation method has been used in order to extract the grain properties as the GN and the EDR distribution for each sample. As described in Chapter 3, a correct segmentation mask must be applied on each map, which means a correct choice of the segmentation parameters. This choice has been done to yield the better match between the applied mask and the grain arrangement for the samples. However, little changes of the segmentation parameters correspond to variations of the experimental results that can affect the analysis. To understand how large these variations are, the segmentation parameters of the maps have been modified with respect to the optimum choice and the resulting values of grain number (GN) and mean grain size (MGS) have been reported. The MGS value is a grain size parameter calculated by Gwyddion that approximates a grain to a square and measure its side, while the equivalent disc radius (EDR) is the radius of a disc that possesses the same grain projected area. Variations of GN and MGS have resulted about the same for different samples. An exemplificative view of segmentation parameter variations with the relative GN and MGS values measured for the ZnS_35 sample have been reported in the graphs of Figure 4.21.

The more sensitive segmentation parameters are the Gaussian smoothing (GS) and the prefill from minima (PFM), depicted respectively in Figure 4.21 *(a)* and *(f)*. Little variations of these two parameters correspond to considerable changes in the final GN value. For this reason, the choice of GS and PFM have been the most important during the grain analysis. The barrier level (BL) shows also changes in the final result, but in a less crucial way respect to the GS and PFM. At last, the add curvature (AC), add gradient (AG) and prefill level (PL) parameter variations show the smallest change in the final GN value.

Basing on these considerations, it can be concluded that the grain analysis done using the image segmentation method is stable, since even small variations of the chosen segmentation parameters do not compromise significantly the final results.

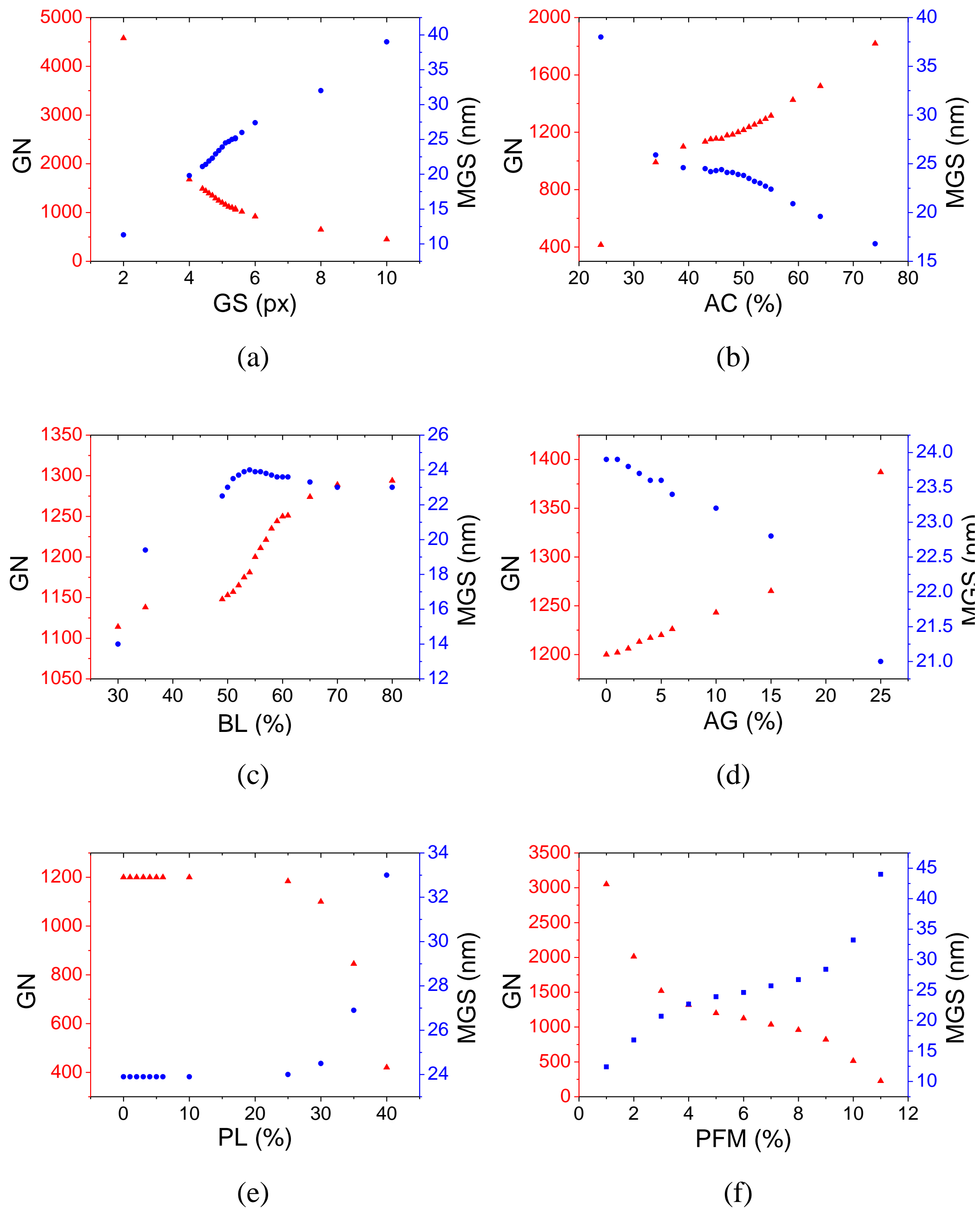

Figure 4.21: GN (*red triangles*) and MGS (*blue circles*) variations for ZnS_35 corresponding to changes in the segmentation parameters used: *(a)* Gaussian smoothing; *(b)* Add curvature; *(c)* Barrier level; *(d)* Add gradient; *(e)* Prefill level; *(f)* Prefill from minima;

4.3.6 Sputtering power dependence of the results

The experimental results from the structural analysis are reported in the graphs depicted in Figure 4.22. From the experimental results a non-linear dependence of the parameters on the sputtering deposition power (SDP) is shown. The SDP at which the films are grown affects in a crucial way the surface structure of the samples under investigation, but the main parameters do not vary with a linear proportionality with it. The graph in Figure 4.22 *(a)* shows the average roughness (R^*) to increase with the SDP except from 50 W. Figure 4.22 *(b)* also shows a similar trend for the lateral correlation length (ξ) as a function of the SDP. The results of the roughness exponent α show an inverse plot respect to R^*, where at 50 W corresponds the lowest value and at 75 W the largest among the samples, as visible from Figure 4.22 *(c).* At 75 W the MDR results to be the smallest among the samples, where the largest corresponds to 125 W, as it can be seen in Figure 4.22 *(d).* It can be concluded that ZnS thin films grown at a 75 W possess the lowest surface roughness, with very small grains that tend not to form clusters. Higher SDP lead to a larger roughness and MDR that is correlated to the greater presence of dips.

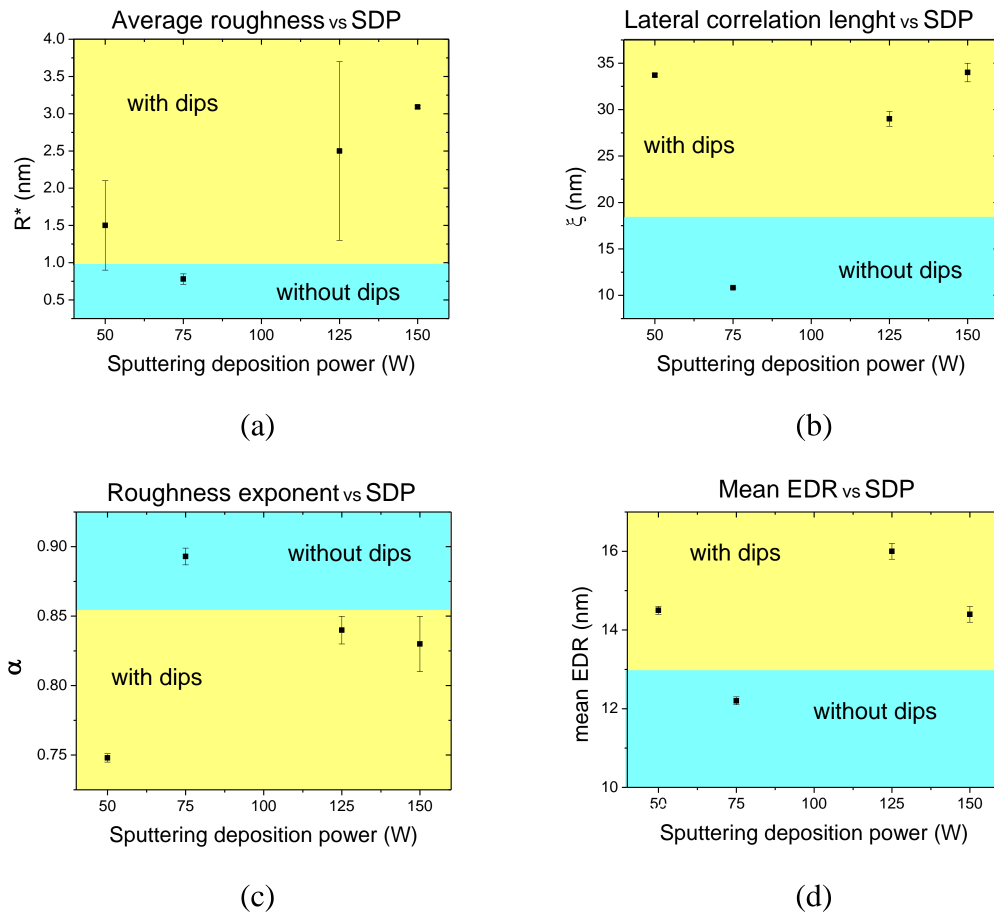

(a) (b)

(c) (d)

Figure 4.22: Graphs of the main experimental results from the structural and grain analyses of the ZnS as a function of SDP. The two colored regions of the graphs differentiate results of samples with the presence of dips (*light blue*) from those without the presence of dips (*yellow*). Parameters shown in the graphs: *(a)* Average surface roughness R^*; *(b)* Lateral correlation length ξ; *(c)* Roughness exponent α; *(d)* Mean grain equivalent disc radius (MDR).

4.4 Comparison with ZnO

Experimental results for both ZnS and ZnO samples have been reported and discussed in this section in order to compare structural and grain properties of the ZnS thin films with those of another Zn compound: ZnO. In the first part of this section are reported the results from the analyses of the two samples ZnO 96 and 97. As for the ZnS films in Section 4.3, a brief discussion about the main results has been done for each sample. The analyses on the ZnO have been the same performed on the ZnS samples, meaning structural parameters extracted from self-affine fit of the *HHCF* data and grain properties calculated by using image segmentation of the AFM maps. The *HHCF* data have been extracted from five different 1µm × 1µm maps for each sample, and then averaged by rows to obtain the distributions from which the parameters have been evaluated. The grain parameters GN and MDR have been extracted by the image segmentation with the application of the 2 px^2 threshold filter. Both the *HHCF* graphs with the self-affine fit and the EDR grain distribution histograms for the ZnO samples have been reported in this section. In the last part of this section the main experimental results for both the ZnS and ZnO samples have been reported and discussed in comparison.

4.4.1 ZnO - Structural and grain analyses results

Experimental results of the roughness exponent α and average roughness R^* from the structural analysis of the ZnO samples are reported in Table 4.15. Surface roughness R_{HHCF}, lateral correlation length ξ, GN and MDR will be reported and discussed in comparison with those of the ZnS samples in Subsection 4.4.2. The image segmentation process is shown in Figure 4.23, with the segmentation parameters used reported in Table 4.16. The *HHCF* data and the EDR grain distributions are shown in Figure 4.24 and 4.25, respectively.

Table 4.15: Mean values of the roughness exponent α, average roughness R^* and AR_{sq} of the self-affine fit for ZnO 96 and 97.

Parameters	ZnO_96	ZnO_97
$\boldsymbol{\alpha}$	1.00 ± 0.05	1.00 ± 0.05
R^* (nm)	7.5 ± 0.8	11.1 ± 0.2

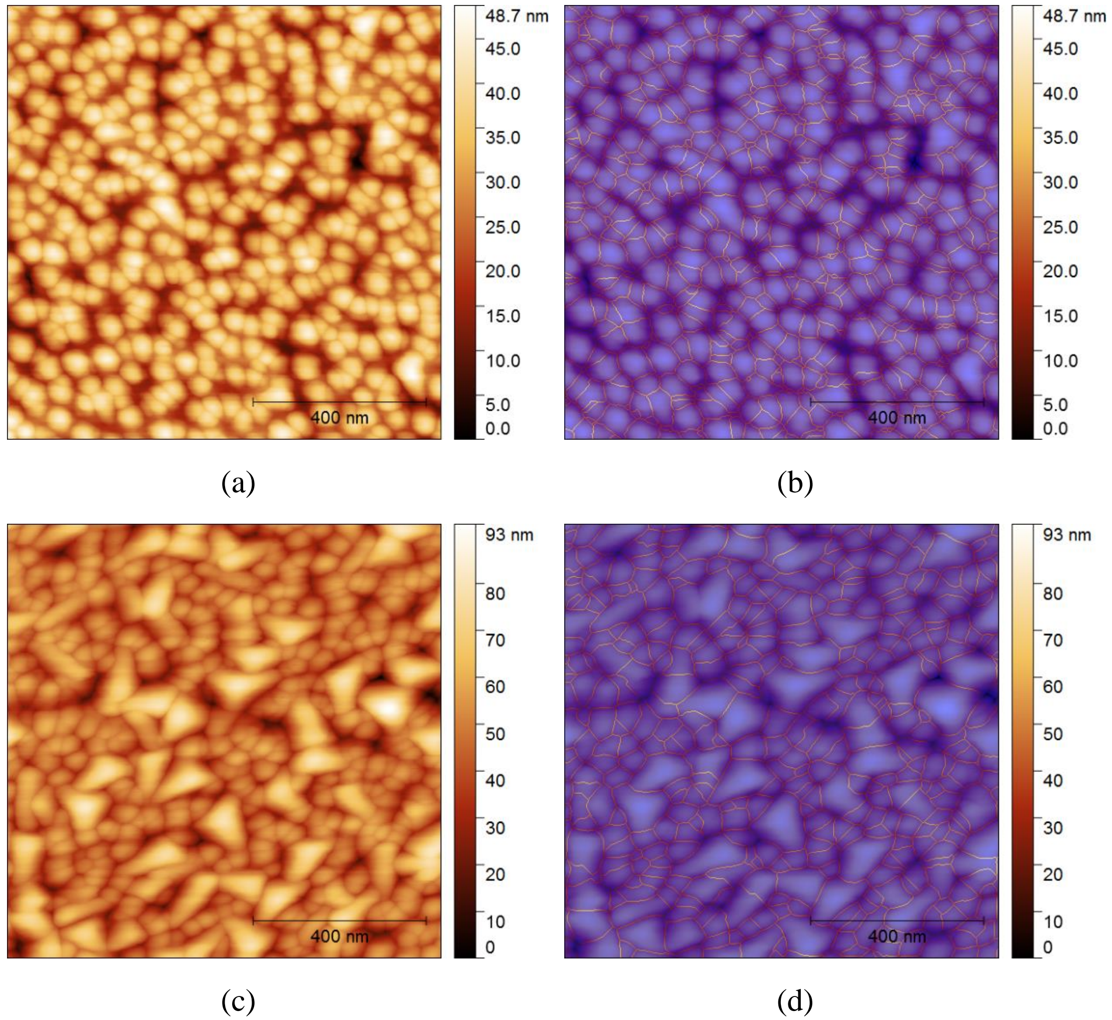

Figure 4.23: Image segmentation of the 1µm × 1µm maps for the evaluation of the GN and EDR. *(a)* Height topography of ZnO_96; *(b)* Segmentation of the ZnO_96 map; *(c)* Height topography of ZnO_97; *(b)* Segmentation of the ZnO_97 map. The segmentation parameters used are listed in Table 4.16. (Image obtained using AFM Park in non-contact mode)

Table 4.16: Segmentation parameters used for the ZnO samples.

Parameters	GS	AG	AC	BL	PL	PFM
ZnO_96	2.07 px	13.58 %	13.58 %	100.00 %	19.75 %	2.58 %
ZnO_97	5.64 px	14.81 %	28.40 %	92.59 %	17.28 %	2.47 %

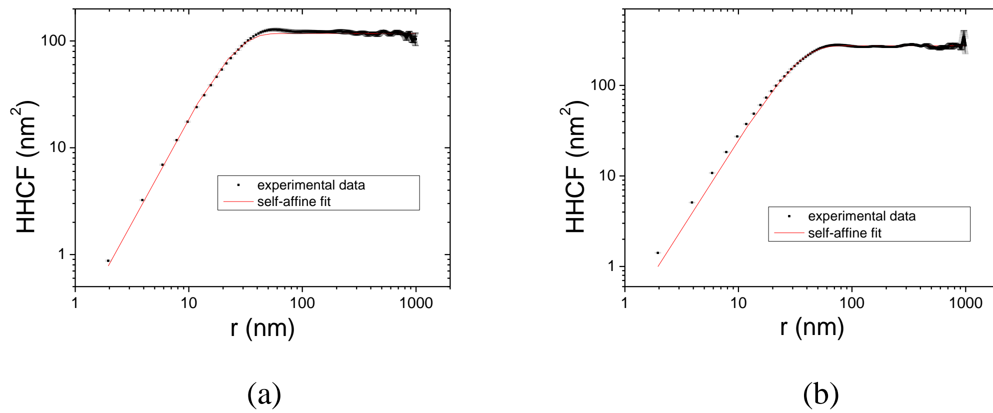

Figure 4.24: Experimental *HHCF* data (*black dots*) in function of the lateral separation of surface heights in logarithmic scale for: *(a)* ZnO_96 (AR_{sq} = 0.8743); *(b)* ZnO_97 (AR_{sq} = 0.8706); *HHCF* data have been fitted by the self-affine function (*red line*). The parameters extracted from the self -affine fit have been reported in Table 4.15.

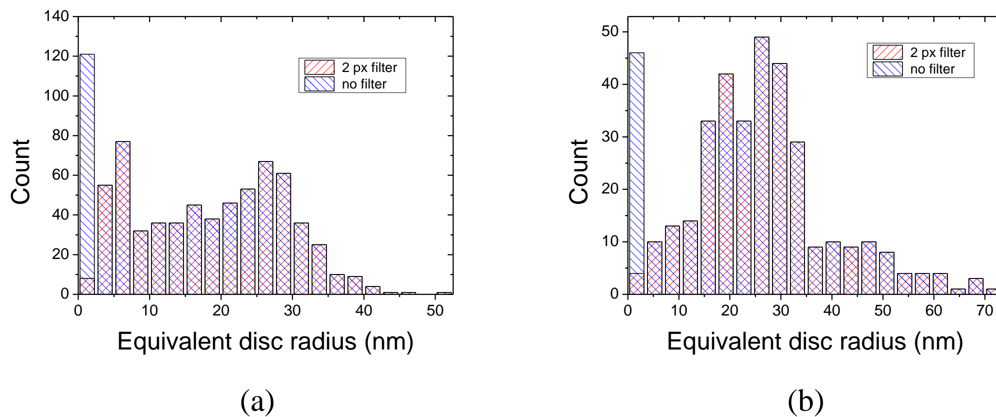

Figure 4.25: Equivalent disc radius distribution of the grains with the application of the 2 px^2 filter (*red*) and without (*blue*) for ZnO_96 *(a)* and ZnO_97 *(b)*. The MDR has been calculated by averaging the distribution without the contribution of grains with an area smaller than 2 px^2 (represented by the blue column on the left of the histogram), which would have led to an incorrect evaluation of the parameter.

4.4.2 Results comparison and discussion

The experimental results obtained both for the ZnS and the ZnO samples are reported in Table 4.17. The comparison between the two sets has been done for the four main parameters of the analysis: mean surface roughness R_{HHCF}, mean lateral correlation length ξ, grain number (GN) and mean equivalent disc radius (MDR).

Table 4.17: Experimental results of structural and grain parameters for both the ZnS and ZnO samples to do a comparison.

Sample (SDP)	ZnS_35 (50 W)	ZnS_36 (75 W)	ZnS_60 (125 W)	ZnS_53 (150 W)	ZnO_96	ZnO_97
R_{HHCF} (nm)	1.67	0.79	2.58	3.44	7.66	11.70
ξ (nm)	33.7	10.8	29.0	34.0	23.9	32.3
GN	1200	1630	1200	1110	780	380
MDR (nm)	14.5	12.2	16.0	14.4	18.0	27.0

The mean surface roughness R_{HHCF} of the ZnO thin films results much larger than that of the ZnS. This can be viewed from the three-dimensional profiles depicted in Figure 4.4 *(a)* and *(b)* (Section 4.1). The surface of the ZnO results very rough, due to the presence of tall clusters that are large in size. In fact, the MDR values for the ZnO samples are also the largest measured in the analysis. From these considerations, the surface of the ZnS films possesses a very low roughness compared to ZnO, with a maximum exhibited by the 150 W sample (ZnS_53), which is less than a half of those of the ZnO. For the flattest of the ZnS samples, which is the 75 W (ZnS_36), the surface mean roughness R_{HHCF} is a tenth of that of ZnO_96 and a sixteenth of that of ZnO_97, meaning a surface that is ten and sixteen times smoother, respectively. The lateral correlation length for ZnO results about of the same order of the ZnS (apart from ZnS_36). However, the MDR is considerably larger for the ZnO samples. This means that grain clusters will tend to form mostly on the ZnS surface than the ZnO, since the ZnO samples show the lower ξ to MDR ratio. This can also be viewed from the images reported in Figure 4.1 and 4.2 (Section 4.1), where the presence of grain clusters is visible. Nevertheless, this is not true for the 75 W sample (ZnS_36), being the one with the lowest MDR and ξ. From the grain analysis results, a small value of the GN is shown by the ZnO films. In particular, ZnO_97 shows a GN that is one quarter of that of ZnS_36. From this values it can be deduced that the ZnS films exhibit a very higher amount of grains on the surface. From the values reported in Table 4.17 it results an inverse proportionality between the GN and the surface roughness, which means a sample with a large GN possesses a low mean roughness, and vice versa. From the results, it can be concluded that the ZnS thin film grown at a 75 W shows the flatter surface profile, where the presence of grain clusters (and dips) is near absent.

4.5 Electrostatic characterization results

In this section the experimental results from the electrostatic characterization of the 75 W sample (ZnS_36) are reported. The motivation behind the choice of this sample comes from the morphological analyses: it has been shown from the dip and grain analyses that ZnS thin films grown at a 75 W possess the flattest surface profile, meaning the smallest roughness and presence of dips. Starting from these results, the 75 W sample has been chosen to be investigated by the EFM and KPFM techniques because it exhibits a uniform surface profile. The EFM measurements have been performed using AFM Park, in order to get the contact potential (CP) maps that characterize the electrostatic structure of the surface. In addition, the KPFM analysis has been used to obtain an evaluation of the contact potential difference (CPD) between the ZnS and the Al layer deposited for the sheet resistance measurement. At last, by using a four-probe points method, the sheet resistance of the sample has been evaluated yielding a result that will probe to be an inferior limit and not a final value. In Subsection 4.5.1, the main EFM and KPFM maps have been reported and discussed. The CPD results between ZnS and Al have been reported in Subsection 4.5.2. At last, the sheet resistance experimental result has been discussed in Subsection 4.5.3.

4.5.1 EFM surface topography

The contact potential maps reported in this subsection have been obtained by using non-contact EFM Park in constant height mode. A first scan has been performed in order to obtain a morphological map of the sample surface. Then, a second scan with a conductive tip has been done to get a contact potential topography. Four maps 500nm $\times$ 500nm of sample ZnS_36 have been obtained during the analysis, using a resolution of 256×256 px^2. The more exemplificative EFM contact potential and height topographies maps have been reported in Figure 4.26.

A match between the electrostatic and the height topographies of the surface can be observed in the images. From the AFM result, it can be deduced that the local charge density is distributed depending on the surface morphology. This means that the local slope of the surface profile affects directly the charge accumulation. From the images depicted in Figure 4.26 *(a),* it is visible that the contact potential is larger in regions associated to valleys and lower in regions associated to peaks. This means that charge density tends to accumulate in concave spaces. This is also partially visible in the second map shown in Figure 4.26 *(b)*. Therefore, the contact potential profile for the ZnS thin film varies inversely with the height topography, where height maxima correspond to potential minima and vice versa.

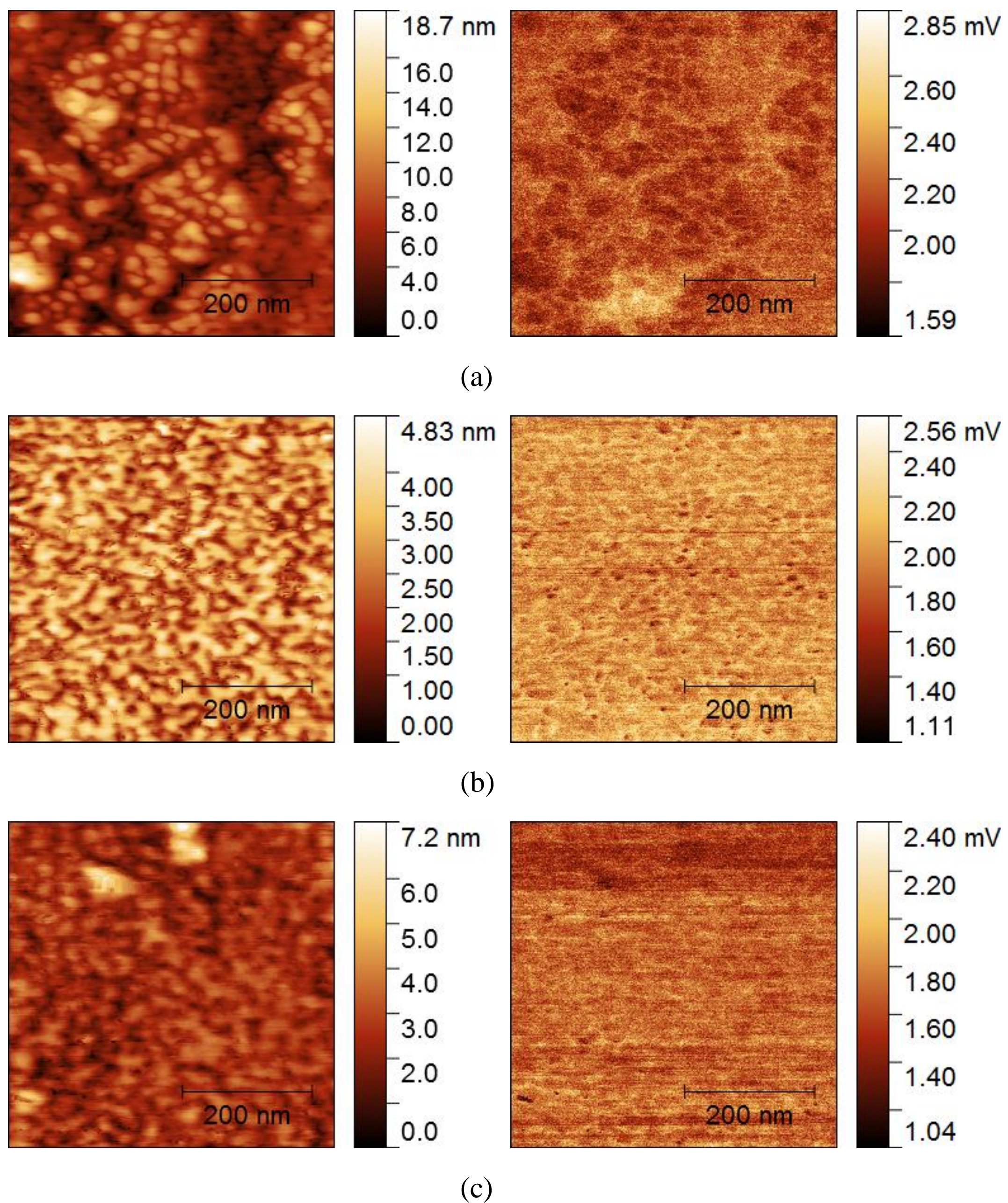

Figure 4.26: EFM surface characterization of the 75 W sample ZnS_36, where the height topography map (*left*) and contact potential map (*right*) are displayed: *(a)* Map 1 (*Amplitude = 27 nm; Scan rate = 0.2 Hz*); *(b)* Map 2 (*Amplitude = 24.7 nm; Scan rate = 0.2 Hz)*; *(c)* Map 3 (*Amplitude = 29.6 nm; Scan rate = 0.25 Hz)*;

4.5.2 Sheet resistance result

The four-probe points measurement performed on the 75 W sample confirm that the ZnS sample acts as an insulator. From the measurement, a precise value of the sheet resistance has not been obtained. The motivation of this lies in a too high resistance that went beyond the instrument sensibility. However, an inferior limit of 7 GΩ has been reported for the 75 W ZnS film. This result proves the ZnS film effectively as an insulator.

4.5.3 ZnS - Al Contact potential difference

The 75 W sample has been investigated using KPFM technique in order to measure the CPD between the Al and ZnS layers. The KPFM potential map resulting from the analysis is depicted in Figure 4.27, where the dark region on the left corresponds to the Al layer, while the light region on the right to the ZnS layer. The image has been cut to point out the potential step between the two deposited layers.

The measurement of the CPD between the two materials, corresponding to the measurement of the difference between the work function of the Al and the electron affinity of the ZnS sample, has been done by averaging the CP values extracted from two separated regions of the map. The results of the measurement are reported in Table 4.18.

Table 4.18: CPD mean values for the ZnS and Al layers.

Layer	ZnS	Al
CP (V)	0.045 ± 0.002	0.020 ± 0.001

From the measurements, the CPD value between ZnS and Al results 0.02 V (with an error of 10^{-3} V). The known value of the work function of Al is about 4.08 eV [83], while the bulk electron affinity value of ZnS has range of values between 3.8 to 3.9 eV [84]. However, from the experimental data it results that the CPD obtained is about an order of magnitude smaller than the reference value. The motivation behind this result could lies in several effects that can act on the surface. A decrease in the measured CP can be explained by induced-surface states originating from oxide formation [85]. The presence of positive and negative charges trapped in oxide (e.g. SiO_2 and Al_2O_3 films grown on a Si substrate) have been experimentally observed by Ludeke et al. [85]. The trapped charge appears as dark spots for negative charges under negative substrate bias and positive charge for positive bias in potential images measured by KPFM [85]. The non-uniform profile of the contact potential, as visible in Figure 4.27, meaning the dense-packed presence of maxima and minima, could reflect trapped charge effects on

the surface. Therefore, being the experimental CPD calculated by averaging values on regions with a large non-uniform profile, the final result could be smaller than the real CPD between the ZnS and the Al layers. A second measurement of the CPD performed considering only values on the maxima and minima of the map has yielded to an approximated CPD of 0.12 V. This can be viewed in a qualitative way from the three-dimensional profile depicted in Figure 4.27.

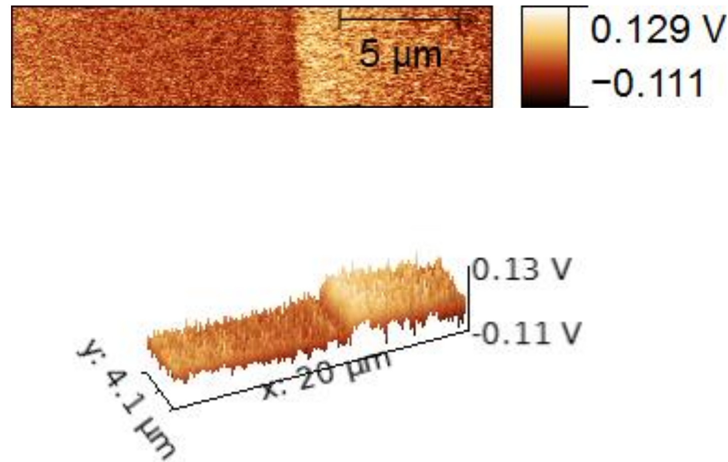

Figure 4.27: KPFM contact potential map in the step between the Al (*dark region on the left*) and ZnS (*light region on the right*) layers. From the three-dimensional profile is visible a CPD of about 0.12 V that corresponds to the difference between the electron affinity of ZnS and the work function of Al. The CPD value averaged over the two regions results of 0.02 V.

From the experimental results, it can be concluded that the average CPD value is not concordant with the values known from literature. However, this could be due to induced-surface states originating from oxide formation. Nevertheless, a measure of the CPD considering only the difference between maxima and minima of the two CP values yields a CPD of about 0.12 V.

4.6 Discussion

The morphological characterization of ZnS thin films grown at different sputtering deposition power was performed by several steps. At first, the presence of dips, which is related to the quality of the films for photovoltaic applications, was investigated in order to delineate the sputtering power at which the lowest density of dips is obtained. In the employed technique, a crucial role was played by the height threshold value chosen to define a dip, namely z_{segm}. From the calculations, the dip number variation corresponding to little changes in the height threshold resulted of about 3 – 15 %. From the results it was immediate to identify the sputtering power at which the lowest presence of dips was exhibited, namely 75 W. This was also confirmed by further analyses performed on a second set of ZnS thin films grown at 75 W that showed a total absence of dips. It was concluded that the dip density is affected by the sputtering deposition power without a linear dependence, since a non-linear trend was observed.

Then, the structural properties of the ZnS thin films were investigated by using a statistical method to calculate the main parameters associated to the surface structure. The analysis was carried out assuming the surface to be self-affine, which allows to fit the height-height correlation data extracted by the software Gwyddion for each map and extrapolate the parameters from the self-affine fit, namely the surface roughness R_{HHCF}, the lateral correlation length ξ and the roughness exponent α. In addition, the mean number and size of the grains were evaluated by the image segmentation method. This analysis included the correct choice of the parameters used during the segmentation, which was done to obtain the better match between the applied mask and the grain arrangement for the samples. The parameters that mostly affect the final results were shown to be the Gaussian smoothing and the prefill from minima.

The analyses were performed also on two ZnO thin films in order to get a comparison of the structural properties between the two zinc compounds. From the experimental results, it is possible to conclude that the sputtering power strongly affects the surface morphology but in a non-linear way. The mean surface roughness R_{HHCF} of the ZnS samples resulted in the range 0.8 – 3.44 nm, which is much lower than that of ZnO, which is in the range 7.6 – 11.7 nm. The mean grain number was shown to be much larger for the ZnS films (1100 – 1600 μm^{-2}) than that of ZnO (380 – 780 μm^{-2}). Moreover, the mean grain equivalent radius of the ZnS films was calculated in the range 12 – 16 nm, while that of ZnO resulted of 18 – 27 nm. These results showed that the ZnS thin films to have a larger number of grains that are smaller in size respect to ZnO, and a surface roughness which is much lower. The surface profile of the ZnS films resulted flatter than the ZnO. In some of the analyzed samples the lateral correlation length ξ is greater than the dimension of the grains, evidencing that a clustering of the grains is present. This was not observed for the ZnS sample grown at a 75 W sputtering power, in which ξ resulted lower than the mean grain size. Clustering of the grains due to the sputtering deposition also contributes to the variations observed in the density of dips, meaning the lower clustering corresponds to the lower presence of dips. Also in

this case, the lowest values for the structural parameters were observed for the dip-free ZnS sample grown at 75 W. The low density of dips of the sample deposited at 75 W can be related to this low deposition power. At higher power, clustering effects could lead to a decrease in the homogeneity of the surface, on the contrary a lower deposition power could lead to a non-complete surface coverage, and thus to an increase of the dip density.

At last, the electrical properties of the flattest ZnS thin film, meaning the one exhibiting the lowest roughness and presence of dips, were investigated by means of EFM and KPFM techniques. In order to measure the sheet resistance with a four-point probes method, four Al channels were deposited on the surface of the 75 W ZnS thin film by thermal evaporation. The EFM contact potential maps were obtained to get the electrostatic characterization of the surface and to have an evaluation of the potential difference between the ZnS and the Al layer, corresponding to the difference between the Al work function and the ZnS electron affinity. A match between the electrostatic and the height topographies of the ZnS sample surface was found from the EFM maps. This could be due to a direct morphological dependence of the local charge distribution. It was observed that the contact potential is larger in regions associated to valleys and lower in regions associated to peaks. Therefore, the local charge density tends to accumulate in concave areas.

The contact potential difference between the ZnS and the Al layer was obtained by using KPFM technique to get more precise measurements. The experimental result was found to be one order of magnitude smaller than the reference value known from literature. This could be related to presence of induced-surface states originating from oxide formation. Positive and negative charges trapped in oxide has already been observed in previous studies [85]. The main consequence of these trapped charges is the very non-uniform profile of the contact potential map, with a dense-packed arrangement of maxima and minima that leads to an underestimation of the real potential difference. A second measurement was performed by considering only values on the maxima and minima of the map, yielding a result close to the value known from literature. Finally, the resistance of the sample was measured to be beyond the instrument sensibility, with an inferior limit of 7 GΩ, thus leading to the conclusion that the ZnS film totally acts as an insulator.

Conclusions

The aim of this thesis is the morphological and electrical characterization of zinc sulfide (ZnS) thin films in dependence of the sputtering deposition power by using Atomic Force Microscopy (AFM) and Kelvin Probe Force Microscopy (KPFM) techniques.

This work has been developed in the framework of the worldwide energy problem of the 21st century. To stop the global warming related to the use of fossil fuels and to fill the gap due to the increasing global energy demand, the development of renewable sources of energy is of fundamental importance. Photovoltaics (PV) is one of the most promising and interesting source of renewable power. Today, over the 85 % of the whole PV market is dominated by monocrystalline and polycristalline silicon wafer based solar cells, which require high wafer thickness (~300 µm). For this reason, costs associated to silicon wafer cells have low possibility to be reduced in a future prospect. For a large scale use of the PV resources, it is crucial to improve new technologies aimed to increase the cells performance while lowering the costs. A promising alternative is represented by the thin film solar cells, which require cheaper materials and smaller thickness, with wider possibilities to improve the efficiency while keeping the costs low. These devices are made of several thin layers of different materials, with various alternatives for the absorber material, including amorphous silicon (a-Si), CdTe and $CuInGaSe_2$ (CIGS).

In this context, a fundamental role is played by the passivating layers, in order to diminish the surface states that act as recombination centers. It has been already proved by previous studies [4,33,86,34], that placing a buffer layer with a larger energy gap between the metal contacts and the active material results in the open circuit voltage to increase and higher efficiency to be reached with lower costs. Actually, among various suitable materials, CdS has been the most common semiconductor used as a buffer layer for surface passivation for CIGS solar cells. However, the use of Cd is associated to toxic hazards, thus leading the attention to new environmental-friendly materials. One of the most promising candidates among various alternative materials is ZnS, since it is non-toxic, abundant and cheaper [49]. In addition, ZnS has a direct wide energy gap of 3.5 – 3.9 eV at room temperature, that is larger compared to CdS having an energy gap of

2.45 eV [49]. ZnS thin films are promising as surface passivation layers because of their high transmittance, wide energy gap and insulating properties. Due to its low reflectivity, ZnS thin films could also find applications as antireflection coatings, which are essential part of the solar cells [45]. This material exhibits peculiar properties that have not yet been much investigated. ZnS thin films have been found useful in various devices, covering a wide area of applications, including electroluminescent devices, photosynthetic coating and optoelectronic devices such as blue light emitting diode [7]. For the interesting properties of ZnS thin layers, in particular focusing on PV applications, a morphological and electrical characterization of ZnS thin films has been performed, with the aim of pointing out the connection between the deposition conditions (i.e. the sputtering deposition power) and the properties of the material at the nano-scale.

The ZnS thin films studied in this thesis are deposited by DC sputtering at the Department of Materials Sciences of the University of Milano Bicocca (UNIMIB). The deposition was performed using Argon as inert gas; the sputtering power has been varied in the range 50 – 150 W; the ZnS samples have been grown on a soda-lime glass substrate hold from fixed distance of 6 cm from the target.

AFM morphology analyses showed the presence of dips on the sample surfaces. The sputtering deposition power corresponding to the lowest dip density was determined. The presence of dips, which is related to the quality of the films for PV applications, was investigated in order to define the sputtering power corresponding to the lowest density of dips. In the analyses of AFM morphological maps, a fundamental role was played by the height threshold value chosen to define a dip. After the analysis, the variation of the grain parameters as a function of the height threshold was calculated to be in the range 3 – 15 %.

The structural properties of the ZnS thin films were investigated by means a statistical method to calculate the main parameters associated to the surface structure, namely the surface roughness, the lateral correlation length and the roughness exponent. In addition, the mean number and size of the grains were calculated by the image segmentation method. Through this technique, it is possible to mark the grains on the map, extracting their number and the equivalent disc radius distribution, from which the mean grain radius was evaluated for each sample. The analyses were performed for another zinc compound, ZnO, in order to get a comparison between the structural and grain properties.

Furthermore, the electrical properties of the flattest ZnS sample, meaning the one exhibiting the lowest roughness and presence of dips, were investigated at the nano-scale by using EFM and KPFM techniques. Four Al layers have been deposited on the sample surface by thermal evaporation in order to measure the sheet resistance of the sample using a four-point probes method. At last, the contact potential difference between the ZnS and the Al layer, corresponding to the difference between the Al work function and the ZnS electron affinity, was evaluated from the KPFM maps. From the experimental results, the conclusions are the following ones.

The sputtering deposition power strongly affects the morphology of the samples. The sample grown at 75 W sputtering power shows the lowest density of dips, while the samples with the lowest and highest sputtering power, namely 50 W and 150 W, both show a large density of dips.

The structural and grain parameters also show a non-linear dependence on the sputtering power. The 75 W sample results the one with the lowest roughness and the highest density of grains. The reduced dimensions of grains could be related to the low density of dips and hence to the larger uniformity of the sample surface. Apart from the 75 W sample, the presence of dips is observed in the ZnS films jointly with a grain clustering process, which is shown also by the larger value of the lateral correlation length respect to the mean grain radius.

From the comparison with ZnO, the surface roughness of ZnS samples results much lower, meaning a smoother surface profile. Moreover, the ZnS grain arrangement shows a higher number of grains that are smaller in size.

A match between the electrostatic and the height topographies of the sample surface was found from the EFM maps. This could be related to a direct morphological dependence of the local charge distribution, meaning that the charge density tends to accumulate in concave areas. The measurement of the sheet resistance proved that the ZnS film acts as an insulator. Finally, the contact potential difference between the ZnS and the Al layer resulted underestimated with respect to the value known from literature. This could be due to the presence of induced-surface states originating from oxide formation, which has already been observed by previous studies [85].

The morphological and electrical properties studied in this thesis provide a thorough characterization of the ZnS thin films, with a particular care for the best sputtering deposition power to be used for photovoltaic applications, especially with a focus on thin film solar cells technology. With a direct wide energy gap, high transmittance and insulating properties, ZnS thin layers are expected to play a key role on developing new photovoltaic solar cells and creating non-toxic and cheap renewable energy.

Acknowledgements

This thesis would not have been possible without the help of many individuals who have greatly assisted me during this study.

First, I want to express my appreciation and thanks to Prof. Daniela Cavalcoli, for her knowledge, encouragement and patience.

A special thanks to Dr. Martina Perani, who has guided me in this work step by step, teaching me an enormous amount of matters with her kindness and experience.

A particular thanks is deserved to the Department of Materials Sciences of University of Milano Bicocca and to the Photovoltaic Division of the Department of Physics of University of Konstanz for the preparation of the samples that I studied.

I would like to thank my friends, near and far who are, to be always an easier and fun part of my life.

Last but not least, I want to express my deepest gratitude to my family, for supporting me during these years and for allowing me to degree in physics, this would not be possible without their help.

Bibliography

1. Zeman M. 'Introduction to Photovoltaic Solar Energy'. Delft University of Technology, college material, 2012: http://aerostudents.com/files/solarCells/solarCellsTheoryFullVersion.pdf.
2. EIA annual energy outlook 2015: http://www.eia.gov/forecasts/aeo/pdf/0383%282015%29.pdf.
3. Wolden C. A., Kurtin J., Baxter J. B., Repins I., Shaheen S. E., Torvik J. T. 'Photovoltaic manufacturing: Present status, future prospects, and research needs.' Journal of Vacuum Science & Technology A 29.3 030801. (2011).
4. Kibbler A. E. 'Passivation of interfaces in high-efficiency photovoltaic devices.' Compound semiconductor surface passivation and novel device processing: symposium held April 5-7, 1999, San Francisco, California, USA. Vol. 573. Materials Research Society, (1999).
5. Nguyen, M., Ernits, K., Tai, K. F., Ng, C. F., Pramana, S. S., Sasangka, W. A. 'ZnS buffer layer for Cu 2 ZnSn (SSe) 4 monograin layer solar cell.' Solar Energy 111 344-349. (2015).
6. Sambhu K., Olsen L. C.. 'Chemical bath deposited (CBD) ZnS buffer layer for CIGSS solar cells.' Photovoltaic Specialists Conference, 2002. Conference Record of the Twenty-Ninth IEEE. IEEE (2002).
7. Ibiyemi A. A., Tech M., Awodugba A. O. 'The influence of annealing on electrical and optical properties of ZnS thin film'. The Pacific Journal of Science and Technology, 13(1) (2012).

8. IEA global tracking framework: https://www.iea.org/media/freepublications/oneoff/GlobalTrackingFrameworkOverview.pdf.
9. Hubbert M. K. 'Nuclear Energy and the Fossil Fuels. Drilling and Production Practice'. American Petroleum Institute & Shell Development Co. Publication No.95 (1956).
10. Hirsch, R. L., Bezdek R., Wendling R. 'Peaking of world oil production: impact, mitigation, & risk management. 2005.' US Energy Information Administration, Annual Oil Market Chronology, at http://www. eia. doe. gov/emeu/cabs/AOMC/Overview. html 26. (2004).
11. BP outlook to 2035: http://www.bp.com/en/global/corporate/energy-economics/energy-outlook-2035/energy-outlook-to-2035.html.
12. European Environment Agency: http://www.eea.europa.eu/.
13. NASA climate change: http://climate.nasa.gov/.
14. NASA climate change: http://earthobservatory.nasa.gov/Features/GlobalWarming/.
15. IPCC, 2007: Summary for Policymakers. In: Climate Change 2007: The Physical Science Basis. Contribution of Working Group I to the Fourth Assessment Report of the Intergovernmental Panel on Climate Change [Solomon, S., D. Qin, M. Manning, Z. Chen, M. Marquis, K.B. Averyt, M.Tignor and H.L. Miller (eds.)]. Cambridge University Press, Cambridge, United Kingdom and New York, NY, USA.

16. Shell energy outlook to 2050: http://www.shell.com/content/dam/shell/static/public/downloads/brochures/corporate-pkg/scenarios/shell-energy-scenarios2050.pdf.

17. IEA renewable energy: http://www.iea.org/aboutus/faqs/renewableenergy/.

18. Beck F., Martinot E.. ‘Renewable energy policies and barriers.’ Encyclopedia of energy 5.7 365-383. (2004).

19. NREL energy analysis: http://www.nrel.gov/analysis/news/news_archive2012.html.

20. Fraunhofer Photovoltaic Report: https://www.ise.fraunhofer.de/de/downloads/pdf-files/aktuelles/photovoltaics-report-in-englischer-sprache.pdf.

21. Renewables 2014 Global Status Report: http://www.ren21.net/Portals/0/documents/Resources/GSR/2014/GSR2014_full%20report_low%20res.pdf.

22. Rech, B., & Wagner, H. Potential of amorphous silicon for solar cells. Applied physics A, 69(2), 155-167. (1999).

23. Green, M. A. ‘Solar cells: Operating principles, technology, and system applications.’ Englewood Cliffs, NJ, Prentice-Hall, Inc., 1982. 288 1-2 (1982).

24. Nelson J. ‘The physics of solar cells’. Vol. 1. London: Imperial college press (2003).

25. NREL PV module reliability workshop 2013: http://www.nrel.gov/docs/fy14osti/60167.pdf.

26. Minnaert B., Veelaert P. ‘A proposal for typical artificial light sources for the characterization of indoor photovoltaic applications’. Energies, 7(3), 1500-1516. (2014).

27. Priambodo, P. S., Sukoco, D., Hartanto, D., Sudibyo, H., & Purnomo, W. ‘Electric energy management and engineering in solar cell system’. INTECH Open Access Publisher (2013).

28. Schroder D. K., Meier D. D. ‘Solar cell contact resistance—a review.’ Electron Devices, IEEE Transactions on 31.5 637-647. (1984).

29. Cubas J., Pindado S., de Manuel C. ‘Explicit expressions for solar panel equivalent circuit parameters based on analytical formulation and the Lambert W-function.’ Energies 7.7 4098-4115. (2014).

30. Bube R. H. ‘Photovoltaic Materials’. Imperial College Press (1998).

31. Wolfe M. ‘Efficiency in Solar Cells’. College Material, Deparment of Physics and Astronomy, Drexel University (2013): http://www.physics.drexel.edu/~bob/TermPapers/Wolfe_termpaper.pdf.

32. Peter, L. M. ‘Towards sustainable photovoltaics: the search for new materials.’ Philosophical Transactions of the Royal Society of London A: Mathematical, Physical and Engineering Sciences 369.1942 1840-1856. (2011).

33. Rahman M. Z., Khan S. I. ‘Advances in surface passivation of c-Si solar cells.’ Materials for Renewable and Sustainable Energy 1.1 1-11. (2012).

34. Hofmann, M., Kambor, S., Schmidt, C., Grambole, D., Rentsch, J., Glunz, S. W., & Preu, R. ‘PECVD-ONO: a new deposited firing stable rear surface

passivation layer system for crystalline silicon solar cells.' Advances in OptoElectronics 2008 1-10. (2008).

35. Vermang, B., Wätjen, J. T., Fjällström, V., Rostvall, F., Edoff, M., Kotipalli, R. 'Employing Si solar cell technology to increase efficiency of ultra-thin Cu (In, Ga) Se2 solar cells.' Progress in Photovoltaics: Research and Applications 22.10 1023-1029. (2014).

36. Boreland M., Bagnall D. 'Current and future photovoltaics'. Report for the Office of Science and Innovation, UK (2006): http://www.foresight.gov.uk/Energy/curre nt_and_future_photovoltaics_.pdf.

37. Richter A., Hermle M., Glunz S. W. 'Reassessment of the limiting efficiency for crystalline silicon solar cells'. IEEE Journal of Photovoltaics, 3(4) 1184-1191. (2013).

38. Kibria M. T., Ahammed A., Sony S. M., Hossain F., Islam S. U. 'A revies: Comparative studies on different generation solar cells technology'. 5th International Conference on Environmental Aspects of Bangladesh (2014).

39. Zhao, J., Wang, A., Altermatt, P. P., Green, M. A., Rakotoniaina, J. P., & Breitenstein, O. 'High efficiency PERT cells on n-type silicon substrates.' Photovoltaic Specialists Conference, 2002. Conference Record of the Twenty-Ninth IEEE. IEEE (2002).

40. Andreani, L., Kowalczewski, P., Mura, C., Patrini, M., Acciarri, M., Binetti. 'Towards CIGS Solar Cells with Reduced Film Thickness: A Study of Optical Properties and of Photonic Structures for Light Trapping.' Proceedings of the 27th

European Photovoltaic Solar Energy Conference and Exhibition, Frankfurt, Germany. (2012).

41. Conibeer, G. 'Third-generation photovoltaics.' Materials today 10.11 42-50. (2007).

42. Barnham K. W. J., Mazzer M. & Clive B. 'Resolving the energy crisis: nuclear or photovoltaics?'. Nature Materials, 5, 161 - 164. (2006).

43. Fang, X., Wu, L., & Hu, L. 'ZnS nanostructures: from synthesis to applications.' Progress in Materials Science 56.2 175-287. (2011).

44. Piezoelectronic properties of ZnO and its potential to power nanotech: http://blogs.hmc.edu/vanheuvelen/the-elements/piezoelectronic-properties-of-zno-and-its-potential-to-power-nanotech-by-faye-jones/.

45. Jafarov M.A., Nasirov E.F., Jahangirova S.A., Jafarli R. 'Nano-ZnS thin films for solar cell'. Nanosystem: Physics, Chemistry, Mathematics, 6 (5), p. 644-649 (2015).

46. Suresh S. 'Synthesis, structural and dielectric properties of zinc sulfide nanoparticles.' International Journal of Physical Sciences 8.21 1121-1127. (2013).

47. Chandran, A., Francis, N., Jose, T., & George, K. C. 'Synthesis structural characterization and optical bandgap determination of ZnS nanoparticles'. Acad Rev, 17(1-2), 17-21. (2010).

48. Eid, A. H., Salim, S. M., Sedik, M. B., Omar, H., Dahy, T., & Abouelkhair, H. M. 'Preparation and Characterization of ZnS thin films.' J. App. Sci. Res 6 777-784. (2010).

49. Haque, F., Rahman, K. S., Islam, M. A., Rashid, M. J., Akhtaruzzaman, M., Alam, M. M. ‘Growth Optimization of ZnS thin films by RF magnetron sputtering as prospective buffer layer in thin film solar cells.’ Chalcogenide Letters 11.4 189-197. (2014).

50. Voutsas, T., Nishiki, H., Atkinson, M., Hartzell, J., & Nakata, Y. ‘Sputtering technology of Si films for low-temperature poly-Si TFTs.’ SHARP Technical Journal 80 36-42. (2001).

51. Gobbi A. L., Nascente P. ‘DC Sputtering.’ Encyclopedia of Tribology. Springer US. 699-706. (2013).

52. M-System FAQ: http://www.m-system.co.jp/newsletter/182/clip_contents.html.

53. Plummer, J. D. ‘Silicon VLSI technology: fundamentals, practice, and modeling’. Pearson Education India (2009).

54. G. Binnig and H. Rohrer, ‘Scanning tunneling microscopy’, Surface Science, 126(1-3) 236-244 (1983).

55. Giessibl F. J. ‘Atomic-resolution of the silicon (111)-(7×7) surface by Atomic Force Microscopy’, Science, 267(5194) 68-71 (1995).

56. Enevoldsen G. H., ‘Scanning Probe Microscopy Studies of a Metal Oxide Surface - a detailed study of the TiO2(110) surface’. University of Aarhus, Faculty of Science, PhD Thesis, (2007).

57. Atomic Force Microscopy for Nanotechnology & Scientific Research | NT-MDT (http://www.ntmdt.com/).

58. Atomic Force Microscopy | AFM Microscope - Park Systems (www.parkafm.com).

59. Sierra R., Javier F., Heckl W. M., Stark R. W. 'Nanomanipulation by atomic force microscopy.' Advanced Engineering Materials 7.4 193-196. (2005).

60. Akamine, S., R. C. Barrett, Quate C. F.. 'Improved atomic force microscope images using microcantilevers with sharp tips.' Applied Physics Letters 57.3 316-318. (1990).

61. Xu X., Raman A. 'Comparative dynamics of magnetically, acoustically, and Brownian motion driven microcantilevers in liquids.' Journal of Applied Physics 102.3 034303. (2007).

62. Mironov V. L. 'Fundamentals of scanning probe microscopy'. The Russian Academy of Sciences (2004).

63. NTMDT principles: http://www.ntmdt.com/spm-principles/.

64. Nanosensors probes: http://www.nanosensors.com/SuperSharpSilicon-Non-Contact-Tapping-mode-High-Resonance-Frequency-Reflex-Coating-afm-tip-SSS-NCHR.

65. AMMRF training for advanced research: http://www.ammrf.org.au/myscope/spm/background/.

66. Oxford instruments: www.oxford-instruments.com.

67. AFM methods: http://www.nanoscience.de/HTML/methods/afm.html.

68. Albrecht, T. R., Grütter, P.; Horne, D.; Rugar, D. 'Frequency modulation detection using high-Q cantilevers for enhanced force microscope sensitivity.' Journal of Applied Physics 69.2 668-673. (1991).

69. Giessibl F. J. ‘Advances in atomic force microscopy’. Experimentalphysik VI, Electronic Correlations and Magnetism, Institute of Physics, Augsburg University, (2003).

70. Garcıa R., Perez R. ‘Dynamic atomic force microscopy methods.’ Surface science reports 47.6 197-301. (2002).

71. Voigtländer B. ‘Scanning Probe Microscopy: Atomic Force Microscopy and Scanning Tunneling Microscopy’. Springer (2015).

72. G. Binnig, C.F. Quate, and C. Gerber, ‘Atomic Force Microscopy’, Phys. Rev. Lett., 56 930-933 (1986).

73. AFM FAQ by Peter Eaton: http://www.fc.up.pt/pessoas/peter.eaton/afm_faq.html#19.

74. Gwyddion user guide: http://gwyddion.net/download/user-guide/ gwyddion-user-guide-en.pdf.

75. Pelliccione M., Lu T. M. ‘Evolution of thin film morphology’. Springer, New York (2007).

76. Condensed Matter Physics Groups, University of Oslo: http://laplace.ucv.cl/Patterns/coopphen_book97/boxes/selfAffineFractals.html.

77. Wargo C. ‘Characterization of Conductors for Printed Electronics’: www. nanopchem. com.

78. http://elearning.vtu.ac.in/11/enotes/Fun-CMOSVLSI/Unit4-UK.pdf.

79. Four point probe operation (UT Dallas): https://www.utdallas.edu/research/cleanroom/manuals/documents/4pointFinal.pdf.

80. Hochberg J., Foster P., Zyvex Corporation. ‘Four Point Probe I-V Electrical Measurements Using the Xyvex Test System Employing a Keithley 4200’. Zyvex Application Note 9702 (2006).

81. EFM Park user manual.

82. Basic of AFM (Utah University): http://www.eng.utah.edu/~lzang/images/Lecture_10_AFM.pdf.

83. Haynes W. M. ‘Handbook of Chemistry & Physics’. CRC 96th edition (2015).

84. Ma, H.L., Zhang, Y., Hu, Q. H., Yan, D., Yu, Z. Z., & Zhai, M. ‘Chemical reduction and removal of Cr (VI) from acidic aqueous solution by ethylenediamine-reduced graphene oxide.’ Journal of Materials Chemistry 22.13 5914-5916. (2012).

85. Melitz, W., Shen, J., Kummel, A. C., & Lee, S. ‘Kelvin probe force microscopy and its application.’ Surface Science Reports 66.1 1-27. (2011).

86. Dingemans G.. ‘Nanolayer surface passivation schemes for silicon solar cells’. PhD Thesis, Department of Applied Physics, Technische Universiteit Eindhoven, (2011).